UNIVERSITÀ DEGLI STUDI DI ROMA
"TOR VERGATA"

FACOLTÀ DI SCIENZE MATEMATICHE, FISICHE E NATURALI
Dipartimento di Fisica

# The ATLAS muon trigger detector in the barrel: performance simulation and cosmic ray tests.

Tesi di dottorato di ricerca in Fisica

presentata da

*Elena Solfaroli Camillocci*



Relatori

Prof. *Rinaldo Santonico*

Prof.ssa *Anna Di Ciaccio*

Coordinatore del dottorato

Prof. *Piergiorgio Picozza*

Ciclo XIX

Anno Accademico 2005-2006

# Contents

**Introduction** **1**

**1 The ATLAS experiment at the LHC collider** **3**
1.1 The Large Hadron Collider . . . . . 3
1.2 The Higgs boson research at LHC . . . . . 4
1.3 The ATLAS experiment . . . . . 8
1.3.1 The Muon Spectrometer . . . . . 16
1.3.2 The trigger and data-acquisition system . . . . . 23

**2 An ATLAS LVL-1 muon trigger detector: the Resistive Plate Chamber** **29**
2.1 The Resistive Plate Chamber . . . . . 29
2.2 Avalanche growth and streamer development in RPC gas gap . . . 31
2.3 The gas mixture . . . . . 33
2.4 The resistive electrodes . . . . . 34
2.5 Pick-up strips and read-out . . . . . 35
2.6 The choice of the avalanche operation mode . . . . . 37
2.7 Time and spatial resolution . . . . . 38

**3 Test results of the ATLAS RPCs** **39**
3.1 The cosmic test stand at the *INFN Roma Tor Vergata Laboratory* . 39
3.1.1 RPC quality tests . . . . . 49
3.1.2 Gas-tightness, electric DC and gap current tests . . . . . 49
3.1.3 Trigger and data acquisition . . . . . 51
3.1.4 Cluster size and detection efficiency study . . . . . 56
3.1.5 Noise detector study . . . . . 60
3.1.6 BOL RPC quality test results . . . . . 65
3.1.7 Study of cross-talk between adjacent RPCs . . . . . 70

3.2 The H8 Test Beam at CERN . . . . . 72
3.2.1 RPC cluster size study at H8 site . . . . . 72
3.3 Conclusions . . . . . 78

**4 The LVL-1 muon trigger logic 81**

**5 Simulation of the LVL-1 muon trigger with cosmic muons 89**
5.1 Detector simulation . . . . . 90
5.1.1 RPC digitization . . . . . 90
5.1.2 LVL-1 trigger logic simulation . . . . . 92
5.2 Cosmic ray simulation in the ATLAS cavern . . . . . 92
5.3 Cosmic muons in the ATLAS cavern . . . . . 95
5.3.1 Cosmic muon rate in the ATLAS cavern . . . . . 97
5.3.2 Results of the cosmic muon digitization . . . . . 99
5.4 The LVL-1 trigger with cosmic muons . . . . . 100
5.5 Trigger study on three ATLAS muon towers . . . . . 105
5.5.1 Dependence on the generation area . . . . . 108
5.5.2 Muon energy cut at generation . . . . . 109
5.5.3 Simulation results and data . . . . . 109
5.6 Study of different LVL-1 trigger schemes for cosmic muons . . . . 114
5.7 Conclusions . . . . . 117

**6 First studies with cosmic muons in the ATLAS cavern 119**
6.1 The first test of a Muon Spectrometer sector in the ATLAS cavern 119
6.1.1 The RPC set-up in the ATLAS cavern . . . . . 124
6.1.2 The data acquisition . . . . . 126
6.2 First results in the ATLAS cavern . . . . . 126
6.2.1 Cluster algorithm . . . . . 128
6.3 Efficiency algorithm . . . . . 134
6.4 An ATLAS muon tower . . . . . 139
6.5 Check of the time alignment . . . . . 141
6.6 Conclusions . . . . . 148

**Conclusions 151**

**Bibliography 155**

# Introduction

The Large Hadron Collider (LHC) is the machine for proton and ion collisions in construction at CERN of Geneva. It will provide the highest ever produced energy in the center of mass, reaching the value of $\sqrt{s} = 14\ TeV$ for proton-proton collisions and giving the possibility to produce particles with mass up to few $TeV$.

The main aim of the LHC experiments is the search for the Higgs boson, which is fundamental to verify the symmetry-breaking mechanism in the electroweak sector of the Standard Model Theory. In addition the LHC experiments will obtain precision measurements of the heavy quarks, and will explore the existence and the predictions of possible supersymmetric models.

ATLAS is one of the LHC experiments. The ATLAS detector is characterized by its stand-alone Muon Spectrometer, based on an air-core toroid system, which generates a large field volume and a strong bending power with a light and open structure. Multiple scattering effects are therefore minimal, and an excellent muon momentum resolution is achieved by high-precision tracking chambers. The muon instrumentation is complemented with a dedicated muon trigger detector, to provide efficient trigger functionality and precision momentum measurements separately. A general overview of the ATLAS experiment is given in chapter 1, with particular attention to the design of the Muon Spectrometer.

In the barrel the ATLAS first level muon trigger relies on the Resistive Plate Chambers (RPC): these are gas ionization detectors which are characterized by a fast response and an excellent time resolution ($\sigma_t \leq 1.5\ ns$). Chapter 2 is dedicated to a description of how a Resistive Plate Chamber works.

Before the ATLAS experiment starts, a good understanding of the detector physics and a complete control of the performance are essential. All subdetectors, therefore, have to be extensively tested before to be installed.

A cosmic muon test stand has been built in the *INFN Roma Tor Vergata Laboratory* for a systematic test of the biggest ATLAS RPCs. It consisted of a preliminary check of the detector status (gas-tightness and test of the electric circuits),

and a characterization of every chamber: in particular the noise rate, the cluster size, the detection efficiency and the gap current have been studied for each detector. The large amount (192) of the tested RPC units provided a significant statistics of data. The procedure of the RPC systematic test and the test results are illustrated in chapter 3. The author collaborated to this test, participating both to the whole test cycles and to the analysis of the results.

Tests of the detector with particle beams are also fundamental. At H8 beam site at CERN, an ATLAS-like detector slice was assembled and tested with particle beams. The presence in the test of the tracking chambers (MDT), combined with the RPCs, allowed to the author an independent study of the RPC performances, exploiting the information extracted from the muon tracks reconstructed by the precision chambers. The results of the H8 test are also discussed in chapter 3.

The assembly of the ATLAS detector in the cavern has already started and will be completed in almost one year. Then a phase of detector calibration and test will precede the beginning of the experiment. During this period the LHC beam will be not yet available and signals from cosmic rays will be acquired, using the RPCs for the trigger. The cosmic muon trigger logic will be the same used for proton-proton collisions, although a dedicated trigger configuration will be necessary. In order to optimize the selection of the cosmic muons, the author studied some possible first level muon trigger configurations, using a Monte Carlo simulation (based on GEANT4). A brief description of the complex logic of the ATLAS first level muon trigger is given in chapter 4, and the study of the trigger for the cosmic muons is described in chapter 5.

Although the ATLAS detector installation in the cavern is still undergoing, some subdetectors are already operative: three muon stations of the lowest sector (the ATLAS sector 13) are ready and working. This allowed to validate the trigger simulation and furthermore to start the muon station debugging. The first performance results of these muon stations are finally presented in chapter 6.

# Chapter 1

# The ATLAS experiment at the LHC collider

## 1.1 The Large Hadron Collider

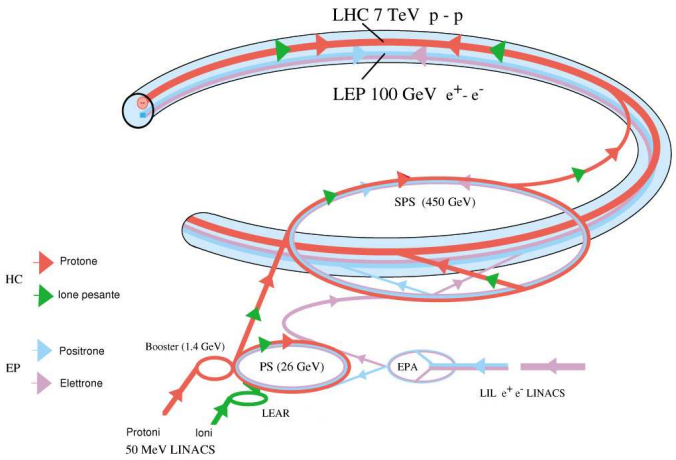


Figure 1.1: The LHC accelerator chain.

The Large Hadron Collider (LHC) is a circular accelerator being built at CERN [1]. It will be hosted in an underground tunnel with a circumference of 27 $Km$. Figure 1.1 shows a schematic view of the layout of the accelerator.

During the main period of the experiment, proton beams will be accelerated and injected in two separate rings, to provide collisions with a centre of mass energy of 14 $TeV$. Proton-proton interactions at such energy offer a wide spectra

of physics investigation, up to particle masses of the order of 1 $TeV$.

The accelerator works with particle bunches of $\sim 10^{11}$ protons, crossing in four points, which will be the four available experimental area. Bunch-crossing will occur every 25 $ns$. At the crossing point the angle between the beams will be $\sim 200\ \mu rad$.

The collider is also designed for heavy ion collisions as $Pb$-$Pb$ collisions, which will be provided with an energy of 1150 $TeV$ in the centre of mass.

The luminosity for $p$-$p$ operation will be of $10^{32}$-$10^{33}\ cm^{-2}s^{-1}$ at the beginning (2008) and will reach $10^{34}\ cm^{-2}s^{-1}$ at $\sqrt{s} = 14\ TeV$ in the following years. These values are two orders of magnitude larger than the previous hadrons colliders, like Tevatron and $S\overline{p}pS$.

The first period at low luminosity is planned to obtain high statistic precision measurements on the heavy quarks bottom and top, and on the $W$ boson mass.

The high luminosity period will be devoted to search for the Higgs boson, the particle that is supposed to be at the origin of the spontaneous symmetry-breaking mechanism in the electroweak sector of the Standard Model Theory.

In addition interactions at such a high energy also give the possibility to explore the predictions of the Supersymmetry Theory.

Three experiments will be installed in the sites of the interaction points: ATLAS (*A Toroidal LHC ApparatuS*) and CMS (*Compact Muon Solenoid*), which are general purpose detectors, and ALICE (*A Large Ion Collider Experiment*) which is dedicated to quark-gluon plasma studies through heavy ions collisions. LHC-b is also a LHC experiment. It has an asymmetric apparatus, explicitly dedicated to the b-physics.

The high rate and luminosity result in high occupancy and events pile-up in the detectors, which should therefore have high radiation hardness, fine granularity, fast response and small dead-time.

## 1.2 The Higgs boson research at LHC

One of the main physics issues, that the centre of mass energy and the high luminosity of the LHC will allow to investigate, is the origin of the spontaneous symmetry-breaking mechanism in the electroweak sector of the Standard Model. According to the theory, the experimental proof of the symmetry-breaking mechanism is expected in the discovery of a new boson, called the Higgs boson.

Figure 1.2 shows the theoretical production cross sections for the Higgs boson

in proton-proton collisions as a function of the Higgs mass ($m_H$) [2]. The total production cross section exceeds 100 $fb$ in the whole estimated mass range.

Feynman diagrams of the principal foreseen production mechanisms for the Higgs boson in proton-proton collisions are shown in figure 1.3.

The gluon fusion process has the highest cross section over the whole mass range, although for $m_H \sim 1\ TeV$ the $Z$ or $W$ fusion process becomes comparable with the gluon fusion.

The coupling of the Higgs boson to a particle depends on the mass of the particle. As a consequence, the heavier are particles Higgs decays in, the higher results the corresponding branching ratios. Figure 1.4 shows the branching ratios of the Higgs boson as a function of its mass.

The Higgs decay channels, their backgrounds and their signatures at LHC [5] can be summarized as follow, as a function of the Higgs mass:

- $m_H < 130\ GeV$. In this mass region $H \rightarrow b\bar{b}$ is the most favorite channel, the $b\bar{b}$ being the heaviest fermion pair accessible to the Higgs. This decay channel is affected by the background of $b\bar{b}$ coming from other processes; but the Higgs decay could be recognizable with clean experimental signature through the identification of the leptons from the decays of the $t$ quark or of the gauge bosons, produced in association with the Higgs. Therefore, the Higgs productions associated with a $t\bar{t}$ pair or with a gauge boson become interesting decay channels for the LHC physics studies, even though they have small cross sections (see figure 1.2).
  The channel $H \rightarrow \gamma\gamma$ is rarer, but it has a clear experimental signature: these events are characterized by two isolated photons with high transverse momentum ($p_T$). Its detection requires a good identification of photons and a high energy resolution. The background for this channel is mainly due to $q\bar{q} \rightarrow \gamma\gamma$ and $gg \rightarrow \gamma\gamma$ processes.

- $130\ GeV < m_H < 2m_Z$. One of the most promising channels in this region is $H \rightarrow ZZ^* \rightarrow 4l$. The background for this kind of processes comes from $t\bar{t} \rightarrow Wb + W\bar{b} \rightarrow l\nu + l\nu\bar{c} + l\nu + l\nu c$ and $Zb\bar{b} \rightarrow 4l$, and can be reduced requiring at least a pair $l^+l^-$ with a mass compatible with the $Z$ mass and rejecting events with secondary vertices.
  At $m_H = 170\ GeV$ the dominant decay channel becomes $H \rightarrow WW^*$. In this case the signal $H \rightarrow WW^* \rightarrow l\nu l\nu$ will be studied, thus requiring a good resolution in the transverse missing energy.

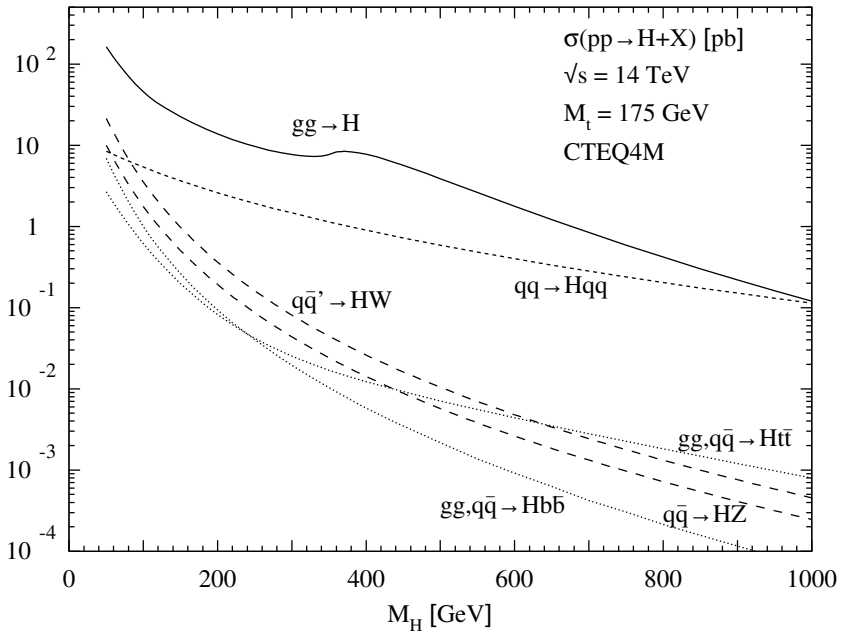


Figure 1.2: Production cross sections for the Higgs boson at LHC as a function of the boson mass.

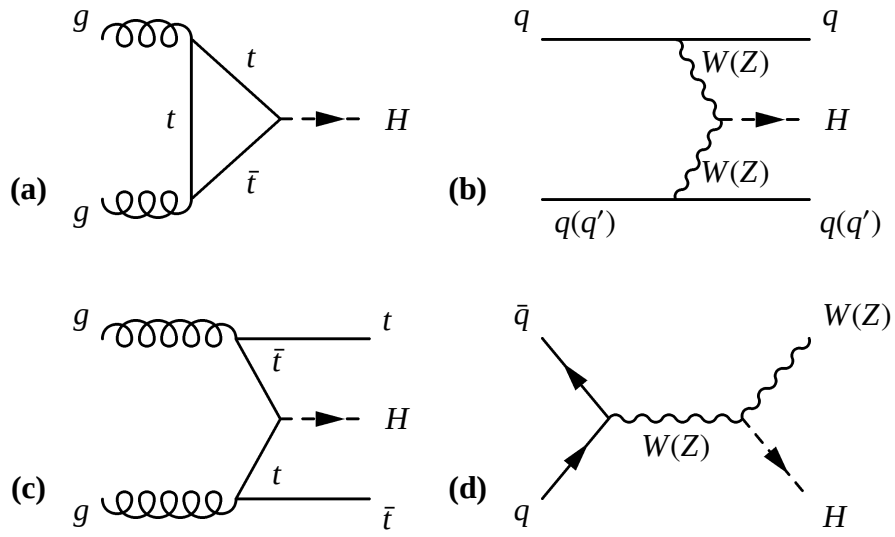


Figure 1.3: Feynman diagrams of the main production processes of the Higgs boson: gluon fusion (a), $Z$ or $W$ fusion (b), production associated with a $t\bar{t}$ pair (c) or with a $Z$ or $W$ boson (d).

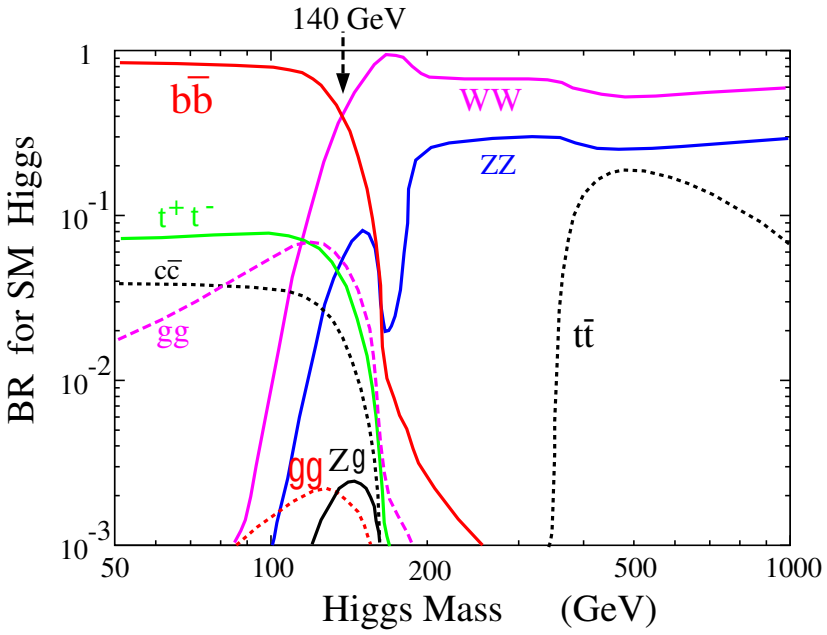


Figure 1.4: Higgs branching ratios as a function of the Higgs mass.

- $m_H \geq 2m_Z$. At these masses, the channel $H \rightarrow 4l$ becomes accessible. Thanks to the high $p_T$ of the four leptons, this channel decay has an extremely clean signature and is a very important candidate for the Higgs research.
  At $m_H > 600\ GeV$, also the channels $H \rightarrow ZZ \rightarrow llvv$ and $H \rightarrow WW \rightarrow lv\,jet\,jet$ can be studied. Detecting Higgs decays in jets is not easy due to the irreducible background of QCD events, but the presence of leptons in association with jets can make recognizable the signature.

The expected significances of the signals discussed above are shown in figure 1.5 for the ATLAS experiment. The discovery potential for each channel depends on the Higgs mass, but for the whole mass range there are one or more channel with a recognizable signature.

If the Higgs boson will be observed at LHC, the ATLAS experiment will be able to measure the Higgs mass with a precision of $\sim 0.1\%$ up to $m_H$ of 600 $GeV$.

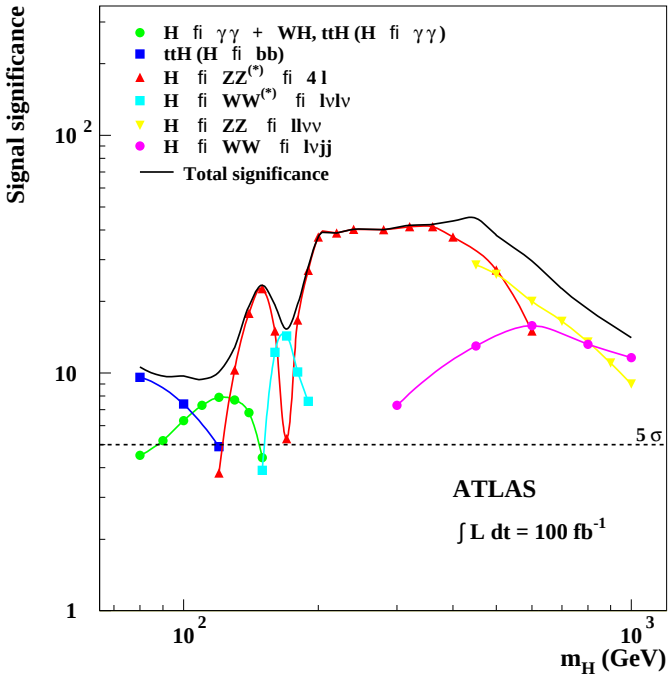


Figure 1.5: Expected discovery potential for the Higgs boson of the ATLAS experiment for an integrated luminosity of 100 $fb^{-1}$, as a function of the Higgs mass.

## 1.3 The ATLAS experiment

Among the LHC experiments, ATLAS and CMS are especially dedicated to the Higgs research. The design of the ATLAS [3, 4] detector [5] as therefore optimized to allow the identification of the Higgs boson decays, but also the requests for study of physics of $t$ and $b$ quarks influenced the project.

In order to achieve the necessary sensitivity to the physics processes to be studied at the LHC, the ATLAS detector provides:

- Electron and photon identification and measurements, using a very good electromagnetic calorimetry.
- Accurate jet and missing transverse momentum measurements, using, in addition to electromagnetic calorimeters, the full-coverage hadronic calorimetry.
- Efficient tracking also at high luminosity, with particular focus on high-$p_T$

lepton momentum measurements.

- Large acceptance in pseudorapidity[1], and almost full coverage in the $\phi$ view.

A scheme of the ATLAS detector is in figure 1.6. Three parts are evidenced: one barrel in the middle and two end-caps closing the structure. The whole detector is long 46 $m$ and has a diameter of 22 $m$. Its weight is about 7000 $Tons$.

### The Magnet System

The magnet system, which implies the huge dimensions of the detector, consists of two independent subsystems in the barrel: a superconducting solenoid around the inner detector cavity, and a large superconducting air-code toroid outside the calorimeters. In the end-cap regions, the magnetic field is provided by two toroid systems inserted in the barrel toroid and lined up with the central solenoid. This configuration allows to avoid particular constraints on calorimetry and inner detectors, leaving full choice for technological solutions, and to realize a high resolution, large acceptance and robust stand alone muon spectrometer.

The central solenoid provides the inner trackers with a field of 2 $T$ (the peak at the solenoid surface is 2.6 $T$). Being the solenoid inner regards to the calorimetric system, its design was carefully tuned in order to minimize the material and not to produce any degradation of the calorimeter performance. As a consequence of this constraints, the solenoid and the electromagnetic calorimeter share the same vacuum vessel. The solenoid requires a 8 $kA$ power supply.

The magnetic field generated by the toroids has a peak value of 3.9 $T$ in the barrel region and 4.1 $T$ in the end-caps. The 8 coils of the barrel toroid, as well as the 8 + 8 coils of the end-caps toroids are electrically connected in series and fed by a 21 $kA$ power supply. Figure 1.7 shows a scheme of the ATLAS toroids.

The magnets are cooled by a flow of helium at 4.5 $K$.

### The Inner Detector

The Inner Detector is entirely contained inside the Central Solenoid, which provides a magnetic field of 2 $T$, oriented along the beam direction.

[1]The pseudorapidity is defined as $\eta = -\ln\left(\tan\frac{\theta}{2}\right)$ and is the limit of the rapidity of a particle in the final-state $y = \frac{1}{2}\ln\left(\frac{E+P_{\parallel}}{E-P_{\parallel}}\right)$ for E≈P (m≪E). It is usually used to substitute the $\theta$ angle in polarity coordinates system. In the ATLAS reference: $\theta$ is the angle with respect to the beam axis, and the angle measured around the beam axis is called $\phi$.

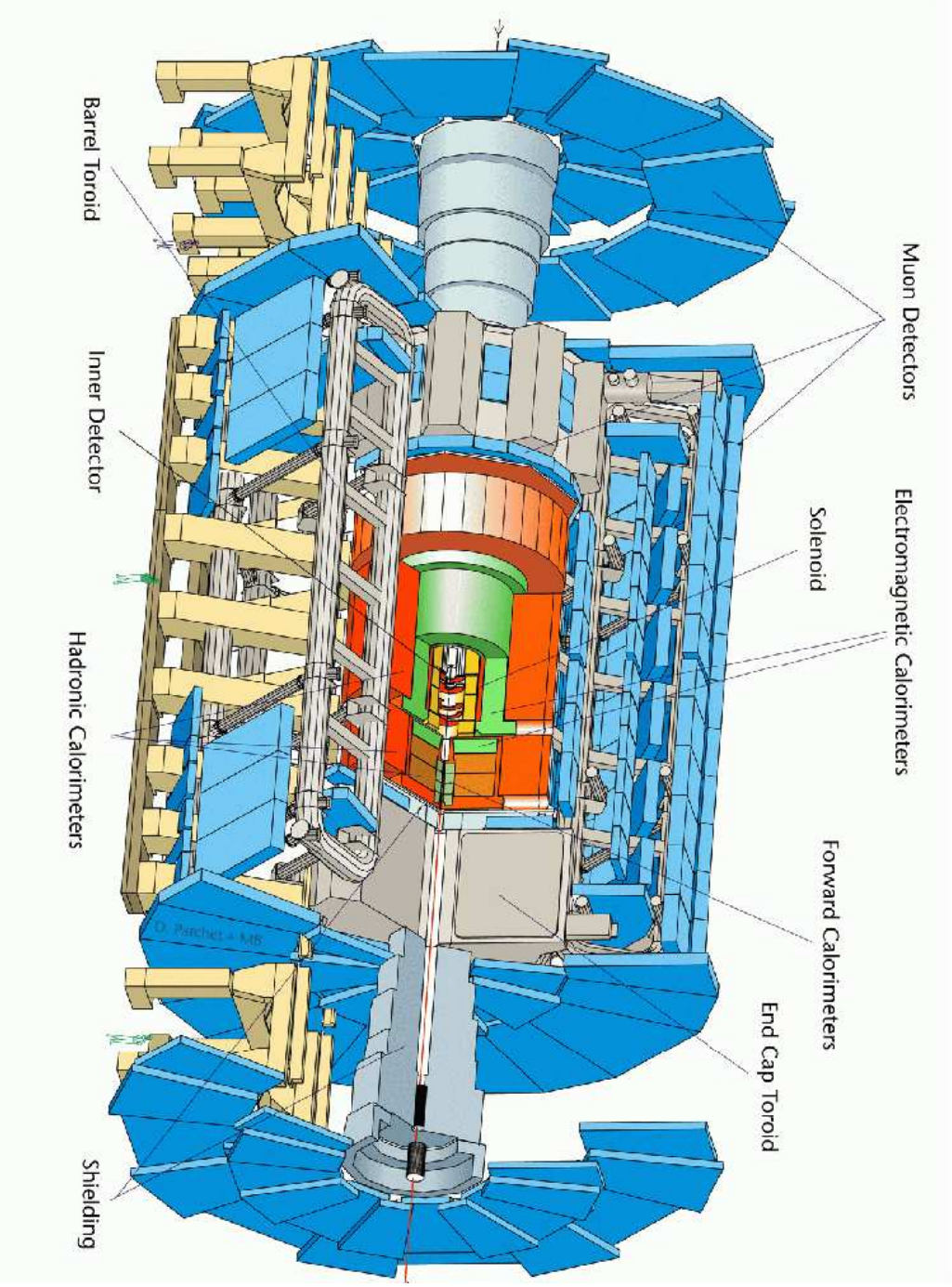


Figure 1.6: The ATLAS detector. The layout of the subdetectors is shown.

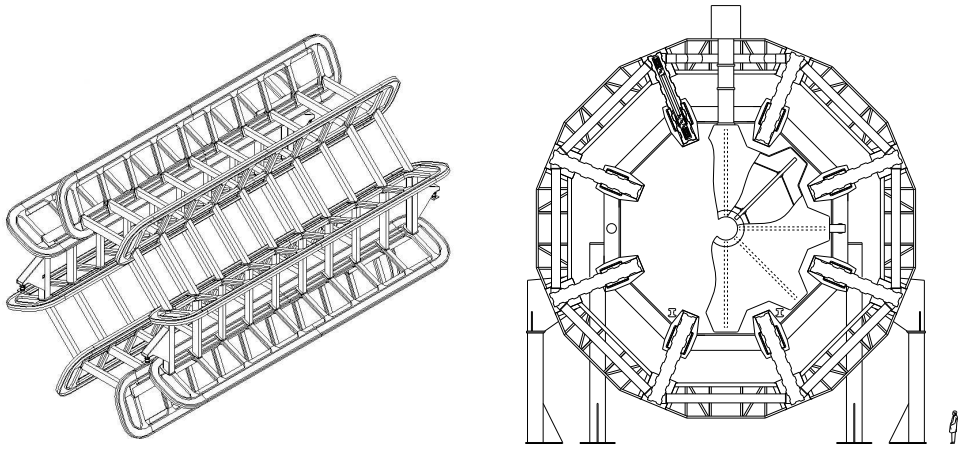

Figure 1.7: Design of the ATLAS magnetic toroids: the barrel toroid on the left and an end-cap toroid on the right.

The high track density expected for the LHC events requests a careful design of the inner tracker. In order to achieve the maximum granularity with the minimum material, two different technologies have been chosen: semiconductor trackers in the region around the vertex and a straw tube tracker at the outer radii. Figure 1.8 shows a schematic view of the Inner Detector.

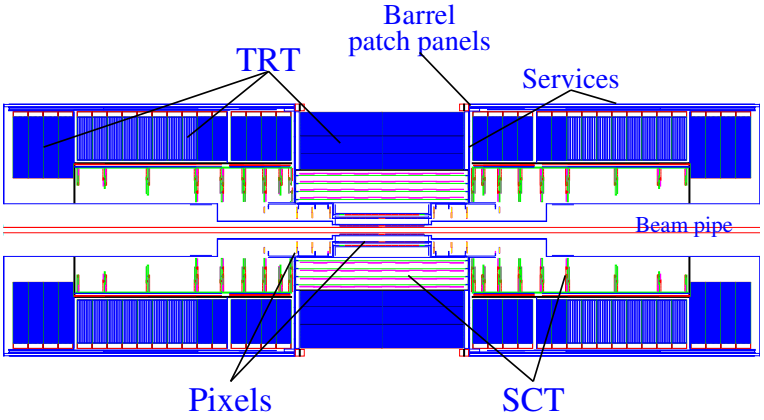


Figure 1.8: The ATLAS Inner Detector.

Pixel detectors and silicon microstrip detectors (SCT) constitute the semiconductor tracker. The total number of precision layers is limited by the amount of material they introduce and by their cost. In the resulting setup, a track typically crosses three pixel layers and eight SCT layers (four space points).

The three pixel layers in the barrel are arranged on concentric cylinders around the beam axis and have a resolution of 12 $\mu m$ in the radial direction ($R\phi$) and of 66 $\mu m$ for the $z$ coordinate[2]. In the end-caps the pixel detectors are mounted on disks perpendicular to the $z$ axis. They provide measurements in $R\phi$ and $R$ with resolutions of 12 $\mu m$ and 77 $\mu m$ respectively. The innermost pixel layer in the barrel is placed at about 4 $cm$ from the beam axis, in order to improve the secondary vertex measurement capabilities.

The SCT detector uses small angle (40 $mrad$) stereo strips to measure positions in both coordinates ($R\phi, Z$ for the barrel and $R\phi, R$ for the end-caps). For each detector layer one set of strips measures the $\phi$ angle. The resolution is 16 $\mu m$ on the radius distance, while it is 580 $\mu m$ for the $z$ coordinates in the barrel region and for the $R$ direction in the end-caps.

The straw tubes are positioned parallel to the beam in the barrel, while in the end-caps they are placed along the radial direction. For the straw tubes a resolution of 170 $\mu m$ has been achieved in test-beams. Since each track crosses about 36 tubes, the lower precision per point compared to the silicon is compensated by the large number of measurements and the higher average radius. Combined measurement accuracy of better than 50 $\mu m$ at the LHC design luminosity, averaged over all straws, is guaranteed. The relative precision of the different measurements is well matched, so that no single measurement dominates the momentum resolution. This implies that the overall performance is robust.

In addition, by employing xenon-based gas mixture the straw tube tracker can also detect the transition-radiation photons emitted in a radiator between the straws, thus improving the ATLAS particle identification capabilities.

### The Calorimeters

A view of the ATLAS calorimeters is presented in figure 1.9. The calorimetry consists of an electromagnetic calorimeter covering the pseudorapidity region $|\eta| < 3.2$, a hadronic barrel calorimeter covering $|\eta| < 1.7$, hadronic end-cap calorimeters in the $1.5 < |\eta| < 3.2$ range, and forward calorimeters covering $3.1 < |\eta| < 4.9$.

**The Electromagnetic Calorimeter** is divided in three parts: one in the barrel ($|\eta| < 1.7$) and two in the end-caps ($1.375 < |\eta| < 3.2$). The barrel calorimeter is

[2]In the ATLAS reference the $z$ axis follows the beam direction. The $x$-$y$ plane is perpendicular to the beam axis. The $x$ positive direction points to the center of the LHC, and the $y$ axis is pointing upwards.

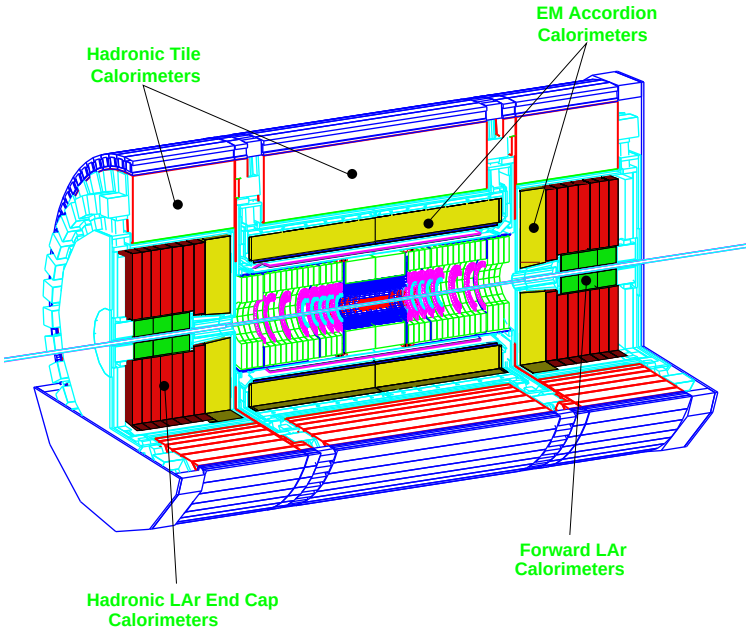


Figure 1.9: The ATLAS calorimeters.

divided in two half barrels, with a small (6 *mm*) gap between them at $z = 0$. The end-cap calorimeters are both made up of two coaxial wheels.

The Electromagnetic Calorimeter is a Liquid Argon detector with lead absorber plates and Kapton electrodes. In order to provide a full coverage in $\phi$ without azimuthal cracks, an accordion geometry was chosen for the internal layout of the calorimeter. The lead absorber layers have variable thickness as a function of $\eta$ and has been optimized to obtain the best energy resolution. The Liquid Argon gap on the contrary has a constant thickness of 2.1 *mm* in the barrel. The total thickness is greater than 24 radiation lengths ($X_0$) in the barrel and $> 26\ X_0$ in the end-caps.

Over the region devoted to precision physics ($|\eta| < 2.5$), the Electromagnetic Calorimeter is longitudinally divided in three sections. The first region is meant to work as a preshower detector, providing particle identification capabilities and precise measurement in $\eta$. It has a constant thickness of $\sim 6\ X_0$ as a function of $\eta$.

The middle section is divided into towers of size $\Delta\eta \times \Delta\phi \simeq 0.025 \times 0.025$

($\sim 4{\times}4\ cm^2$ at $\eta = 0$) with square section. At the end of this section the calorimeter has a total thickness of $\sim 24\ X_0$.

The third section has a lower granularity in $\eta$ ($\sim 0.05$) and a thickness varying between $2\ X_0$ and $12\ X_0$.

The calorimeter cells point towards the interaction region over the complete $\eta$ range. The total number of channels is about $10^5$. A schematic layout of a calorimeter cell is shown in figure 1.10.

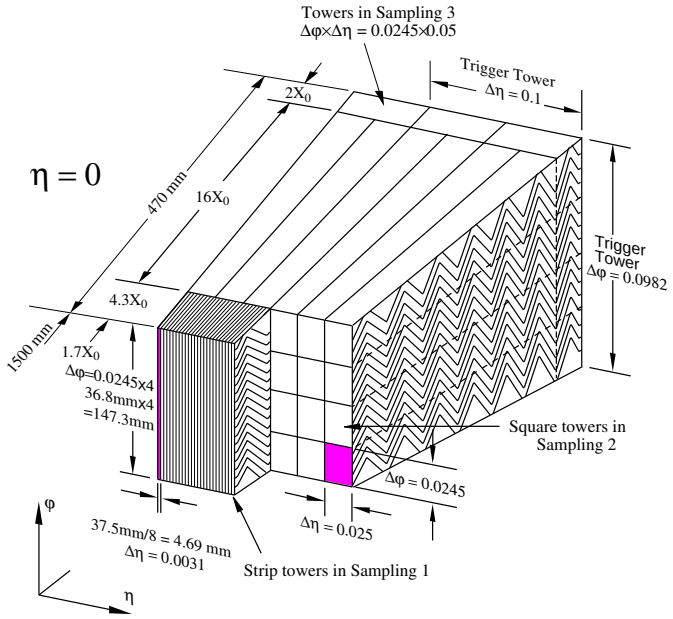


Figure 1.10: Schematic layout of an ATLAS accordion calorimeter module.

**The Hadronic Calorimeter** cover the region $|\eta| < 4.9$ using different techniques, taking into account the different requirements and radiation environment over this large $\eta$ range.

The range $|\eta| < 1.7$, corresponding to the barrel calorimeter, is equipped with a calorimeter based on the iron/scintillating-tile technology.

Over the range $1.5 < |\eta| < 4.9$, liquid argon calorimeters were chosen. In this region the hadronic calorimetry is segmented into an Hadronic End-Cap Calorimeter (HEC), extending up to $|\eta| < 3.2$ and a High Density Forward Calorimeter (FCAL) covering the region with highest $|\eta|$. Both the HEC and the FCAL are integrated in the same cryostat housing the electromagnetic end-caps calorimetry. The overall layout of the ATLAS hadronic calorimeters is shown in figure 1.9.

The thickness of the calorimeter has been carefully tuned in order to provide good containment of hadronic showers and reduce to the minimum the punch-through into the muon system. At $\eta = 0$ the total thickness is 11 interaction lengths ($\lambda$), including the contribution from the outer support ($\sim 1.5\ \lambda$). This has been shown by measurements and simulation to be sufficient to reduce the punch-through to just prompt or decay muons, therefore 10 $\lambda$ of active calorimeter provide good resolution for high energy jets. This characteristics, together with the large $\eta$ coverage, will guarantee an accurate $E_T^{miss}$ measurement, which is an important parameter in the signatures of many physics processes.

In particular the technologies employed in the Hadronic Calorimeter are:

*The Tile Calorimeter*, hosted in the barrel region, is a sampling calorimeter using iron as the absorber and scintillating tiles as the active material. Radially, it extends from an inner radius of 2.28 *m* to an outer radius of 4.25 *m*. The tiles are placed radially and staggered in depth, with a periodic structure along *z*. Tile thickness is 3 *mm* and the total thickness of the iron plates in one period is 14 *mm*. Both sides of the scintillating tiles are readout with two separate photomultipliers.

The barrel calorimeter is segmented along *z* into one barrel part and two extended barrels. It is longitudinally segmented in three layers of 1.4, 4.0 and 1.8 $\lambda$ at $\eta = 0$. Azimuthally, the barrel and the extended barrels are divided into 64 modules.

The readout cells, consisting of fibers grouped into a photomultiplier, are arranged along $\eta$ with a pseudo-projective geometry, i.e. pointing towards the interaction region. The resulting granularity is $\Delta\eta \times \Delta\phi = 0.1 \times 0.1$, reduced to $0.2 \times 0.1$ in the last layer.

Each *Liquid-Argon Hadronic End-Cap Calorimeters* consists of two independent wheels, with an outer radius of 2.03 *m*. The upstream wheel is built with 25 *mm* copper plates, separated by a gap of 8.5 *mm*. The gap is equipped with three parallel electrodes splitting the gap into four drift regions of about 1.8 *mm*. The central electrode is used for the readout. The wheels farther from the interaction point have the same structure, but with 50 *mm* plates.

*The Liquid-Argon Forward Calorimeter* is located in a region where a high level of radiation is expected. It is integrated into the end-cap cryostat and its front face is at about 4.7 *m* from the interaction point. In order to reduce the neutron albedo in the Inner Detector cavity, the front face of the Forward Calorimeter

is recessed of 1.2 $m$ with respect to the Electromagnetic Calorimeter front face. This limitation in space, together with the requirement of 9.5 active interaction lengths, calls for a high density design.

The Forward Calorimeter consists of three sections: the first one made of copper, the other two of tungsten. In each section, the detector has a structure consisting of a metal matrix with regularly spaced longitudinal channels filled with concentric rods and tubes. The rods are at positive high voltage, while the tubes and the matrix are grounded. The Liquid-Argon is the sensitive medium.

### 1.3.1 The Muon Spectrometer

One of the most promising signatures of Higgs physics at the LHC is expected from the decay channel $H \rightarrow ZZ^* \rightarrow 4l$, recognizable by the presence of high momentum final state muons. To exploit this potential, it is important that ATLAS detector provides a high resolution Muon Spectrometer with stand-alone trigger, allowing the high precision measurement of muon transverse momentum over a wide range of pseudorapidity and azimuthal angle.

In particular the most relevant spectrometer parameters that have been optimized are:

- Resolution: Momentum and mass resolutions at the level of few per cent are required for reliable charge identification and for reconstruction of two- and four-muon final states on top of the background levels. A transverse momentum resolution, that is constant over the full rapidity range, is desirable.

- Second coordinate measurement: In order to obtain a safe track reconstruction, muon tracks need to be detected along the non-bending projections with a resolution lower than 10 $mm$.

- Rapidity coverage: The pseudorapidity coverage up to $|\eta| \sim 3$, together with the good hermetic performance, is essential for all physics processes, in particular for rare high-mass processes.

- Trigger selectivity: Trigger thresholds of about 10-20 $GeV$ are adequate to select events with high mass states. But also lower thresholds ($\sim 5$ $GeV$) are necessary to study beauty physics and CP violation.

- Bunch-crossing identification: The LHC bunch-crossing interval of 25 $ns$ sets the scale for the required time resolution of the first-level trigger system.

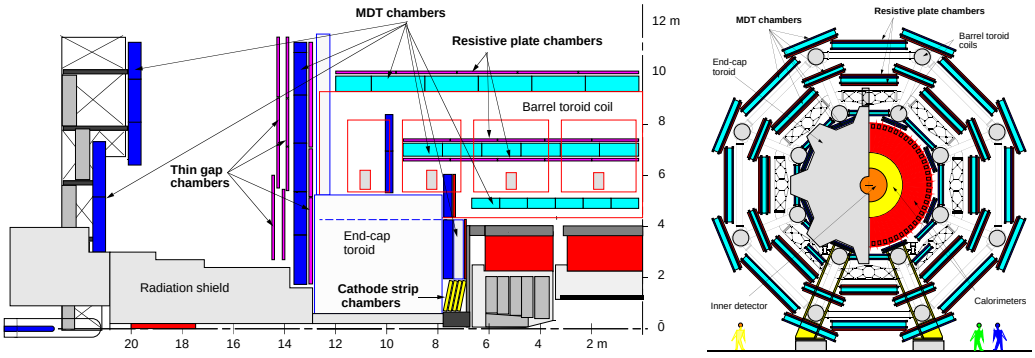


Figure 1.11: Side view of one sector (on the left) and transverse view (on the right) of the Muon Spectrometer.

The conceptual layout of the ATLAS Muon Spectrometer [7] is shown in figure 1.11. The detector design is based on the deflection of muon tracks in a system of three large superconducting air-core toroid magnets (fig. 1.7). In the region with $|\eta| < 1.0$ the magnetic field is generated by the large barrel toroid surrounding the hadronic calorimeter. For $1.4 < \eta < 2.7$ muons are bent by the field produced by two end-cap toroids inserted at both end of the barrel toroid. In the transition region ($1.0 < \eta < 1.4$) muon bending is provided by a combination of the barrel and end-cap fields.

In the barrel, particles are measured at the boundaries of the magnetic field and inside the field volume. The muon subdetectors are arranged such as three radial stations, so particles from the interaction point cross at least three precision chambers, that allow to determine the momentum from the measurement of the trajectory sagitta.

For $|\eta| < 1.4$ the magnet cryostats do not allow positioning of chambers inside the field volume, so the chosen solution is to arrange the chambers in such a way as to determine the momentum with a point-angle measurement.

Figure 1.12 shows the overall layout of the muon chambers in the ATLAS experiment. The positioning of the chambers is optimized to obtain the most hermetic configuration [7].

The chambers in the barrel are arranged on three cylinders concentric with the beam axis, at radii of about 5, 7.5 and 10 $m$. Three chambers form projective towers, pointing to the interaction point. The relative position of the chambers in a tower is constantly monitored by alignment optical rays.

The end-cap chambers are arranged in four disks, concentric with the beam

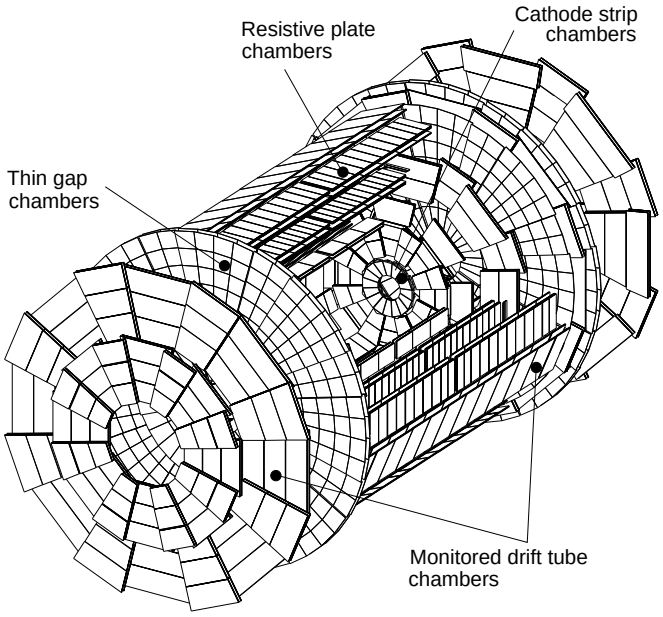


Figure 1.12: Three-dimensional view of the muon spectrometer chambers layout.

axis, at 7, 10, 14 and 21-23 $m$ from the interaction point. The combination of barrel and end-cap chambers provides almost complete coverage in $\eta$ ($|\eta| \leq 2.7$), except for the openings at $\eta = 0$ allowing the passage of cables and services.

The spectrometer is azimuthally segmented in 16 sectors, following the eight-fold symmetry of the magnet structure. The sectors are of two different dimensions: Large Sectors are the ones between two successive coils, and Small Sectors are the one within a coil.

The high level particle flux has impact on the choice and design of the spectrometer instrumentation, with particular attention to the affecting parameters such as rate capability, granularity, ageing properties and radiation hardness. Therefore trigger and reconstruction algorithms must be carefully optimized to cope with the difficult background conditions.

The background in the spectrometer is principally due to primary collision products penetrating in the spectrometer through the calorimeters. Signals from this background are correlated in time with the $p$-$p$ interaction; their sources are semileptonic decays of light and heavy flavors, gauge bosons decays, shower

muons and hadronic punch-through. Figure 1.13 shows the inclusive muon cross sections as a function of transverse momentum.

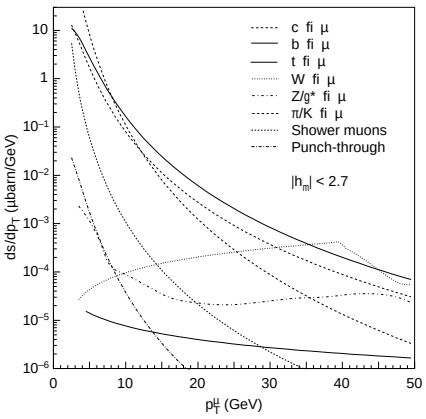


Figure 1.13: Transverse momentum dependence of inclusive muon cross sections.

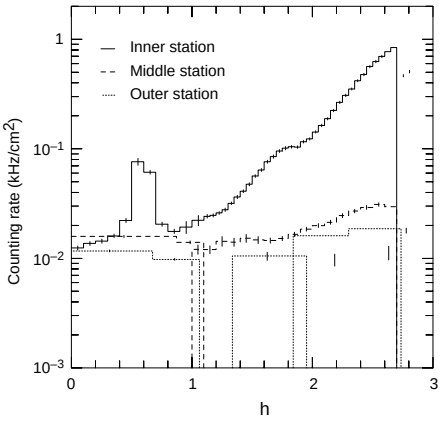


Figure 1.14: Expected counting rates in the three stations of precision chambers for charged and neutral particles, as a function of $\eta$. The rates are calculated at the nominal LHC luminosity.

In addition also neutrons and photons produced by secondary interactions in the inner subdetectors can reach the Muon Spectrometer. These particles enter the spectrometer from all directions and are no more correlated in time with the bunch-crossing.

The expected counting rate in the three stations of precision chambers for charged and neutral particles is shown in figure 1.14.

Taking into account the requests of physics studies and the difficulties related to the low energy background, Monitored Drift Chambers (MDTs) has been chosen for precision measurements of muon tracks. They are arranged in all the spectrometer, except in the innermost ring of the inner end-cap station, where the precision detector consists of Cathode Strip Chambers (CSCs), due to the higher expected particle flux in the end-cap regions. These technologies are able to measure a track point with an accuracy better than 50 $\mu m$, that is essential to allow momentum measurements with a precision $\Delta p_T/p_T < 10^{-4} \times p/GeV$ for $p_T > 300\ GeV$ (at lower energies the resolution is limited to a few percent by multiple scattering and by energy loss fluctuation in the calorimeters) by means of three-point measurements and sagitta reconstruction.

The trigger is provided by three stations of Resistive Plate Chambers (RPCs) in the barrel region, and three stations of Thin Gap Chambers (TGCs) in the end-caps.

Table 1.1 summarizes the characteristic numbers of the muon instrumentation.

| | Precision Chambers | | Trigger Chambers | |
|---|---|---|---|---|
| | CSC | MDT | RPC | TGC |
| Number of chambers | 32 | 1194 | 596 | 192 |
| Number of readout channels | 67000 | 370000 | 355000 | 440000 |
| Area covered ($m^2$) | 27 | 5500 | 3650 | 2900 |

Table 1.1: Overview of the muon chamber instrumentation.

**The Monitored Drift Chambers** are made of aluminium tubes of 30 *mm* diameter and 400 $\mu m$ wall thickness, with a central 50 $\mu m$ diameter W-Re wire [8]. The tube lengths vary from 70 *cm* for the inner chambers to 630 *cm* for the outer chambers.

The tubes are operated with a $Ar$-$CO_2$ (97%-3%) mixture at 3 *bar* absolute pressure and the anode wire is supplied by 3080 *V* to work in proportional mode. At the working point the maximum drift time is about 700 *ns*.

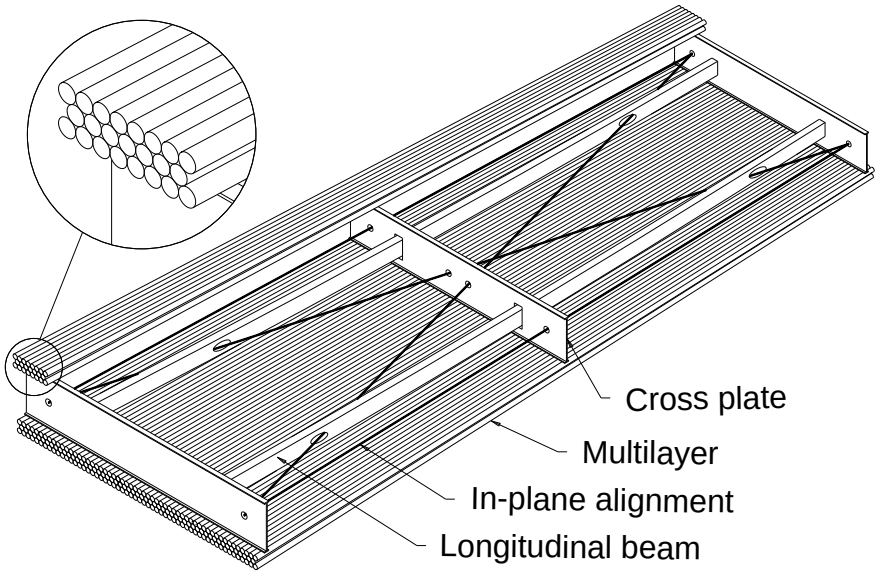


Figure 1.15: Schematic diagram of an MDT.

The tubes are arranged in $2 \times 4$ monolayers for the inner stations and $2 \times 3$

monolayers for the medium and outer stations. A schematic view of the structure of an ATLAS MDT is shown in figure 1.15. This design allows to improve the single-wire precision and provides the necessary redundancy for track reconstruction. The two multilayers of each station are placed on either side of a special support structure (spacer), providing accurate positioning of the tubes with respect to each other. The support structure also slightly bends the tubes of the chambers which are not in a vertical position, compensating the gravitational sag of the wires. Most of the components of the alignment system are mounted on the spacers: once the chambers are installed in the ATLAS detector, all their deformations will be monitored (hence their name) by an in-plane optical system.

Each tube is read out at one end by a low impedance current-sensitive preamplifier, whose threshold is set to a value five times above the noise level. The signal is then processed by a differential amplifier, a shaping amplifier and a discriminator. The leading edge time of the signal can vary as a consequence of charge fluctuations (*time slewing*), this is why a simple ADC also receives the output of the shaper, allowing for the use of the charge-integrated signal to correct the *time slewing*. Finally, the signals are sent to TDCs which measure the drift time with a 300 $ps$ RMS resolution.

A set of data for auto-calibration allow to determine the $r$-$t$ relation (drift-time drift-distance relation) for a tube, in order to correct small deviation from the radial drift due to magnetic effect and change of environment parameters (temperature, humidity and so on).

**The Cathode Strip Chambers** [7] substitute the MDTs in the first end-cap muon measuring station, where high counting rates ($> 200\ Hz/cm^2$) are expected.

CSCs are multiwire proportional chambers with cathode strip readout and with a symmetric cell in which the anode-cathode spacing is equal to the anode wire pitch (2.54 $mm$). Figure 1.16 shows a schematic view of a CSC: the cathode readout pitch ($W$) is 5.08 $mm$. The cathode strip readout, using charge interpolation, provides a spatial resolution of 80 $\mu m$.

CSCs are located at approximately 7 $m$ from the interaction point, occupying the radial space between 881 and 2081 $mm$.

In a typical multiwire proportional chamber signals on the anode wires are read out, thus limiting the spatial resolution to $S/\sqrt{12}$. In a CSCs a higher precision can be achieved measuring the charge induced on the segmented cathode by the avalanche formed on the anode wire.

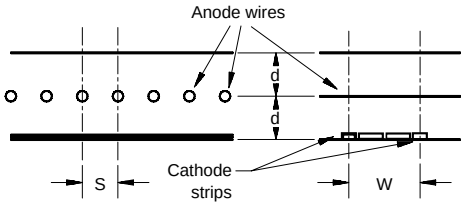


Figure 1.16: Schematic diagram of a Cathode Strip Chamber.

**The Resistive Plate Chambers** are gaseous detectors providing a typical space-time resolution of $1\ cm \times 1\ ns$. This performance made RPCs good candidates for muon trigger chambers in the ATLAS barrel. RPC structure and performance are extensively presented in the chapter 2.

**The Thin Gap Chambers** have a structure very similar to the one of multiwire proportional chambers, with the difference that the anode wire pitch (1.8 *mm*) is larger than the anode-cathode distance (1.4 *mm*). Figure 1.17 shows the inner structure of a TGC.

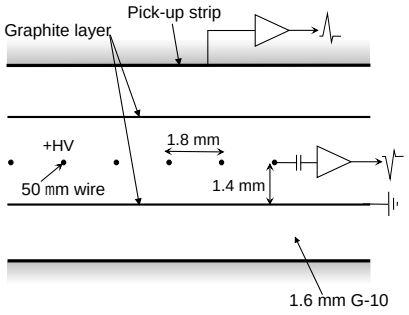


Figure 1.17: Structure of a TGC.

The radial (or bending) direction is measured by reading which wire-group is hit; the azimuthal coordinate is obtained from the radial strips.

When operated with a highly quenching gas mixture ($CO_2$ : $n$-$C_5H_{12}$ = 55% : 45%), this chambers work in a saturated mode, thus allowing for small sensitivity to mechanical deformations, which is very important for such a large detector as ATLAS [9].

The saturated mode also has two more advantages:

- the signal produced by a minimum ionizing particle has only a small dependence on the incident angle up to angles of 40 degrees;

- the tails of the pulse-height distribution contain only a small fraction of the pulse-heights (less than 2%). In particular the response to slow neutrons is similar to that of minimum ionizing particles. No streamers are observed in any operating conditions.

As trigger chambers, TGCs are required to have good time resolution to provide bunch-crossing identification, that means assigning more than 99% of the triggered muons to the correct bunch-crossing.

TGCs also provide azimuthal coordinate measurement in the end-caps. The middle tracking station of MDTs is equipped together with seven layers of TGCs, which provide two functionalities: muon trigger and azimuthal coordinate measurement. The inner tracking layer of precision chambers is equipped with two layers of TGCs, providing only the second coordinate measurement; while the second coordinate in the outer precision station is obtained by extrapolation from the middle station.

Since the TGCs are located outside the end-cap magnetic field and they can use only a small lever arm ($\sim 1\ m$), they need a fine granularity also in the bending direction. To obtain the required momentum resolution it has been chosen to vary the number of wires in a wire-group as a function of $\eta$, from 4 to 20 wires (i.e. from 7.2 to 36 $mm$). The alignment of the wire groups in two consecutive layers is staggered by half the group width.

The chambers are mounted in two concentric rings on each end-cap: an external one in the range $1.05 < \eta < 1.6$ and another one in the area $1.6 < \eta < 2.4$. In order to cope with the higher background rate expected in the innermost rings, three different trigger thresholds can be set for the three rapidity regions.

### 1.3.2 The trigger and data-acquisition system

The ATLAS trigger and data-acquisition (DAQ) system is described in figure 1.18. It is based on three levels of on-line event selection, called LVL-1, LVL-2 and EF (Event Filter). Each trigger level refines the decisions made at the previous level and, where necessary, applies additional selection criteria. Starting from an initial bunch-crossing rate of 40 $MHz$, the rate of selected events must be reduced to $\sim 100\ Hz$ for permanent storage.

The LVL-1 [10] trigger level acts on reduced granularity information from the calorimeters and the muon spectrometer; its decision is based on selection criteria of inclusive nature. Example menus are shown on tables 1.2 and 1.3 with the corresponding trigger rate expected at low and high luminosity.

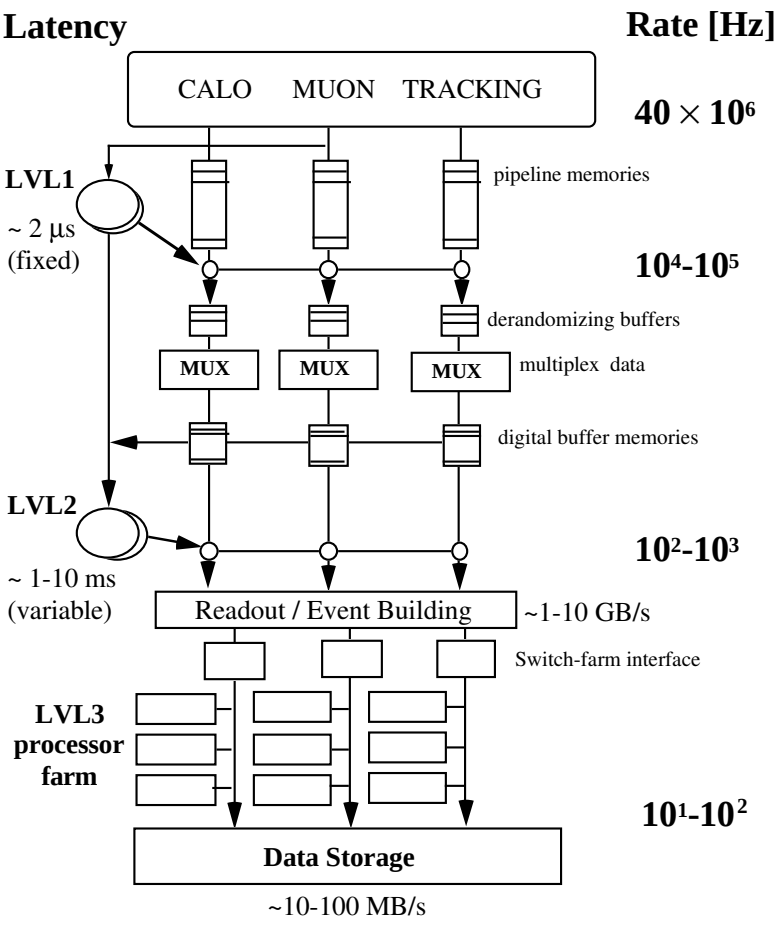


Figure 1.18: Block diagram of the ATLAS Trigger/DAQ system.

LVL-1, whose block diagram is shown in figure 1.19 is divided into four parts: the calorimeter trigger; the muon trigger; the central trigger processor, which is in charge of taking the final decision; and the TTC (Timing, Trigger and Control distribution system), which is responsible for the distribution of the trigger output to the front-end electronics of the subdetectors.

The main task of the LVL-1 trigger system is to correctly identify the bunch-crossing of interest. In the ATLAS experiment this is not a trivial task, since the dimensions of the Muon Spectrometer imply time of flight larger than 25 $ns$ and the shape of calorimeter signals extends over many bunch-crossings.

Moreover LVL-1 trigger also provides information on the position and $p_T$ range of candidate objects (Region of Interest).

Table 1.2: Example of LVL-1 trigger menu ($L = 10^{34} cm^{-2} s^{-1}$).

| Trigger | Rate (kHz) |
|---|---|
| Single muon, $P_t$ >20 GeV | 4 |
| Pair of muons, $P_t$ >6 GeV | 1 |
| Single isolated electromagnetic cluster, $E_t$ >30 GeV | 22 |
| Pair of isolated electromagnetic clusters, $E_t$ >20 GeV | 5 |
| Single jet, $E_t$ >290 GeV | 0.2 |
| Three jets, $E_t$ >130 GeV | 0.2 |
| Four jets, $E_t$ >90 GeV | 0.2 |
| Jet, $E_t$ >100 GeV AND missing $E_t$ >100 GeV | 0.5 |
| Tau, $E_t$ >60 GeV AND missing $E_t$ >60 GeV | 1 |
| Muon, $P_t$ >10 GeV AND isolated electromagnetic cluster, $E_t$ >15 GeV | 0.4 |
| Other triggers | 5 |
| Total | ≃40 |

Table 1.3: Example of LVL-1 trigger menu ($L = 10^{33} cm^{-2} s^{-1}$).

| Trigger | Rate (kHz) |
|---|---|
| Single muon, $p_t$ >6 GeV | 23 |
| Single isolated electromagnetic cluster, $E_t$ >20 GeV | 11 |
| Pair of isolated electromagnetic clusters, $E_t$ >15 GeV | 2 |
| Single jet, $E_t$ >180 GeV | 0.2 |
| Three jets, $E_t$ >75 GeV | 0.2 |
| Four jets, $E_t$ >55 GeV | 0.2 |
| Jet, $E_t$ >50 GeV AND missing $E_t$ >50 GeV | 0.4 |
| Tau, $E_t$ >20 GeV AND missing $E_t$ >30 GeV | 2 |
| Other triggers | 5 |
| Total | ≃40 |

The LVL-1 latency, namely the time spent to take and distribute the decision, is 2 $\mu s$, with an output rate of 75 $kHz$, increasable up to 100 $kHz$ (limit imposed by the design of the front-end electronics).

Events selected by LVL-1 are stored in Read Out Buffers (ROB), waiting for the LVL-2 decision. In case of positive decision, events are fully reconstructed and stored for the final decision of the Event Filter. The LVL-2 trigger level reduces

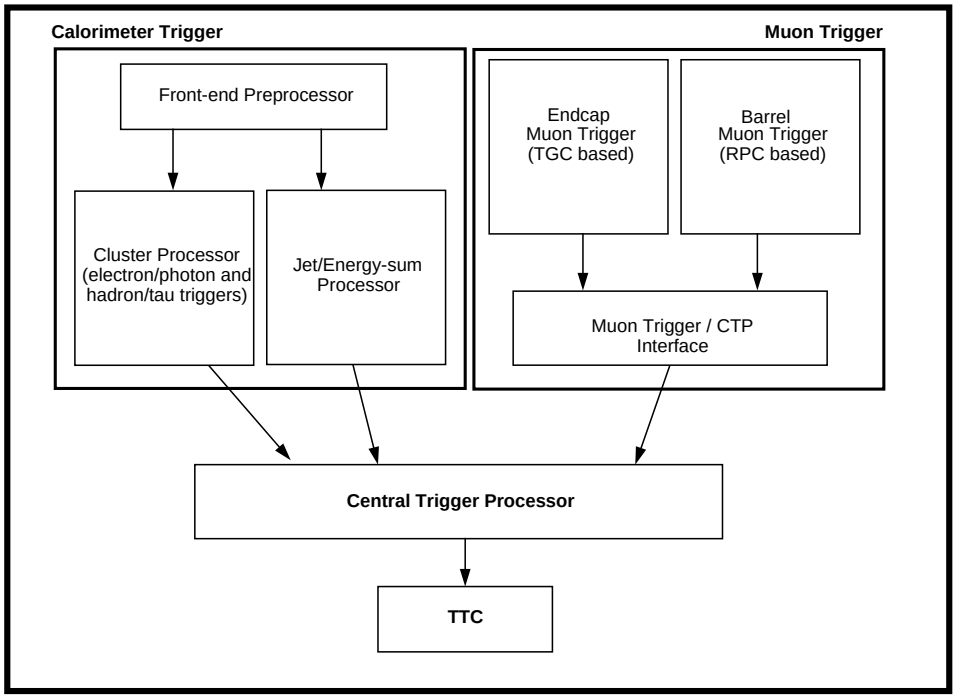


Figure 1.19: Block diagram of the ATLAS LVL-1 Trigger system.

the rate to 1 $kHz$, using also information from the Inner Detector. It has access to the full data of the event, with full precision and granularity, but its decision is taken considering only data from a small region of the detector, i.e the ROI (Region Of Interest) identified by the LVL-1. Depending on the event, the latency of LVL-2 can vary from 1 $ms$ to 10 $ms$.

Then the final trigger decision is taken by the Event Filter by means of off-line algorithms. The EF must reduce the rate to a level suitable for permanent storage, currently assumed to be $\sim$ 100 $Hz$ for a full event of size $\sim$ 1 $Mbyte$.

**The First Level Muon Trigger** is crucial for the on-line selection of events with high transverse momentum muons and for its correct association to the bunch-crossing of interest.

It receives as input the pattern of hit strips or wire-groups in the muon trigger chambers (RPCs and TGCs respectively). These data are used by a dedicated Muon Trigger System to decide whether muons above a given threshold were produced in an event. The sharpness of the $p_T$ cut applied by the trigger is mainly given by the information read out from the detectors in the bending pro-

jection. Therefore, the information in the non-bending view helps to reduce the background trigger rate from noise hits in the chambers produced by low-energy photons, neutrons and charged particles, as well as localizing the track candidates in space, as required for the LVL-2 trigger.

The basic principle of the muon trigger algorithm requires a coincidence of hits in the different chamber layers within a road. The width of the road is related to the $p_T$ threshold to be applied. Space coincidences are required in both views, with a time gate close to the bunch-crossing period (25 $ns$). The muon trigger algorithm is described in chapter 4.

The information from all the sectors is combined in the muon-trigger interface to the Central Trigger Processor (MUCTPI). This counts the number of muon candidates for each of the six $p_T$ thresholds, and passes the multiplicity information on to the Central Trigger Processor (CTP).

Finally in the CTP the input data are combined to form decisions for each menu item using lookup tables.

# Chapter 2

# An ATLAS LVL-1 muon trigger detector: the Resistive Plate Chamber

## 2.1 The Resistive Plate Chamber

The Resistive Plate chambers (RPCs) are able to detect charged particles through the measurement of the ionization in the gas, which a particle produces when traversing the active area of the detector. In order to collect the electrons and ions produced by ionization, a strong uniform electric field is applied, using a couple of resistive parallel plane electrodes.

The electrodes are usually made of a mixture of phenolic resins (usually called *bakelite*) with a volume resistivity $\rho$ from $10^9$ to $10^{12}$ $\Omega cm$. Glass can be used as electrode material as well. The plates are kept spaced and parallel by insulating spacers. The resulting gap is filled with an appropriate gas mixture. A sketch of a Resistive Plate Chamber is shown in figure 2.1. The electrode material, the plate thickness and the distance at which they are kept could vary depending on the experiment requirement. In this thesis the characteristics of RPCs for the ATLAS experiment are presented.

In the ATLAS experiment, the RPC bakelite plates are 2 *mm* thick and separated by a 2 *mm* gas gap. The gap height is made constant on the whole detector area by cylindrical spacers with 12 *mm* diameter, glued on both plates at $\sim$ 10 *cm* interval. A 7 *mm* wide frame of the same material and thickness as the spacers is used to seal the gap at all four edges.

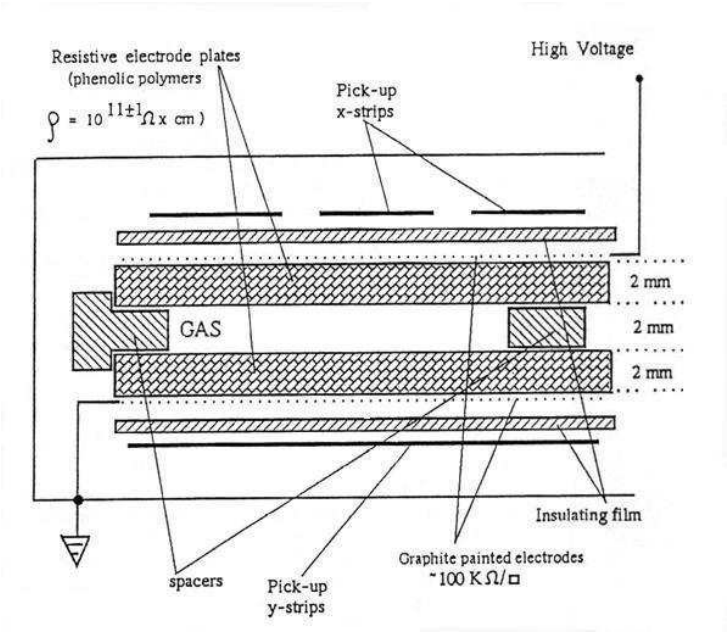


Figure 2.1: A Resistive Plate Chamber sketch.

The external plate surfaces are coated by thin layers of graphite painting. The graphite has a surface resistivity of $\sim 100\ k\Omega\square$, thus allowing uniform distribution of the high voltage along the plates, without creating any Faraday cage that would prevent signal induction outside the plates (as would happen using metallic electrodes, for example). Between the two graphite coatings is applied a high voltage of about 10 $kV$, resulting in a very strong electric field ($\sim 5\ kV/mm$) which provides avalanche multiplication of the primary electrons, produced by ionization due to the incident particle. In presence of such a high electric field, electrode surface irregularity can create local field effects, causing noise in the detector. To avoid this problem the inner surfaces are covered by a thin layer of linseed oil, which makes them smoother.

While the discharge electrons and ions drift in the gas towards the anode and cathode respectively, the signal is induced on pick-up copper strips, supported by the electrodes and electrically isolated by a 200 $\mu m$ thick insulating film. The signal is read-out via capacitive coupling and processed by the front-end electronics, composed in two steps: amplification and discrimination with respect to a fixed threshold.

For the ATLAS experiment, each chamber is made from two detector layers and four read-out strip panels (each couple of panels are arranged with the strips

orthogonal, for measurements of the $\eta$ coordinate and the non-bending one). The two elements are rigidly held together by two support panels, which provide the required mechanical stiffness of the chambers.These panels are made of paper honeycomb sandwiched between two aluminium sheets. One panel is flat, 50 *mm* thick, with 0.5 *mm* thick aluminium coatings; the other panel is 10 *mm* thick with 0.3 *mm* coatings and is preloaded with a 1 *cm* sagitta. The two panels are rigidly connected by 2 *mm* thick aluminium profiles, such that the preloaded support panel provides uniform pressure over the whole surface of an RPC module. The mechanical structure of an ATLAS RPC chamber is presented in figure 2.2.

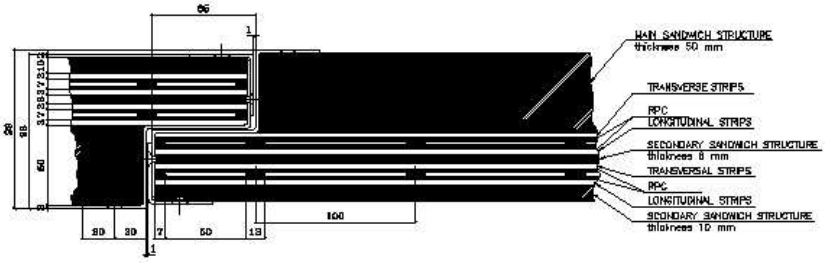


Figure 2.2: Mechanical structure of an ATLAS RPC chamber.

## 2.2 Avalanche growth and streamer development in RPC gas gap

In the RPC gap the electrons produced by first ionization are subjected to the strong electric field which drifts them toward the anode. Along their path they collide with other electrons or gas molecules in the medium. Between two consecutive collisions, an electron can increase its kinetic energy enough to generate a secondary ionization. The electrons liberated in this secondary ionization are also accelerated to produce still more ionization and so on. The avalanche multiplication mechanism, characterized by an exponential growth, initiates.

The mean free path of electrons in the gas medium is $\lambda = 1/\alpha$, where $\alpha$ is the first Townsend coefficient. Defining $n$ the number of electrons drifting in the gas at a fixed time, the increment $dn$ obtained after a displacement $dx$ is

$$dn = n\frac{dx}{\lambda} = n\alpha dx.$$

By integrating over a path along $x$, the total number of free electrons is

$$N = n_0 \cdot e^{\alpha x} = n_0 \cdot e^{\alpha v_d t}$$

where $v_d \sim 50\,\mu m/ns$ is the drift velocity of electrons in the gas, depending on the gas mixture and on the intensity of the applied electric field.

Assuming the electric field constant and uniform implies a constant Townsend coefficient during the avalanche multiplication. But when the spatial charge density of the avalanche is large enough to provide distortions of the field itself, the Townsend coefficient depends on $x$, and the integral of $\alpha(x)$ on the walked path substitutes the constant exponential in the previous expression.

If the avalanche reaches a multiplicity of $\sim 10^6$ electrons, the charge distribution is such that, inside the avalanche, electrons are not accelerated anymore and stop to contribute to multiplication. A sort of dynamic equilibrium is reached: a *saturated avalanche* approaches the anode without increasing anymore. It is the so called *saturated regime* [21].

For extremely high values of the electronic charge (established by Meek in $\sim 10^8$ electrons for noble gases), the avalanche becomes the precursor of a new process, called *streamer*. In this phase, the electrons have low kinetic energy and electron-ion recombination can occur with photon emission. Then the photon produced can further ionize the gas molecules, restarting one more avalanche multiplication, but delayed with respect to the first one. When the number of photons is large and the electric field strong enough, there are several restarting avalanches until the local density and electrons and ions distribution are such to connect the two electrodes. An extremely high current flows in the gas ($\sim$ 100 times larger than the typical avalanche), until all the electrons and ions are collected.

The streamer does not evolve in a spark because of the electrodes resistivity, and it is prevented from propagating transversely by the presence of an opportune photon quencher in the gas mixture.

Streamer signals are therefore greater and easier to detect, but also longer in time and with a higher charge per count. In particular, this last characteristic limits the rate capability of the detector operating in streamer mode to a few hundred of $Hz/cm^2$.

Adopting gas mixtures based on electronegative components allows to retard the appearance of the streamer in terms of the applied electric field [15][16][17]. Then the introduction of a quencher (as $SF_6$) removes the streamer, allowing to work in a pure avalanche mode [13].

Avalanche and streamer modes are two different working modes for RPCs.

## 2.3 The gas mixture

The role of the gas mixture in the RPC operation is crucial. The first ionization extraction potential, the first Townsend coefficient, the electronegative attachment coefficient determine the avalanche multiplication, the presence and the relative importance of photoproduction, the range from the saturated avalanche to the streamer mode. The gas mixture influences the working mode of the RPC, resulting in different characteristics and performances of the detector.

The filling gas is usually composed by an optimized mixture. To operate the chamber in streamer mode, the main gas component should provide a robust first ionization and a large avalanche multiplication, even at low applied field. One typical element is Argon, which ensures great avalanche increase with electrons abundance: a good situation for starting streamer production. To work in avalanche mode, instead, the main component should be an electronegative gas, with high enough primary ionization production, but with low free path for electron capture. The high electronegative attachment coefficient limits the avalanche electrons number below the Meek limit. A gas showing these characteristics is the Tetrafluorethane ($C_2H_2F_4$).

Another component is a polyatomic gas, usually a hydrocarbon, which has a high absorption probability for ultra violet photons, produced in electron-ion recombinations. This component allows to dissipate the photon energy by rotational-vibrational energy levels, avoiding photoionization with related multiplication and limiting the lateral charge spread.

Significant variations in environment variables, as temperature and pressure, change the characteristics and properties of the filling gas (as the density $\rho$, for example), then influence the ionization and multiplication processes. As a consequence, RPC performance at the same applied voltage but in different environmental conditions could be not comparable. In order to set the detector working point with accuracy and to be able to recreate the same working conditions, the applied voltage value ($HV_{app}$) is normalized to a reference temperature ($T_0 = 293.15\ K$) and pressure ($P_0 = 1010\ mbar$) values, according to the formula [11][12]:

$$HV_{eff} = HV_{app}^{T_1,P_1} \frac{T_1}{T_0} \frac{P_0}{P_1}.$$

This correction can be justified with the hypothesis that the gas discharge related phenomena are invariant for any $P$, $V$, $T$ change, which leaves the ratio of the voltage over the gas density unchanged.

## 2.4 The resistive electrodes

The RPC can be schematized as two dielectric planar capacitors [18] and, taking into account the finite resistivity of the plates, the model can give an idea of the time involved in the signal formation process.

The equivalent simplified circuit is shown on the left in figure 2.3. $R$ and $C$ account for the resistive electrodes, while $C_g$ and $R_g$ for the gas gap. Being $R_g \gg R$, in absence of ionization in the gas, the voltage is entirely applied on the gas gap.

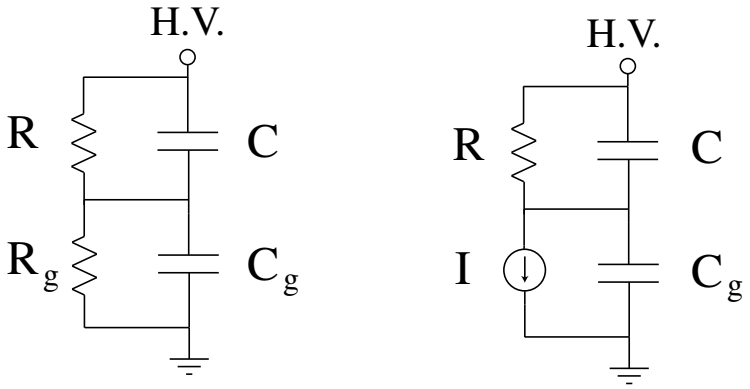


Figure 2.3: Equivalent circuit of the "discharge cell" in the RPC: in absence of ionization (on the left) and when a ionizing particle crosses the gap (on the right).

When the gas is crossed by an ionizing particle, the electric discharge in the gas can be schematized as a current generator which discharges the "gas capacitor" $C_g$ (see figure 2.3 on the right), so that the voltage initially applied to the gas is transferred to the resistive plate described by the capacitor $C$ in figure 2.3. The typical discharge duration is of the order of 10 $ns$. In such a short time the resistive electrodes behave like insulators, obstructing the feeding of the discharge in the gas and, in presence of a streamer, preventing the spark. On this quenching mechanism is based the working principle of the detector.

Then the system goes back to the initial condition, discharging the electrode capacitor $C$:

$$\frac{dq_C}{q_C} = -\frac{dt}{R(C + C_g)}$$

with a characteristic time ($\tau$) depending on geometric parameters (the plate thickness $d$ and the gap thickness $g$), on the dielectric constant $\varepsilon_r$ and on the bakelite

resistivity $\rho$:

$$\tau = R(C + C_g) = \rho\varepsilon_0\left(\varepsilon_r + \frac{2d}{g}\right).$$

Typical value for $\tau$ is $\sim$ 10 $ms$ (for $\rho \sim 10^{10}\Omega cm$), three orders of magnitude greater than the discharge duration. The $\tau$ value is the dead time of the detector and has to be noted that it is indeed limited just to a small area of the detector, that is a consequence of having resistive electrodes. With metallic electrodes the area at null field would have involved the full detector surface, and the restoring time would have been much longer.

Then a chamber with resistive electrode plates is intrinsically divided in a large number of small effective "discharge cells", independent from one another. The area of each cell is proportional to the total charge $Q$ produced in the gas gap:

$$S = \frac{Qg}{\varepsilon_0 V}$$

where $V$ is the applied voltage.

The charge $Q$ is crucial for the detector rate capability: since the discharge occurring in the gas can only be fed by a limited current across the electrodes, a small value of $Q$ allows therefore to keep the operating current small and at the same time, if the signal is accurately amplified, the efficiency high; even in presence of an intense flux of ionizing particles.

## 2.5 Pick-up strips and read-out

The pick-up strips behave as signal transmission lines of well defined impedance, and allow to transmit the signals at large distance with minimal loss of amplitude and time information. Strips are terminated at one end by front-end electronics and on the other end by proper resistor to avoid reflections. Since the strips allow the signal to propagate in the two opposite directions, induced charge is split in two parts, reducing the readable signal by one half.

The read-out electrode can be described as a current generator charging a parallel RC circuit. The resistor $R$ connecting the line to the ground is half the line impedance. The electrode capacity $C$ is proportional to the pick-up area determined by the spatial distribution spread of the induced charge. The time constant $\tau = RC$, for typical values of these parameters, is of the order of tenths of $ps$, much shorter than the rise time of the signal.

Finally, with simple calculations it is possible to observe that the current injected in the strip is, at any time, proportional to the current of the discharge in the gap.

The ion contribute to the current is essentially negligible with respect to the electron one, due to the different mobility; therefore only electrons give a prompt signal. Assuming the liberated electrons uniformly distributed along the gap depth, $n$ is defined to be the number of produced electrons per unit length. At an instant $t$, all the primary clusters produced at a distance $x > v_d t$, being $v_d$ the drift velocity, were absorbed, while all the others had a gain $\sim e^{\alpha v_d t}$. Then the total number of electrons in motion in the gap at the time $t$ is:

$$N(t) = n(g - v_d t)\, e^{\alpha v_d t},$$

and the current induced on the pick-up electrodes is:

$$i(t) = eN(t)\frac{v_d}{g} = ev_d n\left(1 - \frac{v_d t}{g}\right)e^{\alpha v_d t}.$$

Therefore the *prompt* charge $q$ is obtained by integrating the current up to the maximum drift time ($t_{max} = g/v_d$) [19]:

$$q = \int_0^{g/v_d} i(t)\, dt \approx \frac{eng}{(\alpha g)^2} \cdot e^{\alpha g},$$

that has to be compared with the total charge $Q$ liberated in the gap:

$$Q = \int_0^g ene^{\alpha x} dx \approx \frac{eng}{\alpha g} \cdot e^{\alpha g}$$

and result:

$$\frac{q}{Q} \approx \frac{1}{\alpha g}.$$

Considering the not negligible thickness of the resistive electrode plates between the gas gap and the read-out electrodes, the previous expression has to be correct. A simple calculation in which the plates and the gas gap are treated as three serially connected capacitors leads to one more factor on $q$, giving a total ratio of

$$\frac{q}{Q} = \frac{1}{\alpha g}\left[1 + \frac{2d}{\varepsilon_r g}\right]^{-1}\frac{1}{2}.$$

Here is also expressed the factor $1/2$, which takes into account the induced signal splitting between the front-end and the terminating resistor.

## 2.6 The choice of the avalanche operation mode

As previously discussed, RPCs can operate in *avalanche* or *streamer mode* [14].

Typical signal amplitude for an avalanche is $\sim 1\ mV$, with a duration of about 4 $ns$ and an average induced charge of $\sim 1\ pC$. On the contrary, the amplitude of signals induced by streamers is typically greater: $\sim 100\ mV$, with a duration of the order of 10-20 $ns$ and a charge of $\sim 100\ pC$.

Avalanche signals need a strong amplification and have high frequency components due to their very short duration. They are particularly difficult to detect. Streamer signals, instead, do not need any complex signal processing.

When a streamer occurs, both the charge and the detector area involved in the discharge are larger compared to the ones associated to an avalanche. As discussed in section 2.2, this effect implies a lower detector rate capability. Typical rate capabilities for RPCs working in streamer mode are of the order of 100 $Hz/cm^2$. This value can be increased reducing the charge released in the gas, i.e. working in avalanche mode, or decreasing the plate resistivity.

By carefully choosing the gas mixture, it is possible to obtain a stable avalanche working mode, with a large operating voltage plateau, not contaminated by streamers. Using a sophisticated read-out electronics, which allows to detect the small and fast signals generated by avalanches, detector can reach rates capabilities up to 1 $kHz/cm^2$. This is indeed the rate capability fully satisfactory for the ATLAS experiment for muon trigger chambers, and it is why has been decided that ATLAS RPCs have to work in avalanche mode. For this reason, the chosen gas mixture is substantially (94.7%) composed of Tetrafluorethane ($C_2H_2F_4$), because of its properties of electronegative gas; then a small percent (5%) is Isobutane ($C_4H_{10}$); and the remaining 0.3% is $SF_6$, which acts as quencher and removes the streamers, allowing to work in a stable avalanche mode with respect of the applied voltage [13].

Avalanche operation is also safer for what concerns the detector ageing effects, which depend on the total integrated charge.

The detector ageing is, in fact, strictly related to degrading of electrical and resistive properties of bakelite electrodes, because of chemical reactions of the conduction ions with bakelite. Degrading of electrodes influences the detector performances, reducing the rate capability [20]. Lower average charge per count means lower current flux through the detector and therefore a slower ageing, so in long experiment is preferable the avalanche operation mode.

## 2.7 Time and spatial resolution

The RPCs spatial resolution depends both on the read-out geometry and electronics. Using an analogic readout, it is possible to obtain resolution of $< 1\ cm$, but with a digital read-out the resolution is limited by the strip width, of the order of a few centimeters.

Concerning time resolution, it is natural to compare RPCs with wire detectors. The drift times in the radial electric field are different for different clusters, depending on their distance from the wire. The signal duration can be as long as hundreds of $ns$ and is fixed by the cluster at maximum distance from the wire. On the contrary, the high and uniform electric field applied to the gas gap is the same for all primary clusters, producing at fixed time the same exponential growth, limited by the distance of the primary clusters from the anode. The signal at any time is the sum of simultaneous contributions from all primary clusters multiplications. The resulting time jitter for detectable signals is always $< 2ns$.

The excellent time resolution make the RPC a very good candidate for trigger detector.

# Chapter 3

# Test results of the ATLAS RPCs

All the ATLAS subdetectors have to be extensively tested before the installation, given the extreme difficulty in accessing instrumentation in the ATLAS cavern, during ten years of data taking.

Each ATLAS RPC unit went through a set of quality controls using cosmic rays, before to be sent to CERN for integration and installation on the experiment. Test stands were built in the three Italian INFN laboratories of Lecce, Napoli and Roma Tor Vergata, which were responsible for the RPC production.

The Barrel Out Large (BOL) units, which are the largest RPCs, were tested in the *INFN Roma Tor Vergata Laboratory* from May 2005 until July 2006. The test stand, the quality assurance program and the final results of the Roma test stand are here presented.

Moreover tests with muon and pion beams has been performed at the CERN H8 site, where a complete ATLAS-like muon sector with six RPC units and three MDT chambers was assembled in a test area. The presence of the tracking chambers combined with the RPCs allowed further study of the RPCs performances, using the information extracted from the reconstructed muon track.

## 3.1 The cosmic test stand at the *INFN Roma Tor Vergata Laboratory*

In the *INFN Roma Tor Vergata Laboratory* a cosmic ray test stand for BOL RPCs has been built. The mechanical structure, shown in figure 3.1, can host two blocks of four superimposed RPC units. Indeed in the assembly laboratory the RPCs were grouped in self-sustaining blocks of four units. In principle the blocks had

not to be dismounted up to the final shipping at CERN.


Figure 3.1: Photo of the cosmic test stand at the *INFN Roma Tor Vergata Laboratory*. Two blocks of four superimposed biggest RPC units can be hosted. Up to 3854 channels are read out.

The BOL units have all the same length of 5.08 $m$ and width ranging between 0.76 $m$ to 1.12 $m$. Their weight measures up to 150 $kg$. As described in chapter 2, an ATLAS RPC unit is a mechanical structure consisting of two superimposed independent detector layers, each one made of two gas volumes. A gas volume is read out by two orthogonal strip panels, one for the $\eta$ view and the other for the $\varphi$ view. In total a BOL unit has 320 $\varphi$ channels and 96 or 128 $\eta$ channels, according to its width. The two gas gaps per layer are serially fluxed and have a single gas in/out-let. The standard ATLAS gas mixture was used in the test: $C_2H_2F_4$:94.7%, $C_4H_{10}$:5%, $SF_6$:0.3%. Moreover the power distribution inside the BOL is made of 8 Low Voltage (LV) inputs (VEE) which power the Front End (FE) electronics, 8 FE electronics thresholds (Vth), 4 High Voltage (HV) power connections and 4 gap current (Igap) monitors.

### Set-up and data acquisition system

The RPC test stand is equipped with:


Figure 3.2: Photo of the control panel used in the test. The 16 gas bubblers to monitor the gas flux are on the top. The bubblers are made of a single oil vessel receiving the 16 gas outputs. A only output line leads the gas out of the laboratory. LV connections are visible on the bottom.

- A gas system composed of a central control unit piloting four mass flow meters, which provide up to 600 $ml/min$. Flow is split up to 16 input channels. Output channels are connected to bubblers in order to check each gas flux line independently (see figure 3.2).

- A Detector Control System (DCS) monitoring all environmental and detector parameters.

- An industrially produced controller "CAEN SY2527" piloting 2 distinct HV channels, each one feeding up to 16 gas gaps and set via DCS.

- 5 LV power supplies feeding all the 64 FE VEE and Vth inputs.

- All LV, HV and signal cables.

- 56 receiver boards, each one of 64 channels (designed by *INFN Roma Tor Vergata*) converting the front end electronics outputs into shaped low voltage TTL signals.

- 38 latch boards (designed by *INFN Lecce*), each one with 96 channels, reading the hit patterns from the receiver boards every 15 $ns$ and storing them in a $31\times15$ $ns$ internal pipeline.

- A NIM coincidence and trigger logic system. It elaborates the fast-OR signals produced by the latches and generates the common-STOP signal to pause the latch read-out, during the data acquisition.

- A Labview PC based data acquisition (DAQ) system permitting to perform automated acquisition run. The PC accesses to the latches via VME crate with commercial VME master boards.

A photo of the racks hosting the HV and LV power supplies, the latches in acquisition and the NIM modules for the trigger logic is shown in figure 3.3.

The Detector Control System is based on a Windows PC running Labview. It controls 2 HV outputs each one feeding 16 HV inputs and it monitors 32 gap currents. The gas flow is continuously monitored for each component. If the gap currents or the gas composition run outside a properly defined safety ranges, the DCS immediately shuts down the HV power supply to avoid detector damaging.

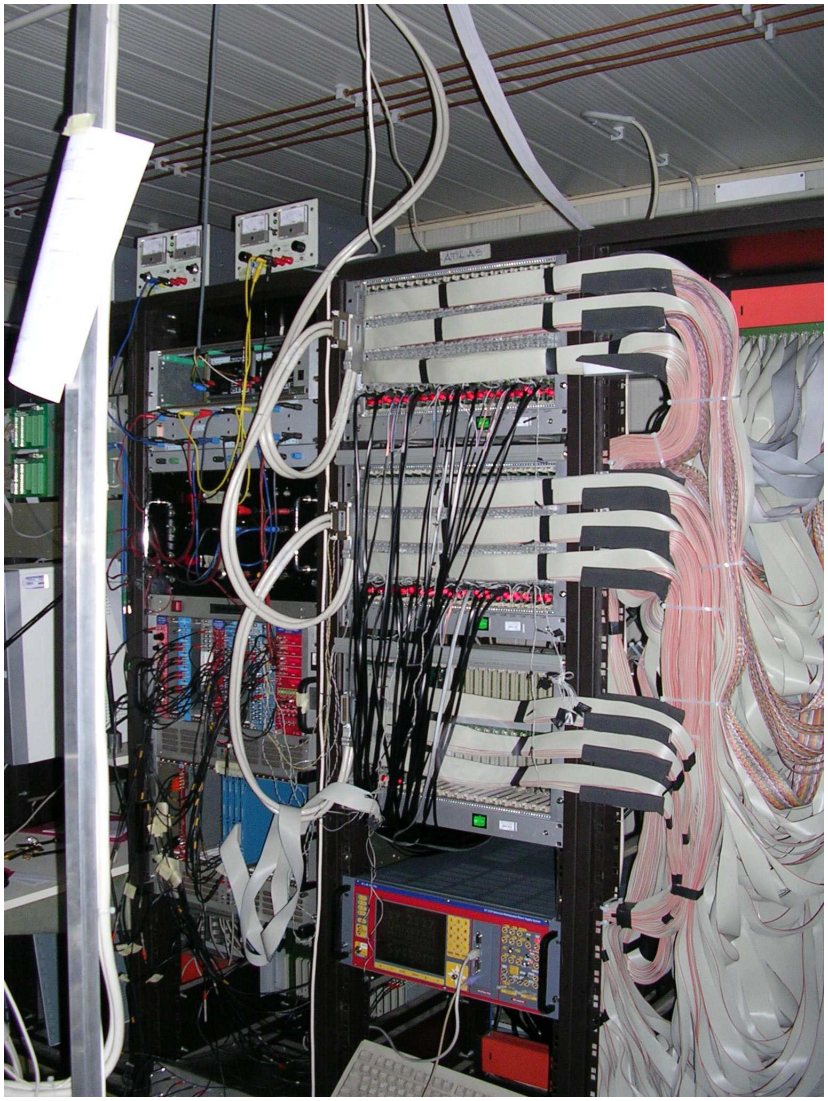

Figure 3.3: Photo of the racks with on the left the LV power system and the NIM modules for trigger logic; on the right the latches for data acquisition and the HV power system.

Moreover the Control System continuously monitors the environment parameters and makes automatical corrections of the applied HV for pressure and temperature variations, according to the formula 2.3 [11][12]:

$$HV_{eff} = HV_{app}^{(T_1,P_1)} \cdot \frac{T_1}{T_0} \cdot \frac{P_0}{P_1}.$$

where $HV_{app}^{(T_1,P_1)}$ is the set voltage value, $HV_{eff}$ is the effective voltage applied to the gas gap, $T_0$ and $P_0$ are the reference temperature (293.15 $K$) and pressure (1010 $mbar$), and $T_1$ and $P_1$ are the temperature and pressure measured during the test.

In figure 3.4 typical temperature and pressure trends are shown together with the monitored currents of the two power supply channels. The currents are compared with the sum of the 16 currents measured directly at the gaps the channel feeds. Not-zero difference (green points) between the 16 Igaps and the current measured by the power system could indicate some possible current leak, corresponding to currents flowing outside the gas gap.

Due to the large number of channels (more than 3500 read-out channels) and services under test, a careful check of test settings must be done before each data taking. On-line monitor displays have been developed to provide direct visualization of many involved parameters.

Both channel and time distribution can be displayed to check unplugged read-out connectors, to locate possible interchange and to focus dead channels before data taking. In figure 3.5, for example, the strip profile shows some dead channels. In particular an empty region of 4×8 strips between the strip 48 and the strip 81 is visible in the bottom $\varphi$ layer. This empty region corresponds to the last four FE boards (each FE board read out 8 strips) of the $\varphi$ read-out panel and indicates that a "bridge" for LV connection between the sixth and the seventh FE boards (counting from left) is broken. This RPC unit has therefore to be opened and repaired before sending it to CERN. On-line track display is a useful monitor to check trigger setting and data selection (figure 3.6).

Finally a display for measurement of the detector noise has been implemented. It provides time coincidences within 30 $ns$ between $\eta$ and $\varphi$ strips of the same gas volume. The $\eta$ and $\varphi$ coincidence allows to eliminate the noise due to electromagnetic contamination, leading just the noise due to spurious discharge in the gas volume, read out both by the $\eta$ and $\varphi$ views. A possible noisy spot is shown in figure 3.7 for $\eta$ strip 32 and $\varphi$ strip 1.

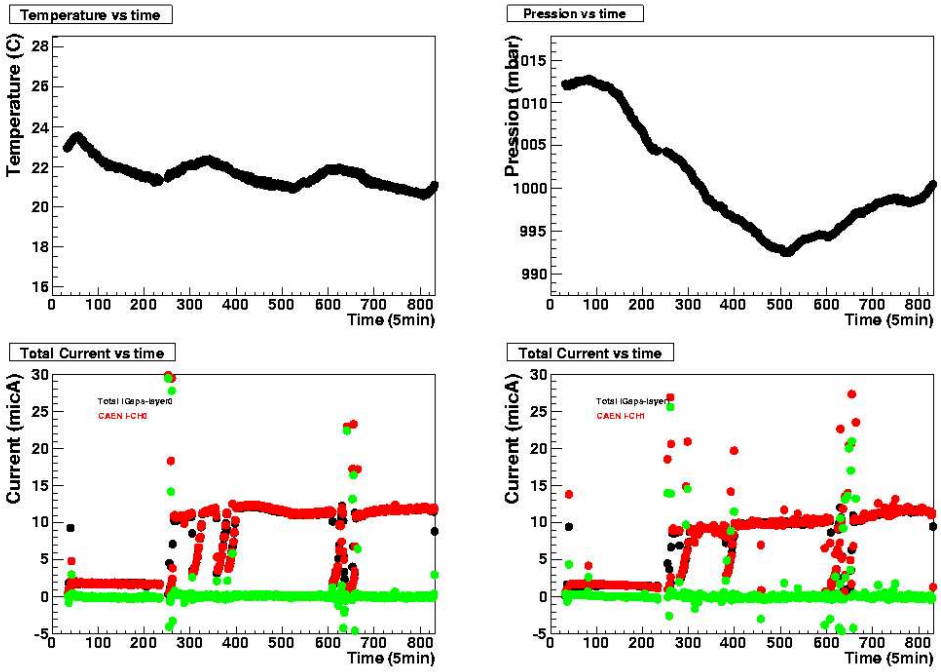


Figure 3.4: On the top the environment parameters are monitored. On the bottom gap currents are monitored in time. Current monitored by the HV power supply (CAEN) channel is compared with the sum of each single contribute: not-zero difference (green points) could indicate some current leaks to ground.

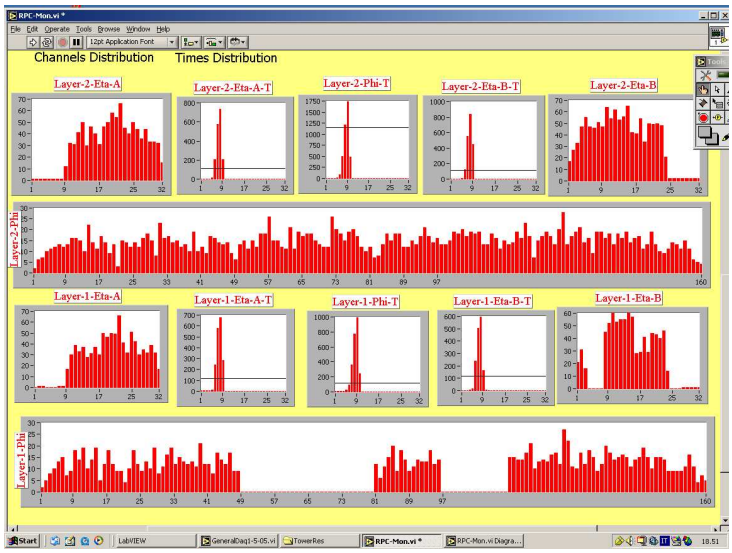


Figure 3.5: On-line BOL channel monitor to check all the strips of the two layers. The $\varphi$ strips of two close panels (each one of 80 strips) are shown together in the large plots. The $\eta$ strips are shown in the lateral profiles, each panel (with 24 strips) separately. In the middle the hit time distributions for the two views are shown. Some dead channels are visible in the bottom layer both for the $\varphi$ view and for the $\eta$ view on the right.

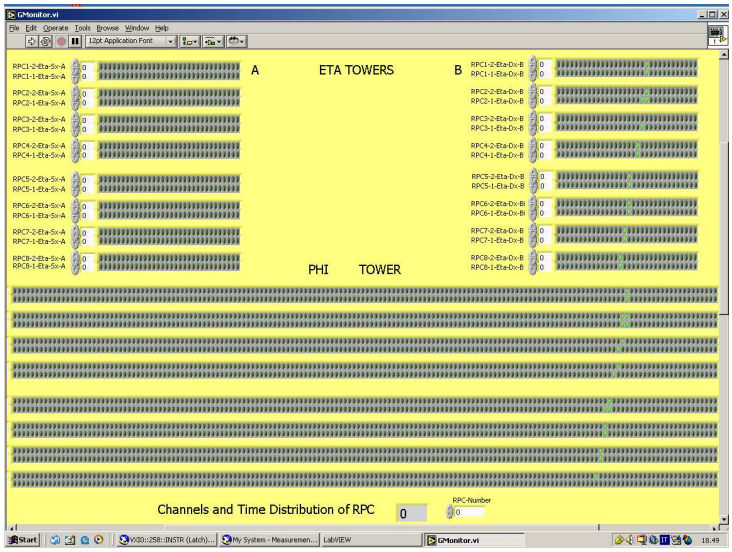


Figure 3.6: Event display: a track is visible in the $\eta$ view (up) and in the $\varphi$ view (bottom).

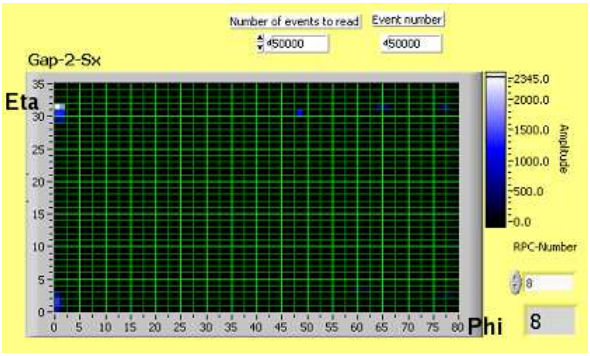


Figure 3.7: Display for measurement of the detector noise, performing time coincidences within 30 $ns$ between $\eta$ and $\varphi$ strips. The coincidence allows to eliminate the noise due to electromagnetic contamination, leading just the noise due to spurious discharge in the gas volume. A noisy spot is visible in the intersection between the $\eta$ strip 32 and the $\varphi$ strip 1.

**Debugging of the DAQ system**

The latch boards used for the data acquisition were home-made in a limited number at the beginning of the test activity. The BOLs were produced and tested at the end of the RPC mass production. Therefore a few defective latch boards were not replaceable resulting in few dead or bad performing DAQ channels

The effect of dead DAQ channels is visible in the frequency distribution of dead channels per test stand layer, shown in figure 3.8. A channel is dead if its efficiency is lower than 0.2. As shown in figure 3.8 there are 3 dead DAQ channels in the $\varphi$ panels and 1 in an $\eta$ panel. In the coarse of the test the efficiency of strip tested by the dead DAQ channels was renormalized.

A case of defective latch board producing a strip efficiency lower than the standard value is shown in figure 3.9. Connecting the same strips to a different latch board, a standard efficiency is measured.

The effect of bad performing DAQ channels is visible in the frequency distribution of RPC residual inefficiency per test stand layer in figure 3.10. The residual inefficiency is defined as the strip panel inefficiency subtracted of the fraction given by the number of dead panel strips over the number of panel strips. The average RPC inefficiency is $\sim 2\%$; larger value are due to DAQ system defects.

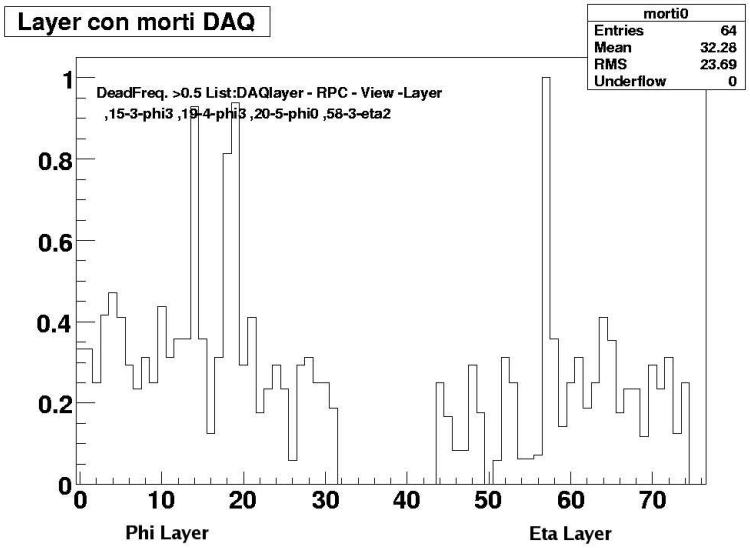


Figure 3.8: Dead channel frequency as a function of the test stand layer number ($\varphi$ layers range from 0 to 31 and $\eta$ layers from 44 to 75). Layers with frequency larger than 0.5 have some problems in the DAQ chain.

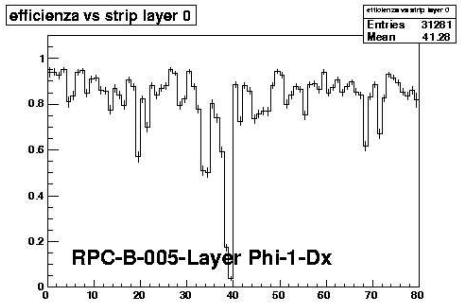


Figure 3.9: Efficiency strip by strip for the read-out panel of a RPC sited in the test stand slot 8. The frequency of this effect for RPC sited in slot 8 implies that is not a characteristic of the tested RPC, but it is due to a damage in the DAQ chain.

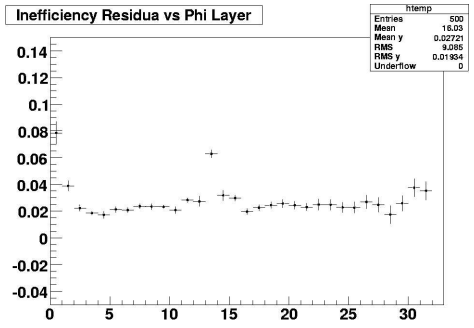


Figure 3.10: Inefficient residuals integrated on a large number of tested RPC units as a function of the test stand layer number.

### 3.1.1 RPC quality tests

The following test have been carried out on the BOL units:

1. Gas leak check;
2. Electronic DC test to check shorts and correct grounding and termination;
3. Gap current test;
4. Cluster size and detection efficiency test, including gas volume tomography;
5. Noise detector test.

The first two steps, gas leak check and electronics DC test, can be done before installing the RPC units on the test stands. The other tests instead require that RPCs are fluxed with the gas and fed by the power system, so the BOLs have to be arranged on the test station and correctly cabled. Before applying voltage to the gas volumes the RPC must be fluxed for at least 12 hours, corresponding to five complete gas volume exchanges.

### 3.1.2 Gas-tightness, electric DC and gap current tests

The RPC gas gaps are first checked for gas leak. Using a bubbler as a liquid manometer, a gas overpressure of about 2 *mbar* (a factor 4 larger than the standard ATLAS overpressure: 0.5 *mbar*) is created with 20 *mm* of water and the pressure for a RPC layer (which is made of two gas gaps) is measured by an electronic sensor for 15 minutes. The minimum pressure variation detected by the sensor is $\Delta P = 0.1$ *mbar*, which corresponds to a gas leak of $\Delta V = 6.7 \cdot 10^{-2}$ $cm^3$ in a minute, according to the formula:

$$\frac{\Delta V}{\Delta t} = \frac{\Delta P}{P} \cdot V \cdot \frac{1}{\Delta t} \tag{3.1}$$

where $P$ is the environmental pressure (1 *atm*), $V \simeq 10^4$ $cm^3$ is the volume of two gas gaps and $\Delta t$ is the test time (15 minutes). The RPC layer are accepted if the pressure variation measured in the test is lower than 1 *mbar*.

From a total of 192 tested BOLs, 11 units did not pass the gas-tightness test and they were opened and repaired. In the other cases the leak measured was of the order of 0.1 *mbar*, corresponding to a gas leak of $\sim$ 100 $cm^3/day$ in the standard ATLAS condition.

After the gas leak test a set of DC tests is performed. These tests are dedicated to check the correct installation and mounting of all on-chamber low voltage and high voltage connections and to verify correct grounding and termination.

The units showing defected electric connections were 15 units out of the 192 tested ones.

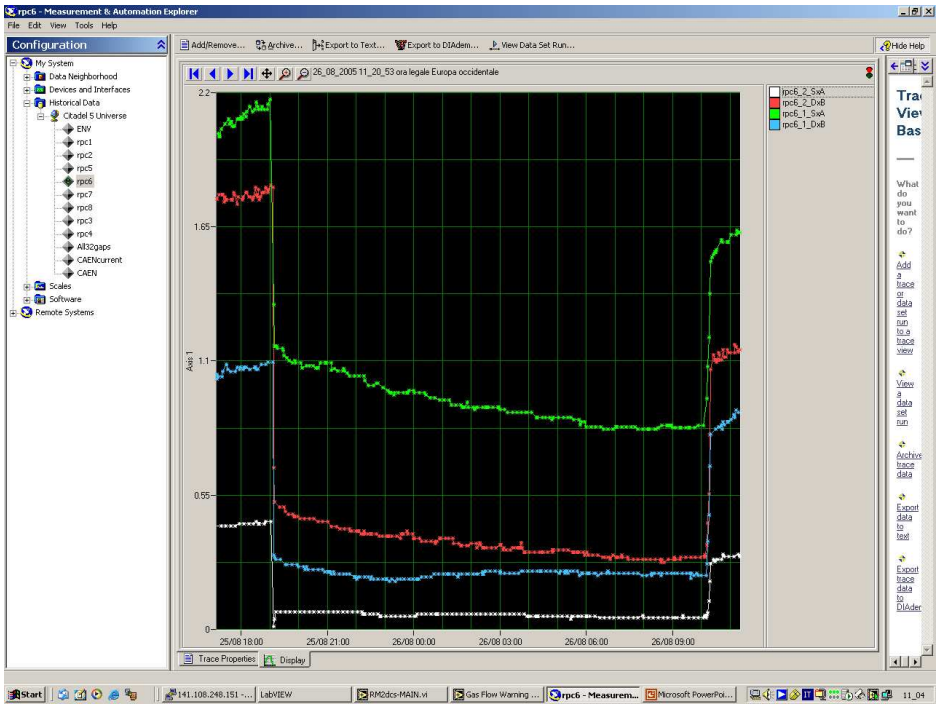


Figure 3.11: Four gas gap currents ($\mu A$) of a BOL unit are monitored for 15 hours. A conditioning process producing a decrease of the gap current is observable with different slopes in three gas gaps.

The eight BOLs, installed on the test station and fluxed for at least 12 hours with the ATLAS standard mixture, are first submitted to a preliminary gap current scan, raising the HV up to 7.5 $kV$, and then they are left at this voltage for about 12 hours. During this time a conditioning process producing a decrease of the gap current is usually observed (see figure 3.11).

Finally the Igap scan is repeated up to 10.2 $kV$ (corresponding to full efficiency in the avalanche regime). Typical Igap slopes as a function of the HV are shown in figure 3.12. The Igap vs HV plot shows a linear behaviour up to $\sim$ 7 $kV$ (ohmic trend), then the slope becomes steeper till the working point voltage (exponential trend). A gap is discarded if an excessive ohmic current is found, or if the current

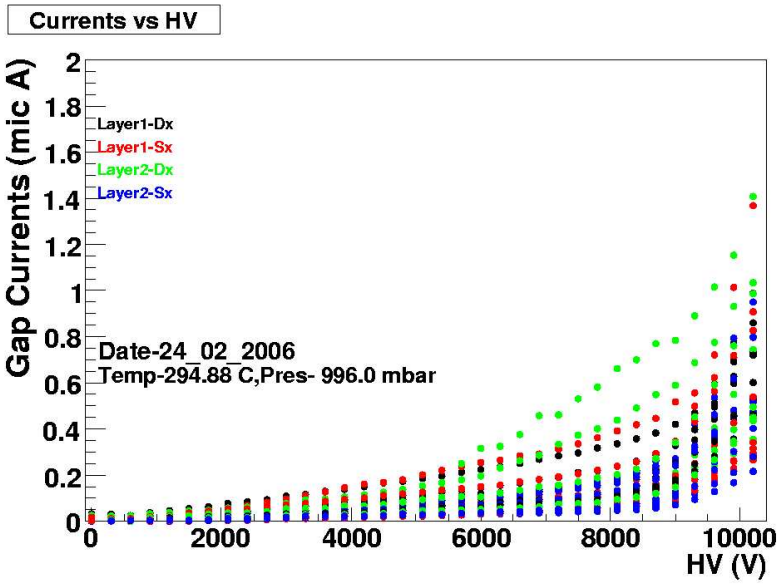


Figure 3.12: Gas gap current (the absolute value is plotted; the measured current has negative value) vs High Voltage scan. All the 32 gas volumes simultaneously under test are shown.

exceeds 3 $\mu A$, as shown in figure 3.13. In this case the gap is submitted to a further conditioning in the attempt to recover it, otherwise it is substituted.

In figure 3.14 an Igap vs HV plot is shown: an anomalously high current even at voltage as low as 4 $kV$ was observed. In this gap the current was associated to a significant noise counting rate, even at low voltage (6 $kV$), and by making coincidences between $\eta$ and $\varphi$ strips the noise source was localized inside the gas gap. The noise distribution of this gap is shown in figure 3.15: the noise is not uniformly distributed in the gap area, but it is concentrated in few points, referred as “hot spots”.

From a total of 192 tested units 22 were rejected due to excessive gap working currents. If after a further conditioning the gap current did not decrease, the RPC was opened and the gap was finally substituted.

### 3.1.3 Trigger and data acquisition

In order to check all the RPC performance, the developed test stand allow to carry out cosmic ray tests for studying a set of crucial parameters, like the cluster size and the detection efficiency. A relevant parameter is also the detector noise. The

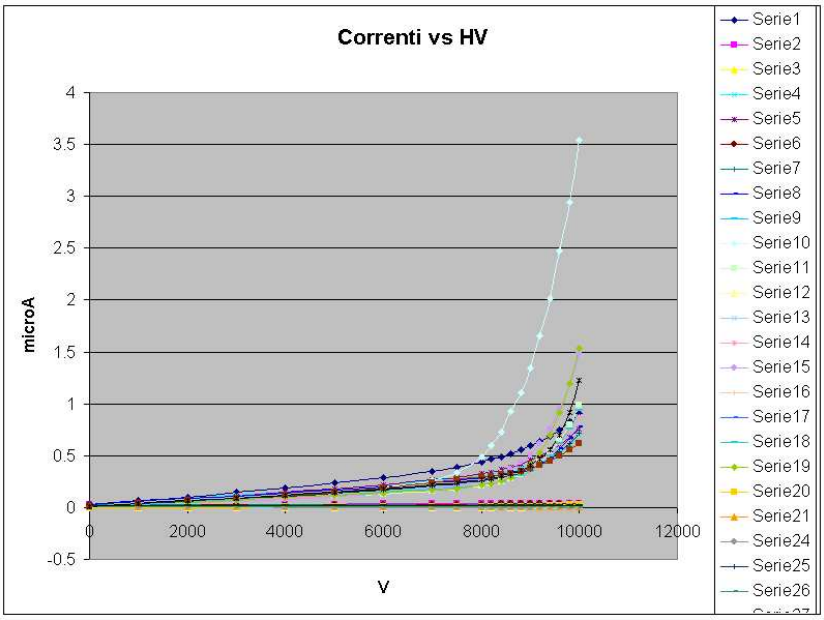


Figure 3.13: Gas gap current (absolute value) vs High Voltage scan. A gas volume shows an elevated current. This gap was submitted to a further conditioning in the attempt to recover it.

acquisition of both cosmic muons and noise signals requires an adequate trigger system. Three settings are available, according to the data acquisition goal:

1. a **random trigger** provided by a dual timer generating a periodical signal (for noise measurement);
2. a **noisy channel trigger** activated by the fast-OR of all the RPC layers (for noisy spot study);
3. a **cosmic ray trigger** obtained by a programmable coincidence of various RPC layers, with a fast-OR of all the $\varphi$ strips for each layer (for cosmic ray tests).

For the random trigger the signal period is fixed at 10 $\mu s$. This choice allow to minimize the acquisition time and to open the full available time window ($31 \times 15 = 465$ $ns$). In figure 3.16, on the left, the acquisition time as a function of the dual timer period is shown. The DAQ time is in plateau up to 1 $ms$. On the right the average hit time and the maximum hit time, expressed in number of latch bins (a latch bin is 15 $ns$ large), are shown as a function of the dual timer period. Trigger signals every 10 $\mu s$ ensure that all 31 latch bins are filled in each event.

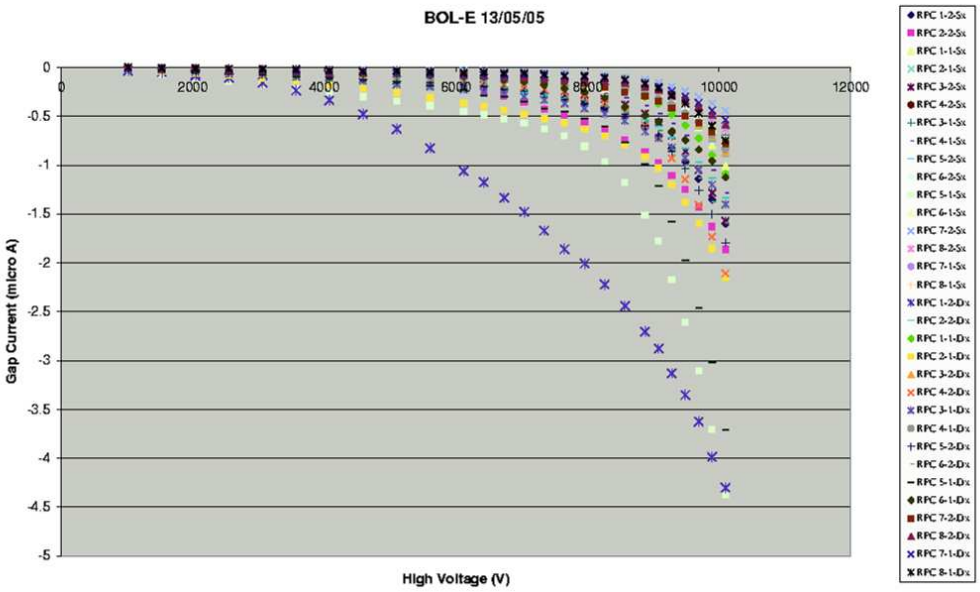


Figure 3.14: Igap versus HV scan. An anomalously high current even at voltage as low as 4 *kV* is observed.

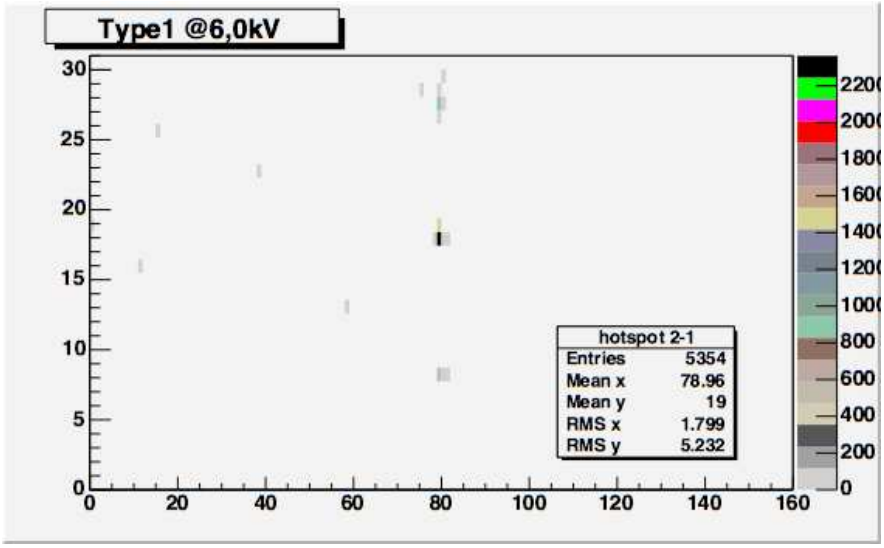


Figure 3.15: Noise distribution for the gap with the anomalous current shown above: the noise is not uniformly distributed in the gap area, but it is concentrated in few points (“hot spots”).

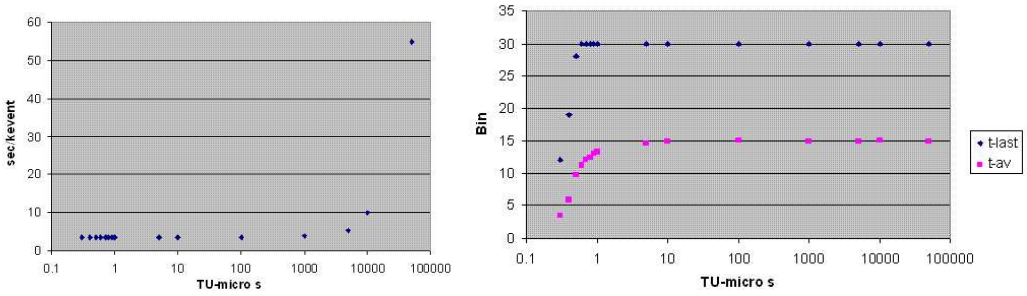


Figure 3.16: The acquisition time as a function of the dual timer (TU) period is on the left. The average hit time (t-av) and the maximum hit time (t-last), expressed in number of latch bins, as a function of the dual timer (TU) period are on the right.

The random trigger is used for measurement of noise counting rate, but the noisy channel trigger is more efficient for getting the noise distribution, because it allows to map possible noisy spot inside the gaps, by making via software the $\eta$ and $\varphi$ coincidences. The trigger rate for the case 2 depends on the noise of the eight BOLs under test and can vary between $10^3$ and $10^5$ *Hz* (16 layers correspond to about 80 $m^2$).

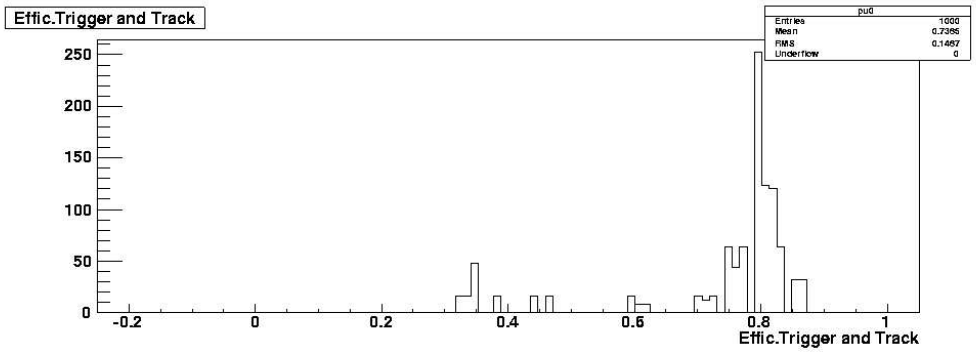


Figure 3.17: Trigger and tracking efficiency for cosmic ray tests. A "DAQ busy" signal should be introduced to avoid fake triggers.

For the cosmic ray trigger the layers chosen for the time coincidence are usually four (among the 16 under test): possibly two layers are chosen between the four upper units in the test stations and the other two layers between the four lower units, so to select almost vertical cosmic rays and ensure that track crosses all the RPC layers. In this configuration the trigger rate is about 350 *Hz*.

Since the acquisition chain has not a "DAQ busy" signal, a new trigger can be activated before the acquisition of the previous event is concluded, then a percentage of the acquired events could be fake. The ratio of the number of the reconstructed tracks over the total number of the acquired events for each run estimates the efficiency of both the trigger and the tracking algorithm (described in section 3.1.4). Averaging on all the acquired runs this ratio is 0.74 (see figure 3.17), therefore the fake triggers are less than 30% of the acquired events. Acquisition runs of $10^5$ cosmic triggers are acquired in order to ensure sufficient statistics for analysis, even at the strip level.

The data acquisition runs for the BOL tests are summarized in table 3.1.

| Measure | Trigger Setting | Acquisition | Events per run |
|---|---|---|---|
| Efficiency and | Cosmic ray trigger | HV scan | $10^5$ |
| Cluster size | Cosmic ray trigger | Vth scan | $10^5$ |
| Tomography | Cosmic ray trigger | standard | $10^6$ |
| Detector Noise | Random trigger | HV scan | $2 \cdot 10^5$ |
| | Random trigger | Vth scan | $3 \cdot 10^5$ |
| Hot Spot | Noisy channel trigger | HV scan | $3 \cdot 10^5$ |

Table 3.1: Data acquisition runs for BOL RPC test.

Efficiency and cluster size are studied both versus FE threshold and versus applied high voltage. The Vth scan is performed fixing the applied HV at 10.2 $kV$ (full efficiency) for all the units and varying the electronics threshold from 0.8 to 1.3 $V$. Because of the auto-trigger system the HV scan is performed in two steps to ensure independent measurements. First all layers 1 (the upper layer in a BOL unit) are left at 10.2 $kV$ producing trigger signals, while the voltage applied to layers 2 (the bottom layer in a BOL unit) is varied from 8.8 to 10.2 $kV$. Then the same procedure is repeated inverting the role of layers 1 with layers 2, triggering on layers 2 and studying the layers 1. During these scans the FE electronics threshold is set at the standard value of 1.0 $V$.

Scans vs HV and Vth are performed also to study the detector noise, but triggering with the dual timer (as explained before).

Moreover a specific high statistics run is dedicated to the gas volume tomography at standard working conditions, in order to check local inefficiency over the whole gap area.

Finally special runs are stored triggering on all RPC layers and varying the HV from 7.5 to 10 $kV$, to investigate possible presence of hot spots.

### 3.1.4 Cluster size and detection efficiency study

For each event RPC hits are collected, recording the hit strip number and the minimum and maximum hit time. A strip could have in principle more than one hit per event.

A cluster is defined as a group of adjacent fired strips; the number of strips in the cluster is the cluster size. The minimum and maximum cluster time are the minimum and maximum time of the strips belonging to the cluster. The cluster position is its geometrical centre.

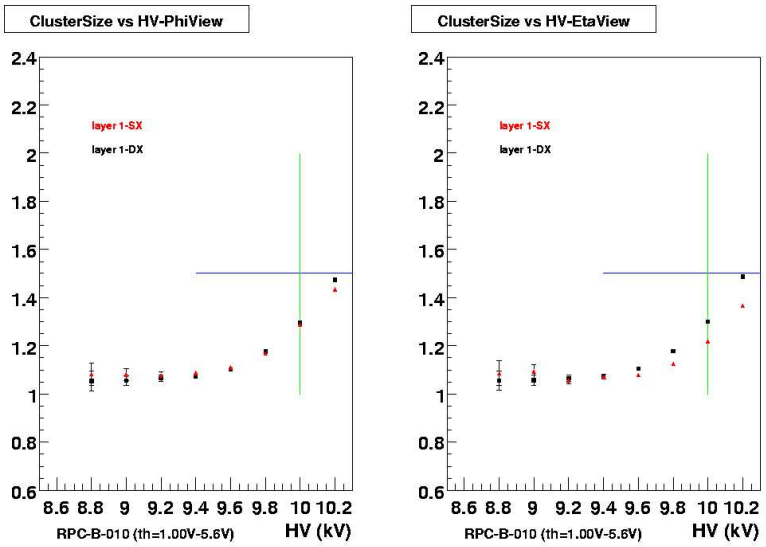


Figure 3.18: $\varphi$ and $\eta$ panel cluster size as a function of the applied High Voltage ($Vth = 1.0\ V$). The cross indicates the acceptance limit of cluster size (1.5).

The cluster size depends on the applied HV. In figure 3.18 the average cluster sizes for two strip panel in the $\varphi$ view (left) and in the $\eta$ view (right) as a function of the applied voltage are shown. The average cluster size value is lower than 1.5 strips up to 10.2 $kV$ in both views.

Moreover the cluster size depends on the FE electronics threshold. Cluster size as a function of the Vth is shown in figure 3.19 for $\varphi$ and $\eta$ panels. It has to be

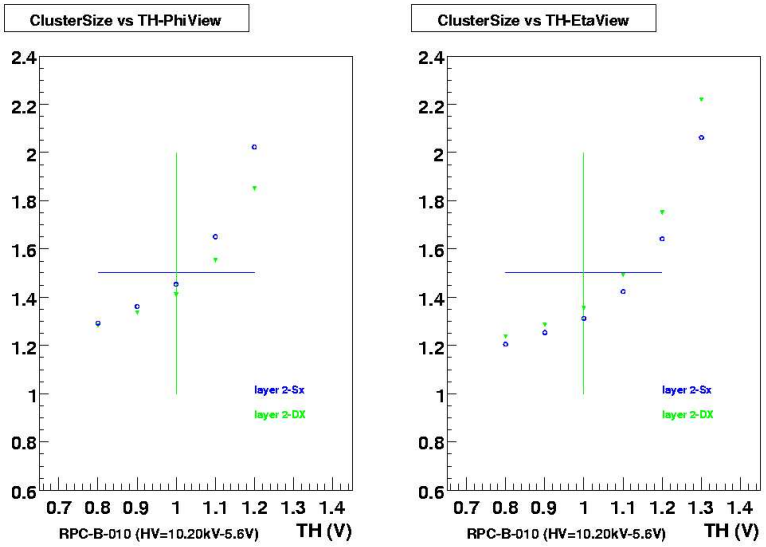


Figure 3.19: $\varphi$ and $\eta$ panel cluster size as a function of the FE electronics threshold ($HV = 10.2\ kV$). The cross indicates the acceptance limit of cluster size (1.5).

noted that the symbol Vth indicates a DC voltage level, which is used to polarize the FE electronics input (VEE). The physical discrimination threshold ($V_{phys}$) is given by

$$V_{phys} = \frac{V_0 - V_{th}}{A} \tag{3.2}$$

where $V_0$ is fixed and depends on the VEE and $A$ is the amplification factor ($\sim$ 700). The Vth of 1.0 $V$ for VEE of 5.5 $V$ corresponds to a physical threshold on the avalanche signal of about 1.2 $mV$. According to the expression 3.2, a larger value of Vth corresponds to a lower physical threshold level and vice versa. Therefore the cluster size increases for softer physical thresholds (larger Vth values) and at the standard threshold value $Vth = 1.0\ V$ the average cluster size is lower than 1.5 strips.

Track reconstruction is requested to evaluate the RPC detection efficiency. No dedicated trackers are in the test stand, but the large number of layers available in the test (16 normally) allows to make self-tracking. Usually of the two layers of the same unit: one is used for tracking (and trigger as described in section 3.1.3) and the other is studied.

The track reconstruction algorithm works in steps as follows:

1. At the the first step only the RPC layers chosen for triggering are considered. A first track fit is performed using only the layers (at least 3) showing a single cluster.

2. The track fit is repeated considering any cluster on trigger layers, which is the closer one to the first fitted track.

3. As last step a third fit is performed, taking into account all the layers with clusters centred at less than two strips from the previously fitted track.

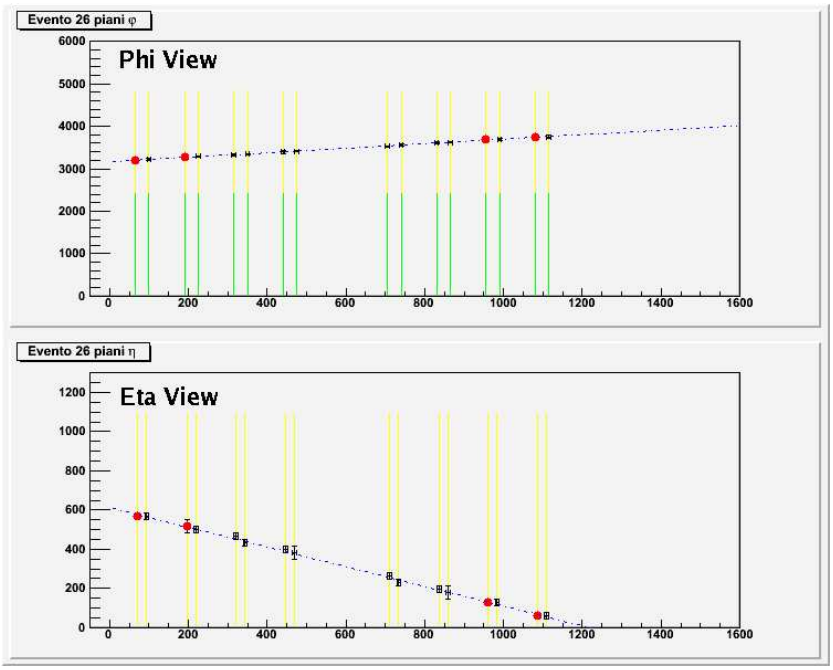


Figure 3.20: Cosmic muon track reconstructed with the RPC layers in the $\varphi$ and $\eta$ views.

The final fit is shown in figure 3.20. The procedure is performed on the two read-out views. If the track can be reconstructed on both the views, the event is selected for the efficiency study; otherwise it is rejected.

For each selected event a read-out panel is efficient if it has a cluster crossed by the reconstructed track, within a halo of half strip both on the left and on the right. Moreover in this case the strip intercepted by the track is defined as efficient.

Reconstructed track profiles (red) and cluster distributions (black) together with the resulting strip efficiency are shown in figure 3.21 for the $\varphi$ view and in

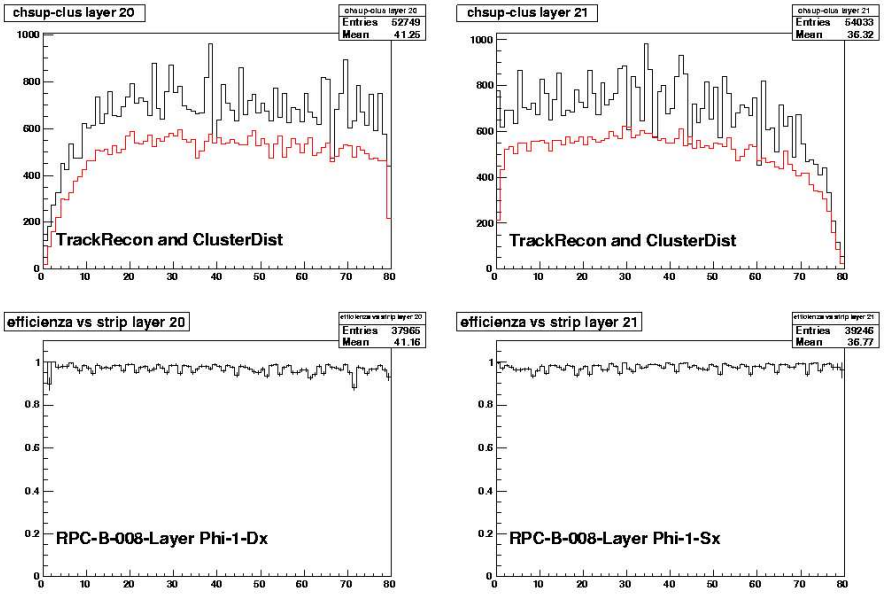


Figure 3.21: On the top track profiles (red line) and cluster distributions (black line) are shown for the $\varphi$ view. The strip efficiency resulted by comparing the cluster positions with the reconstructed tracks is on the bottom.

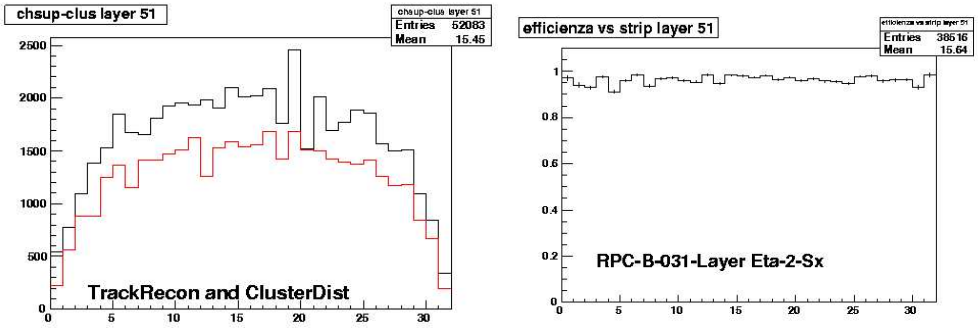


Figure 3.22: On the left the track profile (red line) and the cluster distribution (black line) are shown for the $\eta$ view. The strip efficiency resulted by comparing the cluster positions with the reconstructed tracks is on the right.

figure 3.22 for the $\eta$ view. The red lines reproduce the profile of the cosmic rays selected by the trigger.

A strip is tagged as "dead" if its efficiency is lower than 0.2. A read-out panel under test is rejected if more than 4% of its channels are dead. So up to 3 dead channels are allowed in $\varphi$ panel, and only 1 channel in $\eta$ panel.

The RPC efficiency is a parameter strictly dependent on the detector operation condition. In order to check the correct performance for each gas volume, the efficiency dependence on the applied HV and on the Vth is studied during the quality test, focusing on the full efficiency working point.

Panel efficiency as a function of the HV is shown in figure 3.23 for $\varphi$ and $\eta$ views. Read-out panels are discarded if the efficiency plateau does not reach 95%. In figure 3.24 the efficiency of a rejected panel is shown. Due to many dead channels in the panel, the layer efficiency does not over-cross the acceptance level.
The efficiency slope resulting with a Vth scan is in figure 3.25 for $\varphi$ panels on the left and for $\eta$ panels on the right. $\eta$ strips are more sensitive to the electronics threshold. All panels are fully efficient at the standard threshold value of 1.0 $V$.

High statistics runs allow to investigate the efficiency distribution on the whole gap area in standard condition (HV at 10.2 $kV$ and Vth at 1.0 $V$). The efficiency tomography for two BOL gaps of different dimensions are shown in figure 3.26. The gap shown on the left is fully efficient. The clear spots correspond to the insulating spacers, which systematically reduce the efficiency of about $\sim$ 1.1%. The gap on the right, instead, shows some inefficient regions at the gap edge. For this gap the current has standard behaviour, no hot spots are seen, so probably this inefficiency is due to an excess of the glue used in the gas volume manufactured.

### 3.1.5 Noise detector study

Noise study is performed by analysing data triggered by the dual timer set at 10 $\mu s$. Each acquisition corresponds to a time window of $31\times15$ $ns$. The noise rate per panel and per strip is measured inside this time window and normalized to the area.

Runs of 2-3 $\cdot 10^5$ acquisitions (see table 3.1) are stored in order to estimate the strip rate with an error lower than 20% down to 0.6 $Hz/cm^2$ on $\varphi$ strips (which have an area of $\sim$ 300 $cm^2$) and 0.2 $Hz/cm^2$ on $\eta$ strips (which have an area of 750 $cm^2$).

In figure 3.27 and 3.28 some strip rate profiles are shown. An $\eta$ strip panel with rate below 1 $Hz/cm^2$ on average is shown in figure 3.27. In the plots of

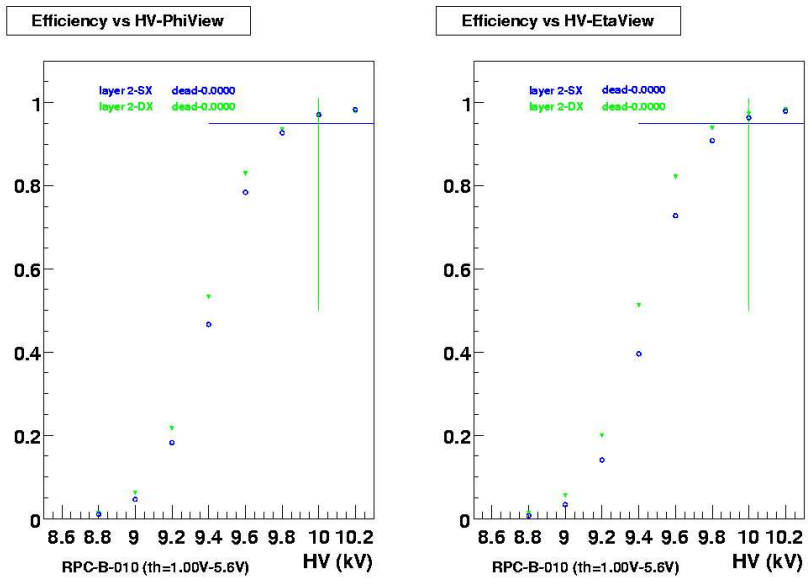


Figure 3.23: $\varphi$ and $\eta$ panel efficiency as a function of the applied High Voltage ($Vth$ = 1.0 $V$). The cross indicates the acceptance limit of the efficiency (95%).

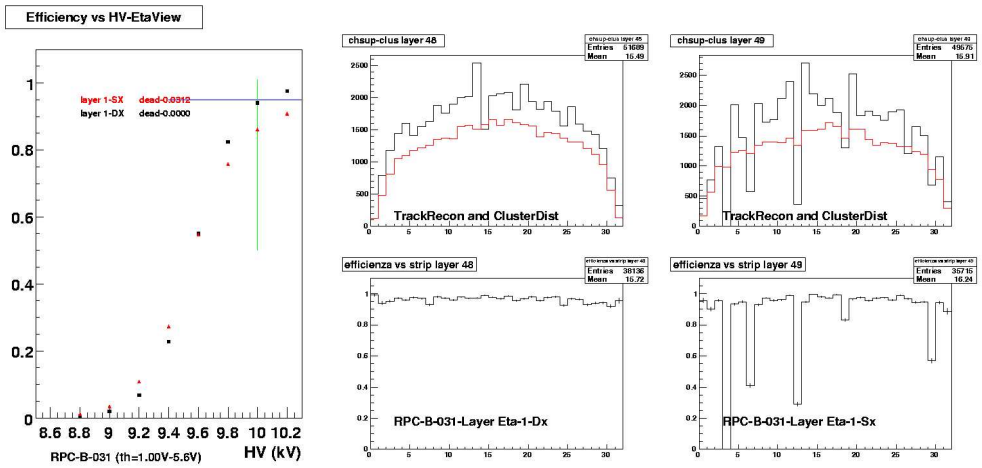


Figure 3.24: On the left the $\eta$ panel efficiency (two panels of a same layer) is shown. On the right the strip profiles (up) and the strip efficiencies (down) for the same panels are shown. One dead and four inefficient (< 85%) strips are clearly visible in one of the two panels. The acceptance limit is 1 dead or inefficient strip on the $\eta$ panels, therefore this unit was rejected.

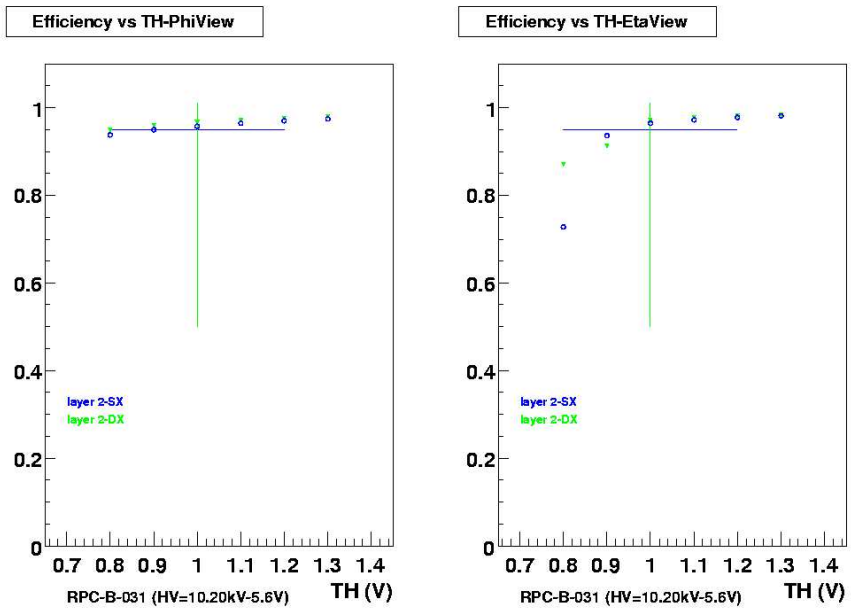


Figure 3.25: $\varphi$ and $\eta$ panel efficiency as a function of the electronics threshold ($HV = 10.2\ kV$). The cross indicates the acceptance limit of the efficiency (95%).

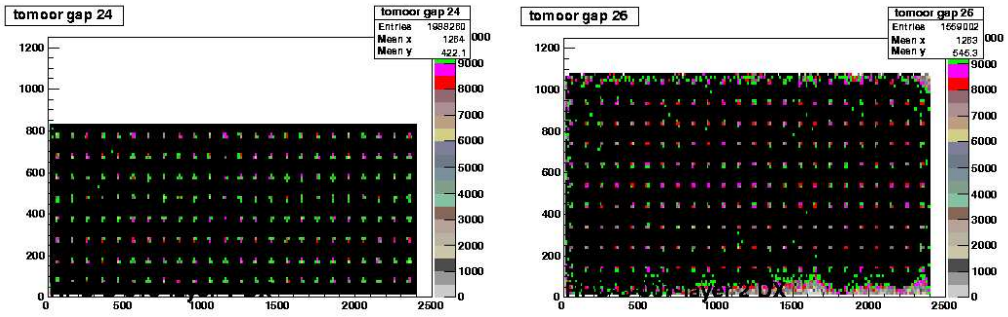


Figure 3.26: Efficiency gas volume tomography for two BOL units with different dimensions. The gap spacers are visible. On the right an example of a gas volume with some inefficient regions at the edge is shown.

figure 3.28 two $\varphi$ panels with noisy channels are shown. Noisy channels are frequently localized on the border and the corner of the panel (right plot), where the HV and gas in-lets connections are positioned.

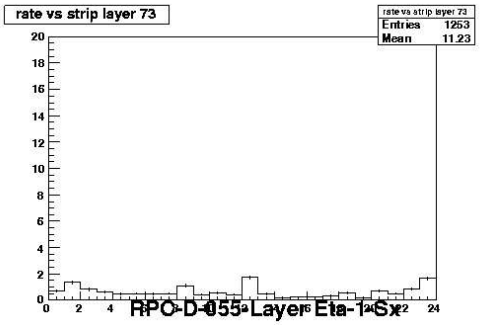


Figure 3.27: Noise rate ($Hz/cm^2$) for read-out strips.

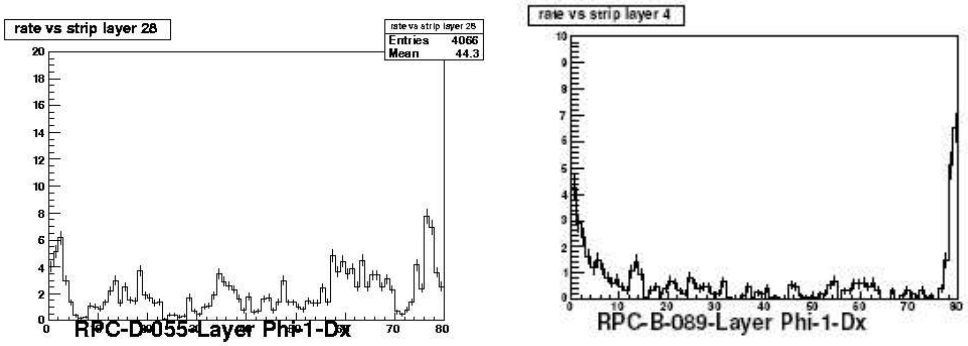


Figure 3.28: Two strip panels with out of standard strip rate ($Hz/cm^2$). Two causes has been observed: noise split on all strips (on the left) and localized in the edge (on the right).

The results of the HV scan for the noise rates are shown in figure 3.29 both for $\varphi$ and $\eta$ read-out panels. Rates below 1 $Hz/cm^2$ are measured up to 10.2 $kV$ in the two views.

In figure 3.30 the noise rate as a function of the electronics threshold is shown. In some cases the noise rate for $Vth = 1.3\ V$ exceeds the level of 1 $Hz/cm^2$, but this FE threshold value is well below the ATLAS standard value of 1.0 $V$. All the shown read-out panels were accepted.

The noise rate dependence on the gap current is studied in figure 3.31. A linear correlation is observable in both views. This observation supports the interpreta-

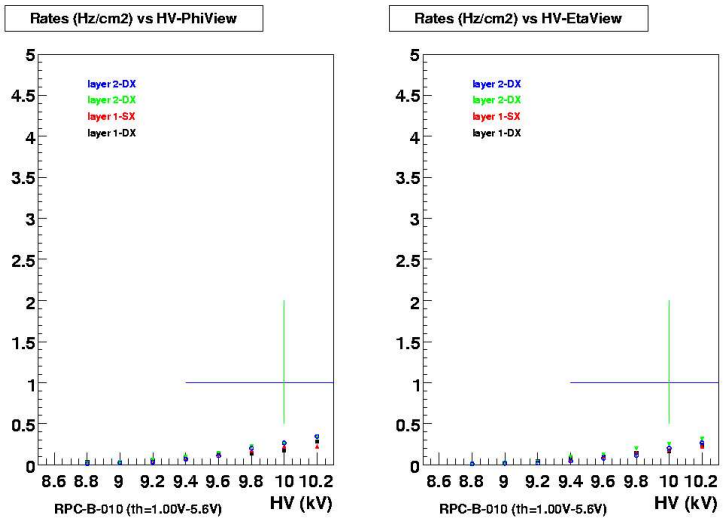


Figure 3.29: $\varphi$ and $\eta$ panel noise rate as a function of the applied High Voltage ($Vth = 1.0\ V$). The cross indicates the acceptance limit for the noise rate ($1\ Hz/cm^2$).

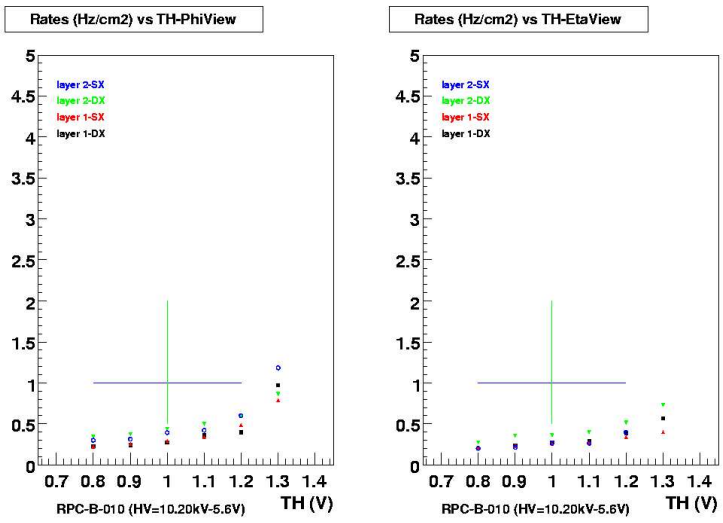


Figure 3.30: $\varphi$ and $\eta$ panel noise rate as a function of the electronics threshold ($HV = 10.2\ kV$). The cross indicates the acceptance limit for the noise rate ($1\ Hz/cm^2$).

tion that the noise is correlated to discharges occurring inside the gas gap. For the gap in figure 3.31, which show the higher counting rate of 0.95 $Hz/cm^2$ and the larger current of 1.2 $\mu A$, the charge delivered in the gas is about 43 $pC$ per count at full efficiency.

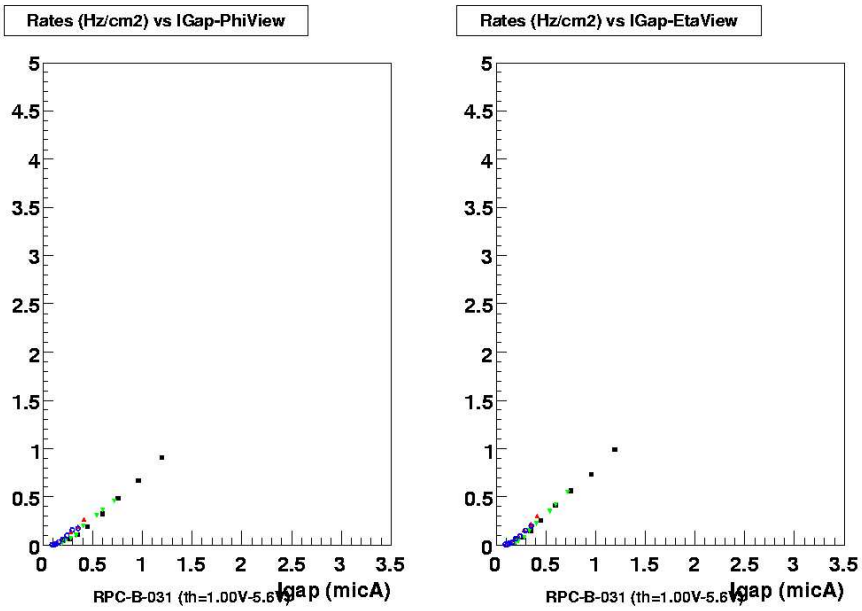


Figure 3.31: $\varphi$ and $\eta$ panel noise rate as a function of the gas gap current (measured during the HV scan with $Vth = 1.0\ V$).

### 3.1.6 BOL RPC quality test results

In this section the results of the *INFN Roma Tor Vergata Laboratory* RPC test stand are summarized.

Of the 192 BOL units tested at Roma test stand, 103 were accepted at the first test. The rejected units were opened, repaired and tested again, before to be shipped to CERN. The rejection reasons are summarized in table 3.2. The frequency of rejecting is also indicated. The main cause of rejection (62 units) was the read-out channel inefficiency. It should be stressed that after the muon station installationthe FE electronics for the ATLAS RPC is equally unaccessible than the detector, because the electronics is located inside the detector Faraday

| Rejection reason | 1st test | 2nd test | 3rd test |
|---|---|---|---|
| Gas leak | 11/192 | 1/89 | - |
| Problem in LV connections | 15/192 | 2/89 | 1/28 |
| High gap current | 22/192 | 9/89 | 5/28 |
| Dead channels exceeding the threshold | 62/192 | 12/89 | 5/28 |
| High noise rate | 6/192 | 3/89 | - |
| Low efficiency | - | 2/89 | - |

Table 3.2: Rejection reasons for the BOL quality test.

cage. On each FE board (8 channels) DC and AC tests were performed before assembling on the read-out panels. However the handling of the panels during the unit assembly caused further damages or disconnections.

In the following figures the data concerning the first 125 BOLs fully analyzed are reported, looking at all corresponding read-out panels.

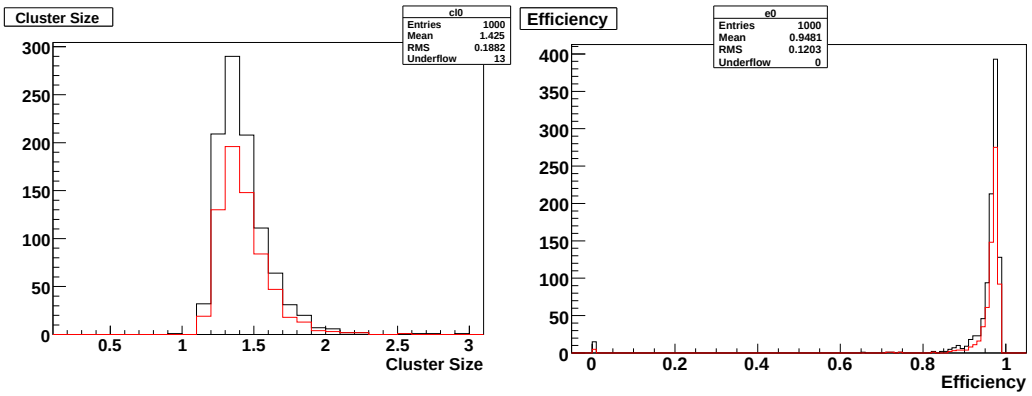


Figure 3.32: Read-out panel average cluster size distribution (left) and efficiency distribution (right). All test results are reported by the black line (125 tests); final acceptance tests, after reparation, are reported by the red line (84 tests). Therefore the distributions shown by the red line are the characteristic ATLAS RPC distributions.

In figure 3.32 the average cluster size and read-out panel efficiency distributions are shown. The distributions in red, which refer to the final results after reparation, can be assumed as the ATLAS RPC references. At the standard working point ($HV = 10.2\ kV$ and $Vth = 1.0\ V$), the average cluster size is 1.4 and the efficiency averaged on all read-out panels is 97%. This result has been obtained after the correction of some systematics due to inefficient DAQ channels

(see section 3.1).

In figure 3.33 the RPC efficiency as a function of the electronics threshold is shown for the $\varphi$ (red points) and $\eta$ (green points) panels respectively. As already observed in section 3.1.4, $\eta$ strips are more affected by the electronics threshold, but there is no difference between the two views for $Vth \geq 1.0\ V$.

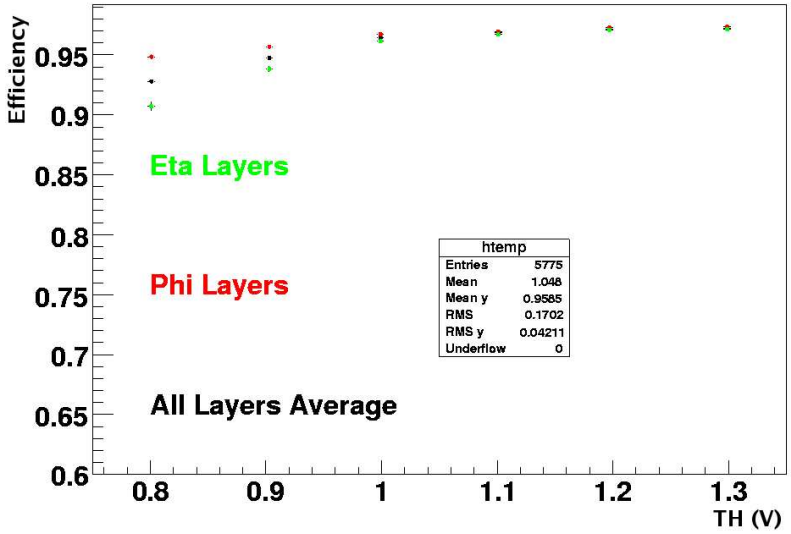


Figure 3.33: Read-out panel efficiency as a function of the FE threshold for $\varphi$ (red) and $\eta$ (green) view ($HV = 10.2\ kV$). The black points are the results by integrating on the two views.

In figure 3.34 the scatter plots of the RPC efficiency and the average cluster size (left) and of the RPC efficiency and the gap current (right) are shown. There is only a very modest correlation between efficiency and cluster size and no correlation between efficiency and Igap. The reason of rejecting units with high gap currents is not related to the detection efficiency but to possible ageing problems [20]. The Igap distribution for the BOL units is shown in figure 3.35, the maximum value measured during the test (after the conditioning phase) is considered for each gas volume. The measured Igap is 0.8 $\mu A$ on average.

The noise detector results are presented. In figure 3.36 on the left the distribution of the noise rate in $Hz/cm^2$ is shown. The measured value at standard working condition ($HV = 10.2\ kV$ and $Vth = 1.0\ V$) is 0.4 $Hz/cm^2$ on average. On the right in figure 3.36 the noise rate dependence on the FE threshold is shown for the $\varphi$ (red points) and $\eta$ (green points) panels. $\varphi$ read-out panels show a larger noise rate at every Vth values.

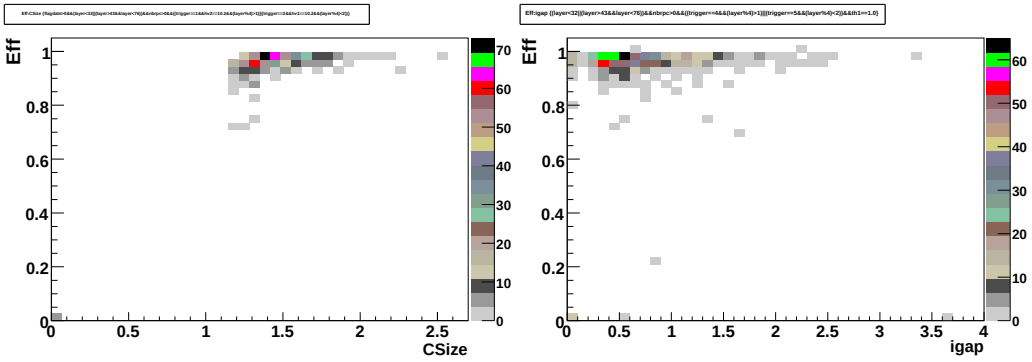


Figure 3.34: Read-out panel efficiency versus the average cluster size (on the left) and gap current (on the right) scatter plots at the standard working point ($HV = 10.2\ kV$ and $Vth = 1.0\ V$). A very modest correlation is observed in the left plot and no correlation is visible in the right plot.

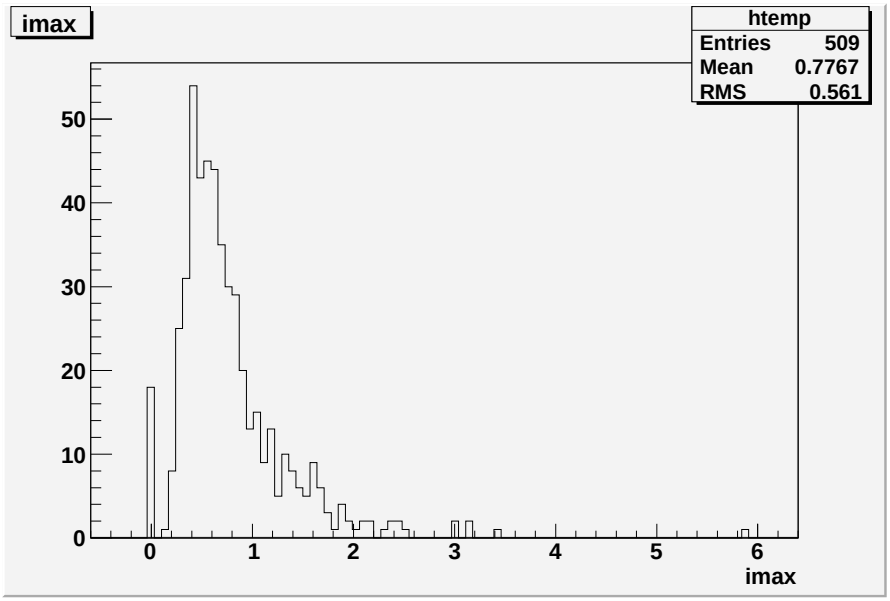


Figure 3.35: Maximum gap current ($\mu A$) distribution.

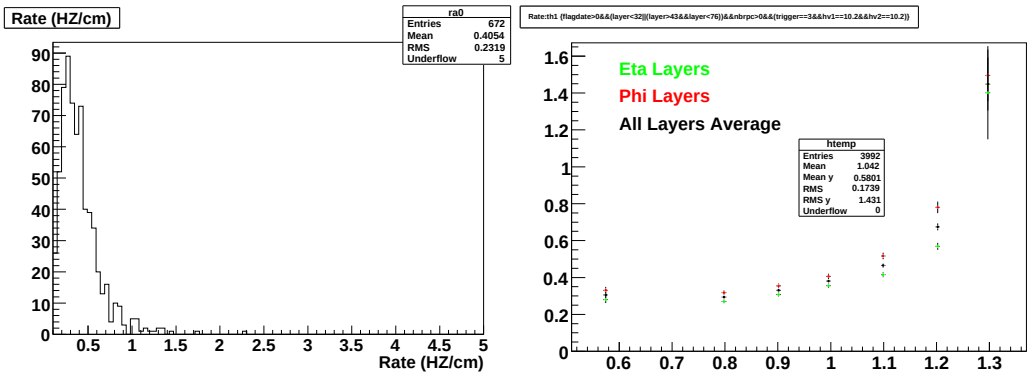


Figure 3.36: Noise rate distribution on the left and noise rate (in $Hz/cm^2$) versus FE electronics threshold (in $V$) on the right.

The correlation between the noise rate and the gap current is shown in figure 3.37.

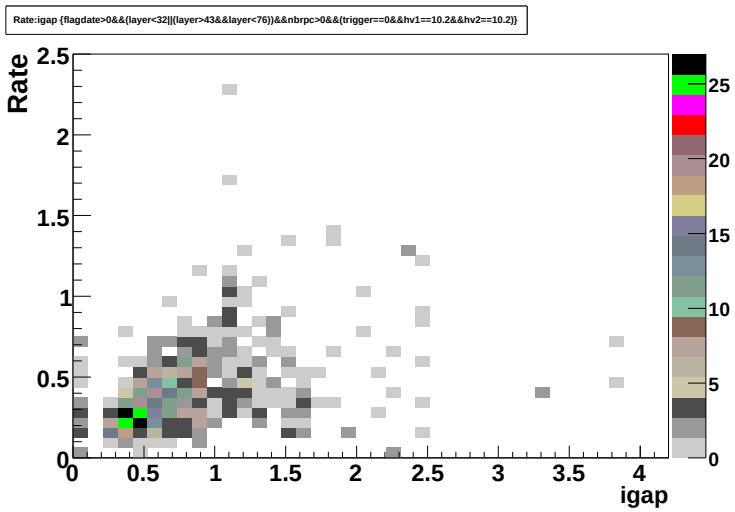


Figure 3.37: The read-out panel noise rate ($Hz/cm^2$) is plotted as a function of the gas gap current ($\mu A$).

The results of the all plots shown in this section indicate that at $HV = 10.2\ kV$ and $Vth = 1.0\ V$, the performance of the BOL chambers can be summarized by the following average values: efficiency $\sim$ 97%, cluster size 1.4, counting rate 0.4 $Hz/cm^2$ and gap current 0.8 $\mu A$.

### 3.1.7 Study of cross-talk between adjacent RPCs

As described in chapter 2, for the ATLAS experiment each RPC unit is constituted of two detector layers rigidly held together in an aluminium box. The two layers of gas gaps, each one with two read-out strip panels for both the $\eta$ and $\varphi$ views, are separated by a panel made of paper honeycomb and sandwiched between two aluminium sheets. This structure should avoid any cross-talk between the two detector layers and the consequent reduction of the trigger rejection power.

A dedicated measurement of the cross-talk between the two RPC layers assembled in the same mechanical structure has been performed at the test stand in order to evaluate the hermeticity of the Faraday cage. For this purpose a set of runs was acquired for 8 BOL units, setting the layers 2 at full efficiency (10.2 $kV$), while no voltage was supplied to the layers 1, although the FE electronics was operative. The trigger condition to select cosmic rays required a four-out-of-four coincidence of the two $\varphi$ layers 2 on the top and two on the bottom. An electronics threshold scan from 0.9 $V$ to 1.4 $V$ was carried out on layers 1, leaving the Vth of layers 2 fixed at the standard value of 1.0 $V$. Runs of $2 \cdot 10^5$ events were collected.

The efficient layers 2 are also used in the analysis for the track reconstruction, according to the algorithm described in section 3.1.4. Each reconstructed track is extrapolated on the layers 1 and a signal in the expected strip or in one of the two closest neighbours (the region where the cross-talk is more probable) is searched. For each event the layer 2 was efficient a possible cross-talk on the layer 1 was searched.

For simplicity a "detection efficiency" is defined for the layers 1. A layer 1 strip is defined "efficient" if a signal of cross-talk occurs. Then the read-out panel "efficiency" is the fraction of events with "efficient" strip over the number of reconstructed track crossing the gas volume.

The panel "efficiency" due to the RPC layer cross-talk as a function of the electronics threshold is shown in figure 3.38. No cross-talk is observable up to threshold of 1.2 $V$, the softest Vth value for the ATLAS configuration. Cross-talk between RPC layers can occur for a softer threshold as 1.4 $V$, but the effect is negligible (below 0.1%). The $\eta$ panels are more affected by the cross-talk, due to their position between the two RPC layers.

Due to the not symmetric assembly of the two RPC layers in a BOL unit, the cross-talk could be different according to the layer position in the unit, so a further Vth scan was acquired inverting the role of layers 1 with the layers 2. No cross-talk of the layers 1 on the layers 2 was observed up to threshold of 1.4 $V$.

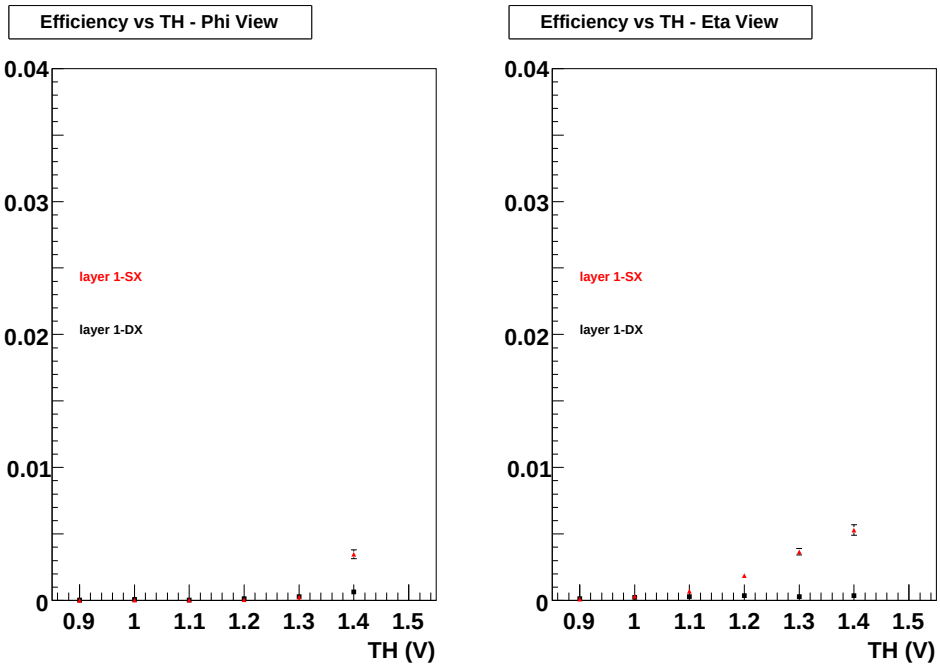


Figure 3.38: Cross-talk due to the adjacent read-out layer for the $\eta$ and $\varphi$ views. The $\eta$ panels are more affected by the cross-talk, due to their position between the two RPC layers.

## 3.2 The H8 Test Beam at CERN

ATLAS RPCs have been also extensively tested (2003-2004) with muon beams at H8 beam line at CERN. H8 is a secondary beam obtained by the interaction of the SPS proton beam with a proper target. The pions produced in the interaction, selected according to the momentum, decay in muons, that are filtered with proper iron absorber. The muon beam obtained in this way has energy ranging from 20 to 350 $GeV$.

The purpose of this test was to study a full ATLAS muon tower of the "Large" barrel sectors consisting of: the Inner, the Middle and the Outer stations, ordered in the beam direction. The stations consist of tracking (MDT) and trigger (RPC) chambers. The MDT is sandwiched between two RPC chambers in the Barrel Middle stations (BML) and coupled to a single RPC located downstream in the Barrel Outer stations (BOL), as in figure 3.39. No trigger chamber is foreseen for the inner stations (BIL).

Within a muon tower the RPC chambers are identified, according to the LVL-1 trigger logic scheme (see chapter 4). The BML RPC chamber, mounted behind the MDT chamber respect to the beam direction, is called "BML Pivot". The other BML RPC is called "BML Low Pt" . Moreover the BOL is called "BOL High Pt".

The test was dedicated to study, in addition to the behaviour of the single chamber, more general muon system aspects like trigger/tracking capabilities and alignment.

The beam trigger was provided by two scintillator systems. The coincidence of the signals of two scintillators ($10 \times 10\ cm^2$) centred on the beam line provided the small area trigger. A large area trigger ($60 \times 100\ cm^2$) was produced by the coincidence of two planes of six scintillating slabs. For the hodoscope setting a veto to suppress the beam core was possible, by using the $10 \times 10$ trigger.

### 3.2.1 RPC cluster size study at H8 site

One of the most important achievement of the RPC test was the systematic study of the cluster size dependence on the muon impact point in the strip panel. This was possible thanks to the MDT chambers which provided an accurate reconstruction of the muon tracks.

Tracks were reconstructed by the MDTs in the $\eta$ view and extrapolated on the RPC gas gaps. The dependence of the size of the RPC cluster on the muon track position was measured. In this test the RPCs were operated at $HV = 9.6\ kV$ and

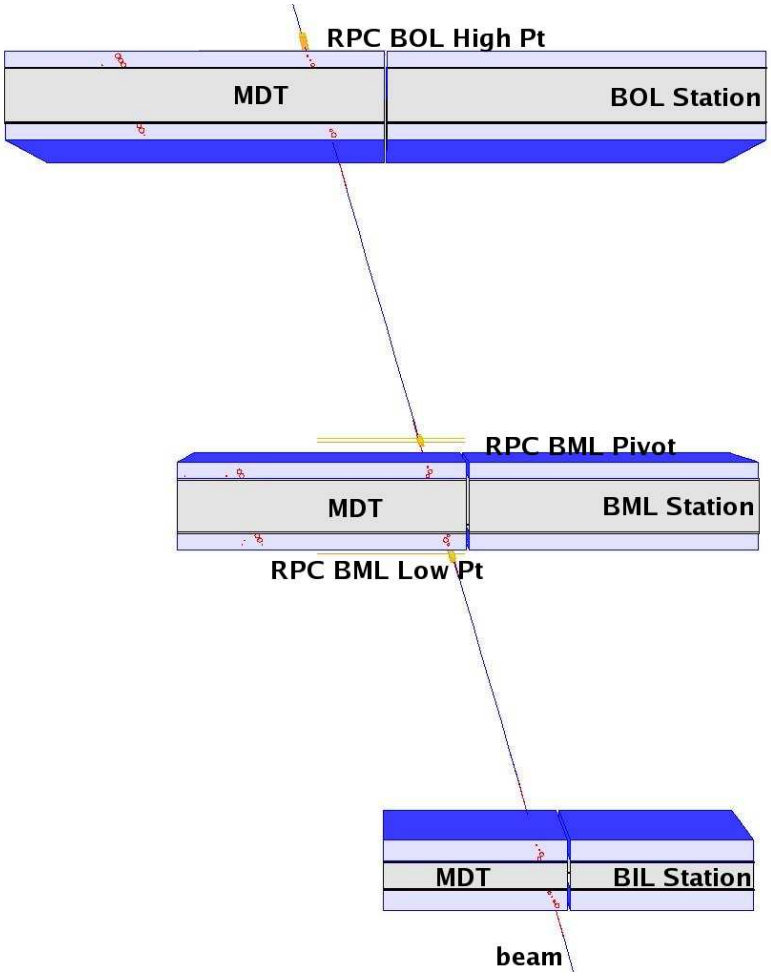


Figure 3.39: Scheme of the two muon towers installed at H8 site (view from the top). The beam crosses first the BIL station. The chambers were rotated of about 30 degrees respect to the beam, in such a way to simulate inclined muon tracks at $\eta > 0$.

$Vth = 0.9\ V$.

In figure 3.40 on the left the probability of clusters with size 1 is shown as a function of the $\eta$ coordinate expected by the MDT track extrapolation. The probability is flat and about 1 for a muon crossing the gas gap in the region close to the centre of a strip and it decreases down to 20% for tracks extrapolated between two adjacent strips. Therefore the distribution in figure 3.40 on the left exactly reproduces the RPC strip pitch (34 *mm*).

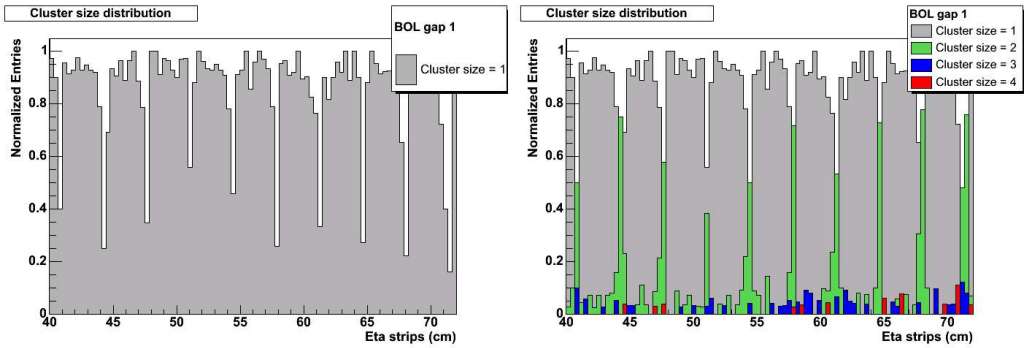


Figure 3.40: Cluster size probability as a function of the muon impact point extrapolated by the MDT track. On the left only clusters with size 1 are considered. The RPC strip pitch (34 *mm*) is exactly reproduced. All clusters are on the right, using the colors to distinguish clusters of different size.

On the right side of figure 3.40, the probabilities of RPC cluster size 1, 2, 3 and 4 are shown (with different colors) as a function of the muon impact point on the panel strip. The systematic of cluster sizes 1 (85.2%) and 2 (11.7%) can be perfectly explained by the charge induction on the strip plane: when the gas discharge occurs near the centre of a strip most of the induced charge is concentrated on that strip; when it occurs at the centre of two strips, the induced charge is equally shared between these two strips. The systematics of the cluster sizes 3 (2.5%) and 4 (0.6%) are less straightforward. They might be related to the appearance of $\delta$-rays produced in the gas. Although some systematics with respect to the muon impact point is still visible.

Averaging on all the readout channels (figure 3.41), cluster with size 1 and 2 are shown with respect of the strip width. The distributions are symmetrical with respect to the strip centre.

Cluster size is very sensitive to the RPC working point. In figure 3.42 the probability distributions of cluster with size 1 (up) and of cluster with size 2 (down)

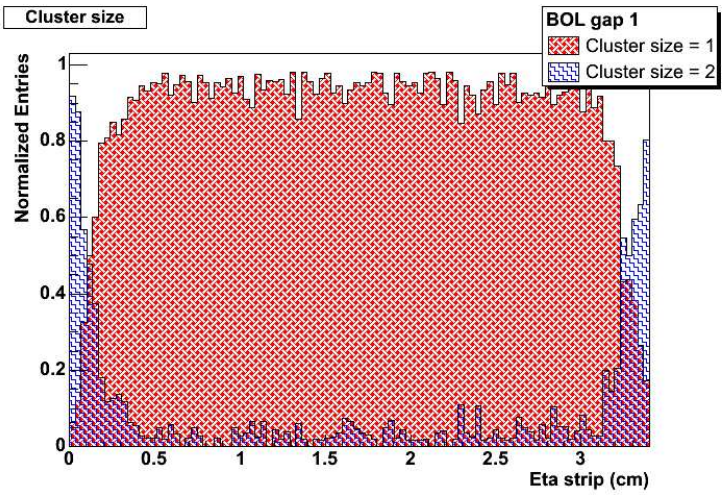


Figure 3.41: Cluster size 1 in red and 2 in blue, averaging on all the readout channels. The strip pitch is clearly reproduced.

| | BOL gap 1 | | BOL gap 2 | |
|---|---|---|---|---|
| High Voltage | Cluster size 2 | $\sigma$(mm) | Cluster size 2 | $\sigma$(mm) |
| 9.4 $kV$ | 6.1% | 0.93 ± 0.16 | 5.5% | 1.14 ± 0.17 |
| 9.6 $kV$ | 10.0% | 1.22 ± 0.06 | 9.1% | 1.29 ± 0.08 |
| 9.8 $kV$ | 14.2% | 1.91 ± 0.07 | 12.4% | 1.63 ± 0.08 |

Table 3.3: Cluster size 2 for different HV values: percentage and $\sigma$ estimated by Gaussian fit on the cluster size 2 distribution.

are shown for three different values of the HV applied to the gas volume. The probability of cluster size 2 increases for increasing HV.

The muon position distribution for clusters with size 2 in the region between two adjacent strips is shown in figure 3.43. Assuming that the distribution is Gaussian, a fit is performed. The $\sigma$ is an estimate of the spatial resolution of RPCs when clusters with size 2 occur. The percentage of events with cluster size 2 and the $\sigma$ for the distribution related to two gaps of the BOL station are presented in table 3.3 for different HV values. The $\sigma$ increases with the percentage of clusters with size 2.

These $\sigma$ values of the cluster size 2 should be compared with those of cluster size 1, which in the rectangular approximation is $L/\sqrt{12} = 9.8\ mm$ ($L$ is the strip pitch). This is an upper limit because the experimental distribution (figure 3.41)

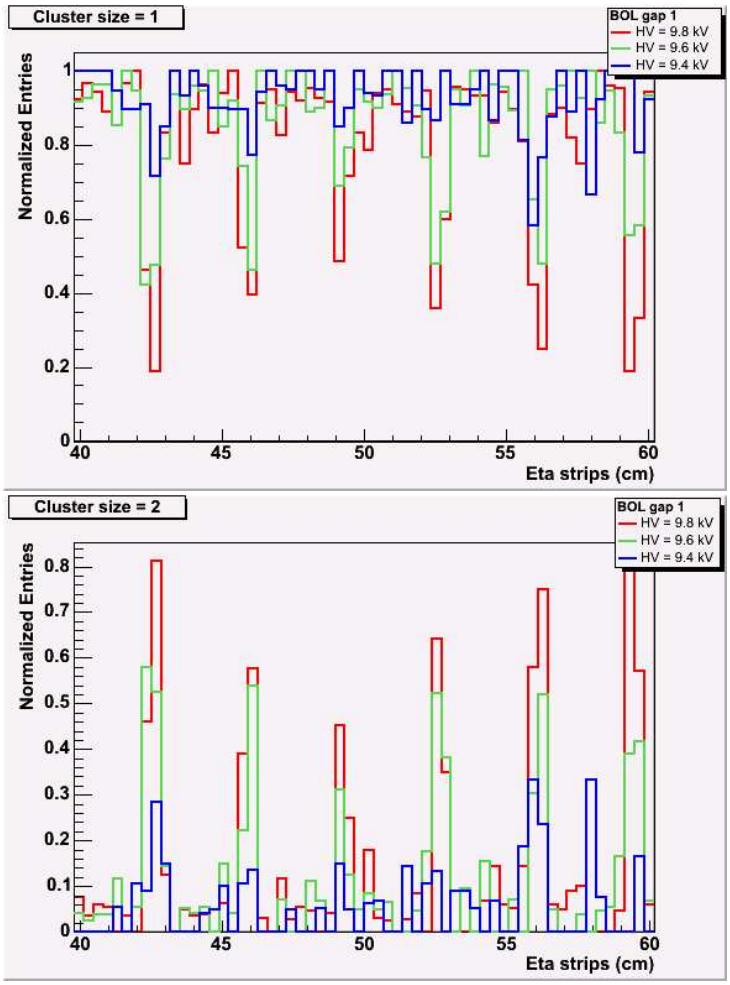


Figure 3.42: Probability distributions of cluster size 1 (up) and cluster size 2 (down) as a function of the muon impact point extrapolated by the MDT track for different values of the applied high voltage.

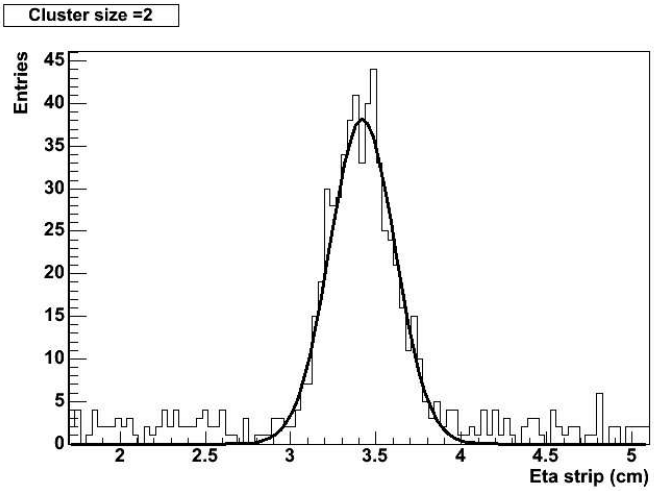


Figure 3.43: Distribution of clusters with size 2 in the region between two adjacent strips ($HV = 9.6\ kV$ and $Vth = 0.9\ V$). A Gaussian fit is performed.

is somewhat narrower. Therefore the combination of cluster sizes 1 and 2 gives better position information with respect to an "ideal RPC" giving a fixed cluster size equal to 1.

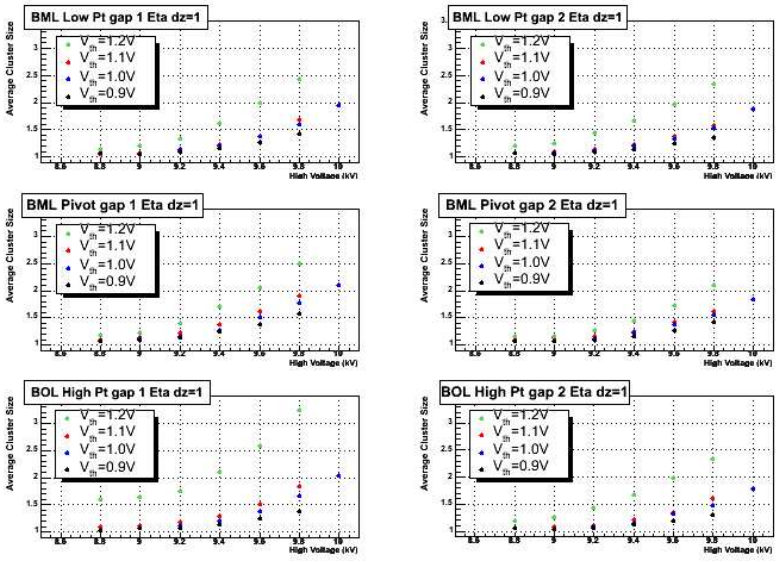


Figure 3.44: Average cluster size as a function of the high voltage for different electronics threshold values. The results of each gap of a muon tower are shown.

The cluster size is also affected by the FE electronics threshold. HV scans

were collected at H8 site, varying the Vth setting (MDTs were switched off). The average cluster sizes measured for the gaps of a muon tower tested at H8 site are shown in figure 3.44 as a function of the high voltage. Different Vth values are considered. The average cluster size increases with the HV and is stable up to electronics threshold of 1.2 $V$.

As a conclusion, the cluster size is not a random, but a systematic effect depending on the impact point of the muons on the strip panel. It affects the RPC spatial resolution, that, in the limit of HV and Vth ranges tested here, is improved for increasing cluster size.

## 3.3 Conclusions

The largest RPCs, the BOL units, were tested in the *INFN Roma Tor Vergata Laboratory* from May 2005 until July 2006. Of the 192 BOL units tested, 103 were accepted at the first test. The rejected units were opened, repaired and tested again, before to be shipped to CERN. The main cause of rejection (62 units) was the read-out channel inefficiency; the other causes were high gap currents (22), problems in LV connections (15), gas leaks (11) and high noise rates (6).

The results of the all accepted units indicate that at $HV = 10.2\ kV$ and $Vth = 1.0\ V$, the performance of the BOL chambers can be summarized by the following average values: efficiency $\sim 97\%$, cluster size 1.4, counting rate 0.4 $Hz/cm^2$ and gap current 0.8 $\mu A$.

A linear correlation between single counting rate and gap current is observable in both $\eta$ and $\varphi$ views. This observation supports the interpretation that for a perfectly optimized detector Faraday cage the noise is mainly correlated to discharges occurring inside the gas.

No correlation was observed instead between the gap current and the detection efficiency. The reason of rejecting units with high gap currents ($> 3\ \mu A$) is not related to the efficiency but to possible ageing problems.

Dedicated measurements at the cosmic test stand show that no cross-talk occurs between the two RPC layers assembled in the same mechanical structure up to electronics threshold of 1.2 $V$ (the softest Vth value for the ATLAS configuration). A negligible cross-talk (below 0.1%) was measured for a softer threshold. These measurements ensure the hermeticity of the Faraday cage, without which the trigger rejection power would be spoiled.

Moreover tests with muon and pion beams was carried out at the CERN H8

site, where a complete ATLAS-like muon sector with six RPC units and three MDT chambers was assembled in the test area. The dependence of the size of the RPC clusters on the position of the muon track reconstructed by the MDT chambers was studied. Cluster with size 1 occurs in 85% of events ($HV = 9.6\ kV$ and $Vth = 0.9\ V$), and in particular they are more frequent for tracks extrapolated near the centre of a strip; otherwise tracks impacting in the region between two adjacent strips produce events (12%) with cluster size 2. In a small number of cases (3%), clusters with sizes > 2 are also observed.

The cluster size is very sensitive to the RPC working point: increasing the HV and the Vth (i.e. decreasing the physical threshold), a decrease of clusters with size 1 and an increase of cluster size 2 frequency are observed.

# Chapter 4

# The LVL-1 muon trigger logic

The First Level (LVL-1) muon trigger is crucial in the ATLAS experiment for the on-line selection of the events with high transverse momentum muons and for their correct association to the bunch-crossing of interest. The basic principle of the LVL-1 algorithm is the selection of the events with muons having a large $p_T$ coming from the interaction vertex.

A general description of the Trigger System and of the Muon Spectrometer of the ATLAS experiment has been already given in chapter 1. As specialized muon trigger detectors, RPCs are used in the barrel ($|\eta| < 1.05$) and TGCs in the end-cap.

The ATLAS barrel is divided in two half-barrels, symmetric respect to $\eta = 0$, and azimuthally segmented in octants; each octant is further subdivided in two parts, referred as Large and Small sectors.

The muon chambers in the barrel are arranged on three stations: the Inner, the Middle and the Outer. Each station is constituted by a precision tracker chamber (the MDT chamber); moreover in the middle station two RPCs (RPC 1 and RPC 2) cover the internal and external faces of the MDT chamber, and in the outer station a third RPC (RPC 3) is assembled with the outer MDT chamber, covering its external or internal face according to the ATLAS sector dimension as shown in figure 4.1.

RPC chambers are classified, according to their location, into BML (Large sectors of RPC 1 and RPC 2), BMS (Small sectors of RPC 1 and RPC 2), BOL (Large sectors of RPC 3) and BOS (Small sectors of RPC 3). A RPC plane is composed of four doublets of gas volumes, each one read out by metallic strips in the two orthogonal views, $\eta$ and $\varphi$, referred as bending and non-bending projections respectively.

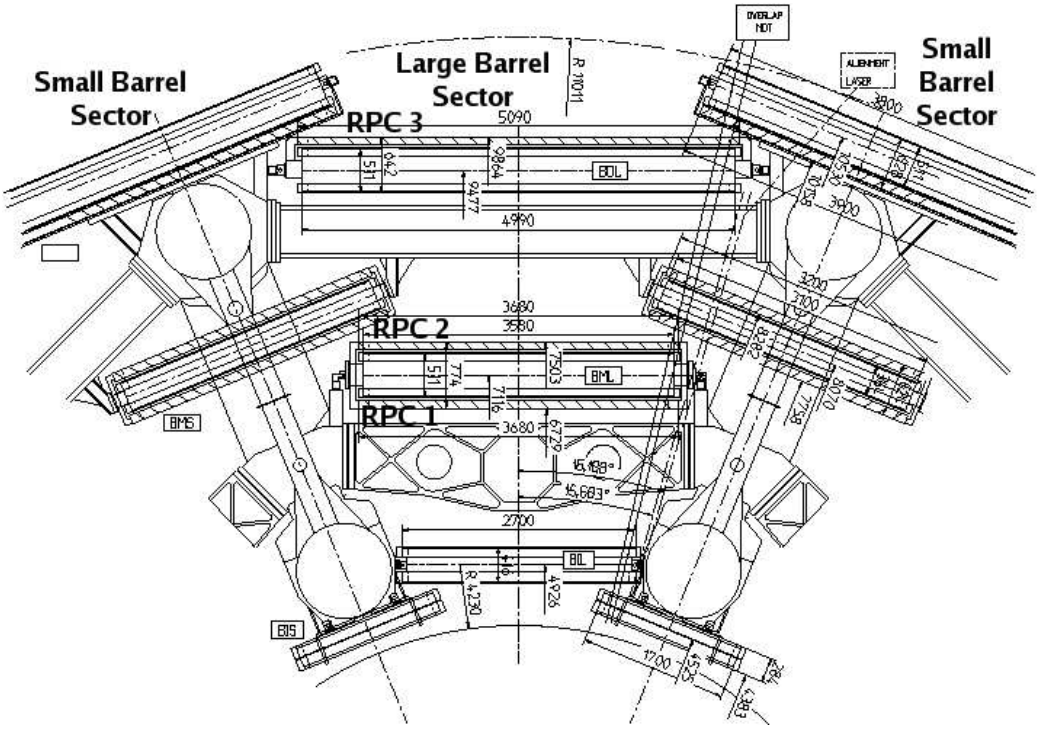


Figure 4.1: View of a standard barrel sector ($\varphi$ view). The three muon stations are visible: the inner station is constituted by a MDT chamber; the middle station is composed of two RPCs (RPC 1 and RPC 2) covering the internal and external faces of a MDT chamber, and in the outer station a third RPC (RPC 3) is assembled with a MDT chamber, covering its external (Large Barrel Sector) or internal (Small Barrel Sector) face, according to the ATLAS sector dimension.

The muon trigger logic [10] is based on coincidences between different planes, the RPC 2 being chosen as "pivot". The two innermost planes are used to trigger low-$p_T$ muons (mainly for b-physics studies), while the outermost is used to trigger high-$p_T$ muons. To reduce the rate of accidental triggers, due to low-energy background particles in the ATLAS cavern, the algorithm is performed in both the $\eta$ and $\varphi$ projections for both low-$p_T$ and high-$p_T$ triggers. A valid trigger is generated only if the trigger conditions are satisfied for both projections.

The trigger logic is implemented through Coincidence Matrices (CM). They are connected to RPC strips and perform space coincidences in a fixed time window. The trigger response is given evaluating the so called Coincidence Windows, as schematically shown in figure 4.2. CMs provides also the read-out of the RPCs.

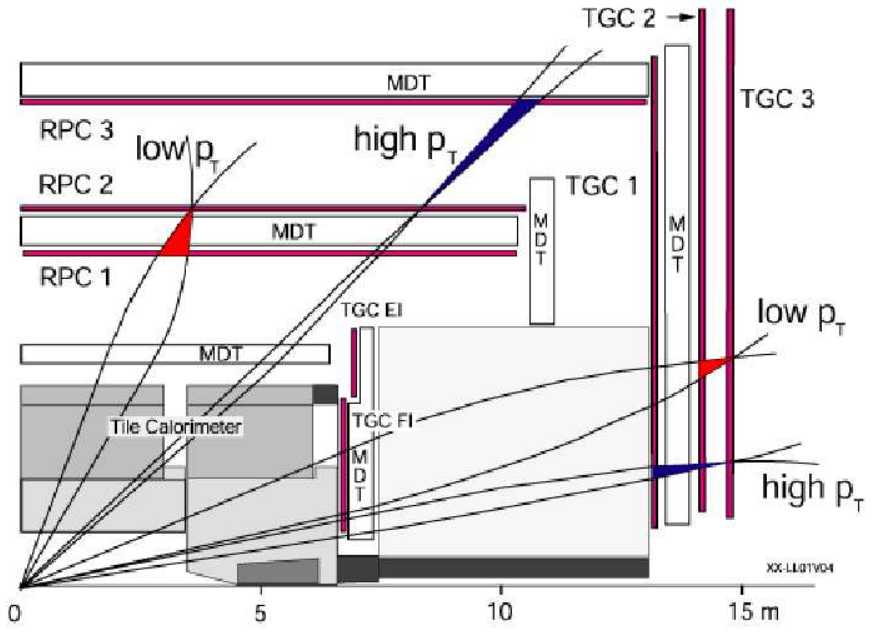


Figure 4.2: Schematic view of the the coincidence-window-based muon LVL-1 trigger algorithm ($\eta$ view). In the trigger logic the middle plane (RPC 2) is chosen as "pivot".

Four CMs, two in $\eta$ and two in $\varphi$, form a Pad. The intersection of a $\eta$-CM and a $\varphi$-CM within a Pad gives a RoI (Region Of Interest) of size $\Delta\eta \times \Delta\varphi \simeq 0.1 \times 0.1$. In order to select also muons with inclined tracks, RPC signals from the confirm

planes (RPC 1 and RPC 3) can be split in more than one CM. For this purpose splitter boxes are mounted on the trigger detectors.

The low-$p_T$ trigger algorithm operates in the following way: if a track hit is generated in the RPC 2 doublet (the pivot plane), a search for the same track is made in the RPC 1 doublet, within a road whose centre is defined by assuming the muon path to be a straight line (i.e. the infinite momentum approximation) with the origin at the interaction point. A scheme of the trigger logic in the bending plane is shown in figure 4.3.

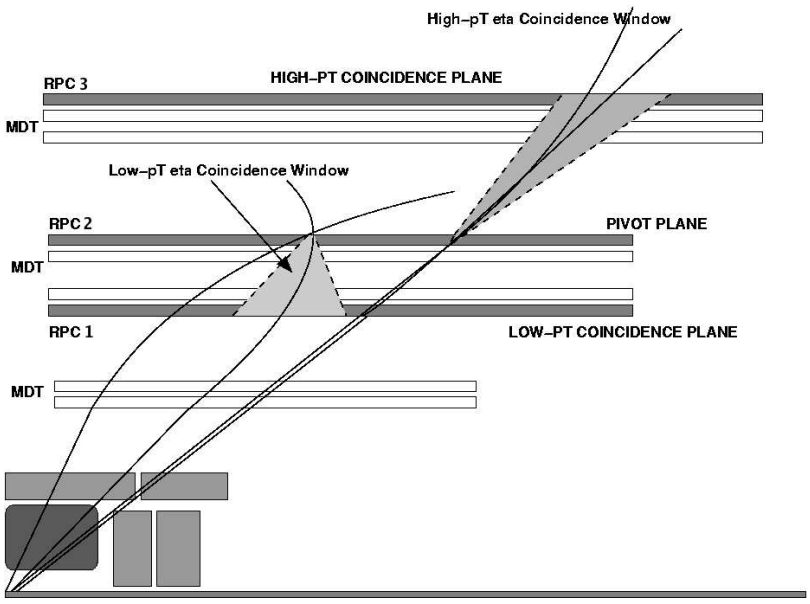


Figure 4.3: Scheme of the trigger algorithm in the bending plane: when a muon crosses the pivot plane (RPC 2), the low-$p_T$ algorithm activates the trigger if it finds a hit of the same track in the RPC 1 doublet, within a road whose centre is defined by assuming the muon path to be a straight line with the origin at the interaction point. The high-$p_T$ algorithm combines the result of the low-$p_T$ trigger with the information generated in the RPC 3 plane, operating in a similar way of the low-$p_T$ algorithm.

The width of the road is a function of the desired cut on the muon transverse momentum: the smaller the road width, the higher the cut on $p_T$. The system is designed so that three programmable $p_T$ thresholds in each projection can be applied simultaneously.

According to the trigger road, the coincidence windows for each $p_T$ threshold are defined. They are not symmetric around the extrapolated point of the infinite

momentum path: muons bending towards high $|z|$ regions cross the RPC 1 plane at a distance from the extrapolated point larger than that for muons of opposite charge. That leads to asymmetric coincidence windows, formed by independent left and right half-windows. This effect increases with $|\eta|$ in the barrel: the difference between the right and left half-window is $7/10$ *cm* in the large/small chambers at $|\eta| \sim 0.9$.

The low-$p_T$ trigger condition is satisfied if, for both projections, there is at least one hit within the coincidence window, and at least one of the two low-$p_T$ doublets (RPC 1 and RPC 2) has hits in both trigger layers satisfying the three-out-of-four (3/4) logic.

The high-$p_T$ algorithm makes use of the result of the low-$p_T$ trigger and of the information generated in the RPC 3 outer station. It operates in a similar way of the low-$p_T$ algorithm with three programmable $p_T$ thresholds, which can be applied simultaneously. The high-$p_T$ trigger is satisfied if the track passes the low-$p_T$ criteria, and in the barrel at least one hit in the two trigger layers of RPC 3 are in coincidence.

In total the thresholds programmable simultaneously are six: three for low-$p_T$ trigger and three for high-$p_T$ trigger. The lower momentum limit for detecting a muon in the Muon System is set by the energy loss in the calorimeter and corresponds to $p_T \sim 3$ *GeV* in the barrel. The standard CM threshold configurations for the ATLAS experiment are summarized in table 4.1.

| Trigger | $p_T$ Threshold |
|---|---|
| Low-$p_T$ trigger | 6 *GeV* |
| | 8 *GeV* |
| | 10 *GeV* |
| High-$p_T$ trigger | 20 *GeV* |
| | 40 *GeV* |

Table 4.1: Standard Coincidence Matrix threshold configurations for the ATLAS experiment.

The trigger roads, which determine the $p_T$ thresholds for the proposed trigger system, have been computed by tracking single muons through the ATLAS detector, using Monte Carlo simulation techniques. The size of a coincidence window is defined such that muons of each charge within the detector acceptance, generated with transverse momentum equal to the $p_T$ threshold, are accepted [24]. Each half-

window is evaluated accounting for the relative trigger efficiency of positive and negative muons independently, to minimize possible effects on charge-asymmetry measurements.

The trigger efficiencies as a function of the muons $p_T$ for the low-$p_T$ and the high-$p_T$ system for the standard $p_T$ thresholds are shown in figure 4.4. The trigger efficiency is estimated by the muon LVL-1 trigger logic simulation with a large sample ($10^6$) of single muons simulated over a wide $p_T$ range (3-50 $GeV$) [26]. The plateau value in figure 4.4 corresponds to the system geometrical acceptance, limited by the zone not covered by the RPCs (magnet ribs and support structure, elevator hole and central crack). The overall acceptance is 82% for low-$p_T$ trigger and 78% for high-$p_T$ trigger.

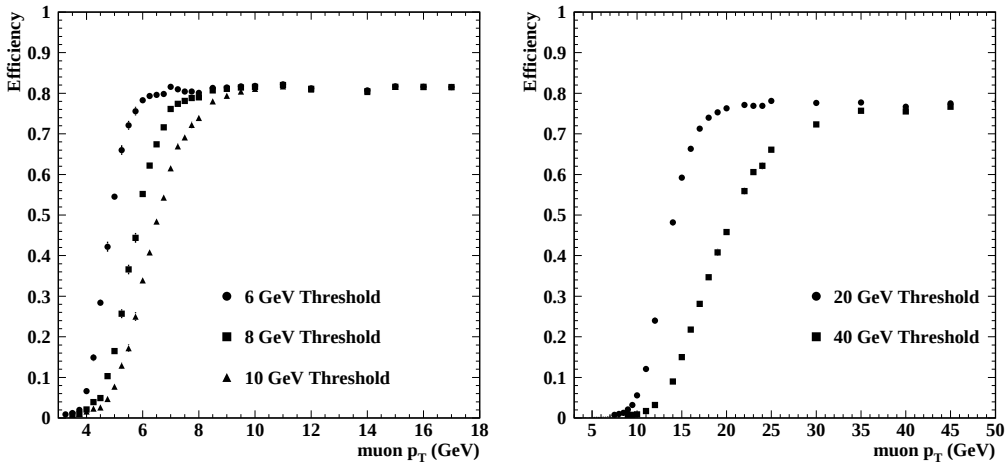


Figure 4.4: Level-1 Muon Trigger Efficiency curves for low-$p_T$ (on the left) and high-$p_T$ (on the right) system.

### The LVL-1 muon trigger components

The figure 4.5 shows a scheme of the trigger slice layout [10] . Both the devices mounted on the trigger detectors and the off-detector devices sited in the counting room are shown.

The most crucial component of the trigger system is the Coincidence Matrix ASIC (CMA) chips [25]. It performs almost all the relevant trigger functionalities, as coincidence and majority operations, thresholds cuts, pipelined delays and hit

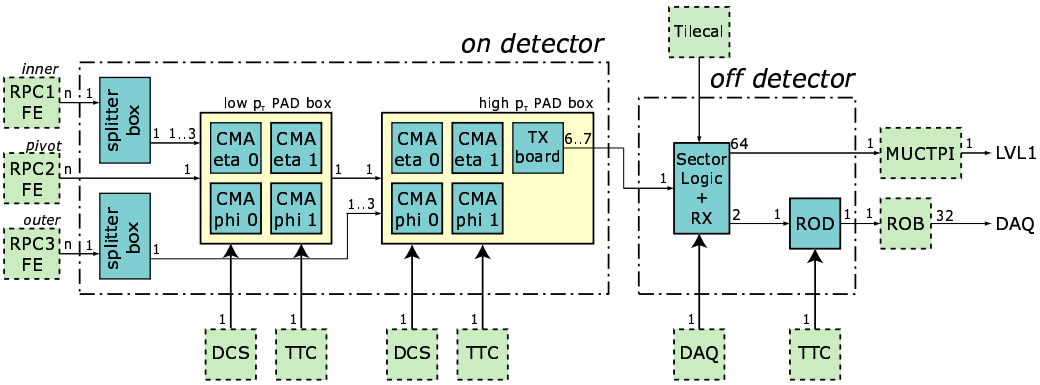


Figure 4.5: Trigger slice layout, showing different on- and off-detector devices.

clustering. ASIC operates with the LHC machine 40 *MHz* clock, and its internal logic works at 320 *MHz*. Inputs from the RPCs are called: $I0$ and $I1$, 32 strips each one, coming from the RPC 2 pivot plane for the low-$p_T$ trigger or from the low-$p_T$ trigger pattern output for the high-$p_T$ trigger; $J0$ and $J1$, 64 strip each one, coming from RPC 1 or RPC 3.

The system is designed so that 3 $p_T$ thresholds in each projection can be performed in parallel. The coincidence matrix contains thus $3 \times 32 \times 64$ cells. The trigger output of the coincidence blocks is a hit pattern containing:

- hits which generated the valid trigger,
- the highest threshold value,
- two bits indicating overlap conditions (to reduce the fake double-muon trigger rate due to a single track crossing two overlapping trigger chambers),
- the three lower bits of the Bunch Crossing counter.

The information of two adjacent CMA boards in the $\eta$ projection, and the corresponding information of the two CMA boards in the $\varphi$ projection, are combined together in the low-$p_T$ Pad Logic board. The four low-$p_T$ CM boards and the corresponding Pad board are mounted on top of the RPC 2.

The low-$p_T$ Pad board generates the low-$p_T$ trigger result and the associated RoI information. This information is transferred, synchronously at 40 *MHz*, to the corresponding high-$p_T$ Pad board, mounted on the outer RPC, that collects the overall result for low- and high-$p_T$ trigger.

The high-$p_T$ trigger logic receives as an input the hits on the outer RPC plane and the output pattern of the low-$p_T$ trigger algorithm. The high-$p_T$ Pad board, mounted on top of the RPC 3 detector, combines the low- and high-$p_T$ trigger results. Then the combined information is sent, synchronously at 40 $MHz$, via optical links, to a Sector Logic (SL) board, located in the counting room. Data coming from up to eight high-$p_T$ Pad belonging to the same ATLAS trigger sector are collected by the same SL board.

Each Sector Logic board selects two candidate muons those with the highest thresholds and associates a Region of Interest and a unique bunch crossing number to each one.

The trigger data elaborated by the Sector Logic is sent, again synchronously at 40 $MHz$, to the Muon Interface to the Central Trigger Processor (MUCTPI), located in the same counting room.

The MUCTPI elaborates the data from the Sector Logic boards, counts the number of muon candidates for each of the six $p_T$ thresholds and passes the multiplicity information on to the Central Trigger Processor (CTP). The MUCTPI is also responsible for detecting cases where muons traverse more than one sector due to chamber overlaps, making sure that they are counted only once in the multiplicity calculation. Overlaps within sectors are handled by the logic specific to the barrel and end-cap subsystems.

The ATLAS LVL-1 Central Trigger Processor (CTP) combines information from the LVL-1 calorimeter and muon trigger processors, as well as from other sources such as calibration triggers, and makes the final LVL-1 accept decision. The algorithm used by the CTP to combine the different inputs allows events to be selected on the basis of trigger menus.

In parallel, data provided by CMs are read out from both the low- and high-$p_T$ Pad boards. These data include the RPC strip pattern and some additional information used in the LVL-2 trigger. The read-out data for events accepted by the LVL-1 trigger are sent asynchronously to Read-Out Drivers (RODs) located in the counting room and from here to the Read-Out Buffers (ROBs). The data links for the read-out data are independent of the ones used to transfer partial trigger results to the SL boards.

# Chapter 5

# Simulation of the LVL-1 muon trigger with cosmic muons

Before the starting of the ATLAS experiment, a phase of detector commissioning is foreseen. This phase is very important, because it is the first time that the whole ATLAS detector works in the ATLAS cavern, with all the subdetectors assembled together in the final layout. A set of data will be acquired to test every subdetectors and check their working points; moreover the data will be essential to test the calibration and the alignment of each subdetector.

During the first period (2006-2007), the collisions will not be available and cosmic rays will be exploited as particle sources for the commissioning test. The RPCs, the trigger chambers in the ATLAS barrel, will be used to select the cosmic ray data, although the trigger system layout is optimized for muons coming from $p$-$p$ collisions and it is not congenial for cosmic muons. Any modification of the detector geometry or the cable connections is not possible after the assembly in the cavern, so a stringent limit to the trigger logic is imposed by the detector hardware. However a special LVL-1 configuration can be applied in order to optimize the cosmic ray selection, in fact the trigger acceptance is modifiable by programming the Coincidence Matrices (CMs) with a set of appropriate thresholds relative to the desired trigger.

A dedicated simulation of the detector performance with cosmic rays has been performed. The trigger rates expected for some different LVL-1 configurations have been estimated, in order to evaluate the most useful trigger logic for the cosmic ray acquisition. A first test of three muon towers in the ATLAS cavern made possible a comparison of the simulation results with the data collected in the cavern. The results of this study are here presented.

## 5.1 Detector simulation

The new ATLAS detector simulation exploits the *Geant4 Toolkit* [22], which is based on an object oriented architecture, implemented using C++. The *Geant4 kernel*, which is the core component of the toolkit, is able to manage the run, generating particles for each event to be simulated and taking care of all the operations needed for particle propagation in the simulated detector.

The user is requested to provide the kernel with a geometrical description of the volumes in which the particles will be propagated, together with an accurate description of the materials, each volume is made of. A list of the physical processes to be simulated for each kind of particles is also necessary. Finally, the kernel needs to know a mechanism to generate the primary vertices of the events to be simulated.

Hit production in Geant4 is provided by "*Sensitive Detectors*". If a certain volume described in the geometry is supposed to generate signals when crossed by some kind of particle, it must be associated to a properly implemented Sensitive Detector, which is an instance of a class different from the one describing the "real" geometry. When a simulated particle trajectory crosses a volume which can generate hits, the kernel calls the corresponding Sensitive Detector implementing the hit generation algorithms. Hence, the Sensitive Detector generates a list of hits, which are stored for further processing. The `RPCSensitiveDetector` class has been implemented to provide the generation mechanism of the hits in the barrel trigger chambers.

The Muon Digitization software package is independent of the Geant4 detector simulation, and runs within the ATHENA framework [23], which is a control framework dedicated to the ATLAS analysis and based on the GAUDI architecture. The goal of the muon digitization is to simulate the output signal of the ATLAS muon detector, obtained by the output of the Geant4 detector simulation. The digitization process consists of two steps: in first, the output of the detector simulation (Geant4 hits) is converted to muon digits; in second step, the muon digits are converted to Raw Data Objects (RDO) from which the byte stream (the electronics output) is produced.

### 5.1.1 RPC digitization

The RPC hits are generated by the RPC SensitiveDetector, which assigns to them a Simulation Identifier (SimID), uniquely identifying the gas gap each hit is reg-

istered in. The hit position in the gas gap reference system is also stored, together with the time from the beginning of the event, i.e. the time of flight of the particle generating the hit.

The digitization process takes care of adding to the hits the information necessary for further analysis as trigger algorithm simulation and track reconstruction. It translates any SimID to a Standard Offline Identifier (OID), which is used by the other ATHENA algorithms to uniquely identify the RPC strips in the Muon Spectrometer. Using the position information provided by the hits, the digitization can properly calculates the propagation time of each electronics signal along the strip and adds it to the hit time of flight; finally it assigns this *global time* to the digit.

In reality, when a particle crosses a RPC and generates an avalanche in the gas gap, a significant signal can be induced (and detected) in more than one read-out strip. A set of $n$ adjacent strips induced by the same signals forms a *cluster* of size $n$. As described in section 3.2.1, the particle impact point along a strip is known to influence the size of the cluster, the signal will generate. Particle crossing the gap in the region close to the centre of a strip will probably generate cluster of 1 strip; otherwise if the track impacts the gas volume in the region centred between two adjacent strips, a cluster with size 2 occurs. The cluster size averaging on the all detector surfaces is typically of 1.5, but it strictly depends on the RPC working point (high voltage and electronics threshold).

The hit production mechanism provided by the ATLAS Geant4 simulation does not include a tool for proper simulation of clusters. A particle generates an only hit on one strip, except when secondaries (for example $\delta$-rays) are produced and detected by the neighboring strips.

In order to consider the phenomenon of the RPC clusters, RPC digitization algorithm reproduces the observed cluster sizes by generating, when necessary, digits on strips adjacent to the one actually crossed by the particle. Cluster simulation is carried on in three steps:

1. experimental distributions (for the fixed RPC working point) are used to evaluate, according to the particle impact point along the strip, the probability to have cluster size 1 or 2;

2. experimental distributions are used to decide what the final size of the simulated cluster will be;

3. digits are created according to the results of the above steps.

### 5.1.2 LVL-1 trigger logic simulation

In order to optimize the LVL-1 trigger logic design and to study its performances a dedicated C++ package [27] has been developed, running within the ATHENA framework.

All the logic of the trigger system hardware is duplicated in the simulation. The coincidences are performed using the appropriate granularity of the trigger matrices. Moreover the LVL-1 package (as the Coincidence Matrices do) allows to program the six $p_T$ thresholds (three for the low-$p_T$ trigger and three for the high-$p_T$ trigger) loading the CM configuration files.

It has to be stressed that coincidences selected by simulation are only spatial coincidences, because no timing information is currently included in the detector simulation: the RPC signals produced by the same cosmic muon are forced to reach the CMs simultaneously. This forcing does not impact significantly the trigger performance, since the muon time of flight within an ATLAS muon trigger tower is in the coincidence time window.

## 5.2 Cosmic ray simulation in the ATLAS cavern

In the lower half of the atmosphere (altitude $\lesssim 5\ km$) most cosmic rays are muons (see figure 5.1), moreover the other interacting particles are absorbed by the rocks, therefore it is correct assuming that mostly muons can reach the $\sim$ 100 $m$ deep ATLAS cavern and produce signals in the detector.

Measurements of cosmic rays at sea level [28] estimated a rate of 130 $Hz/m^2$ (for the total cosmic muon flux crossing unit horizontal area from above), assuming for cosmic muons at the ground $E \gtrsim 225\ MeV$. The mean energy of muons at sea level is $\approx 4\ GeV$. The energy spectrum is almost flat below 1 $GeV$, steepens gradually to reflect the primary spectrum ($\propto E_\mu^{-2.7}$) in the 10-100 $GeV$ range, and asymptotically becomes one power steeper for muon energy much more than 1 $TeV$.

In order to study the ATLAS detector performances using cosmic rays as particle source, samples of cosmic muons are generated and propagated toward the ATLAS cavern, then the output of the cosmic ray simulation is passed as input to the detector simulation.

Primary cosmic generation is performed via a specific generator (`CosmicGenerator`), providing single muons at surface level. The generation area is fixed by the user (for the ATLAS experiment a square area of $600 \times 600\ m^2$, centred with respect

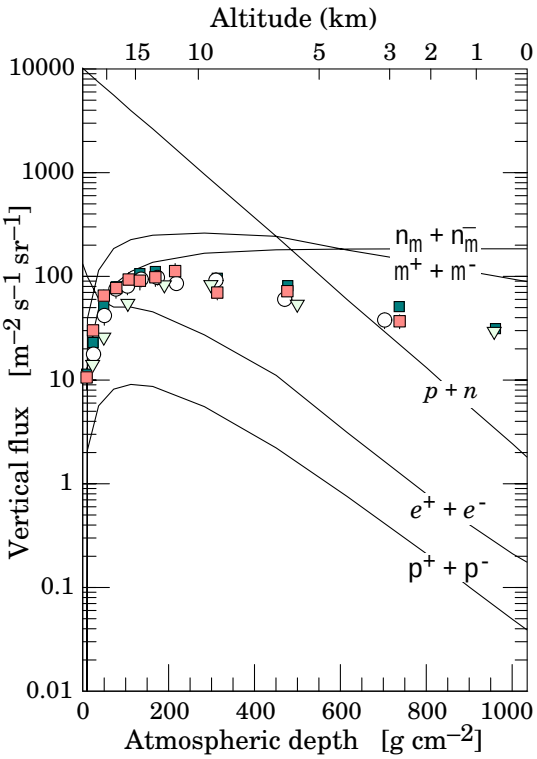


Figure 5.1: Vertical fluxes of cosmic rays with energy $>$ 1 *GeV* in the atmosphere [29]. The points show measurements of negative muons ($E_\mu >$ 1 *GeV*) [30, 31, 32, 33].

to the interaction point, is often used). The user can also decide the muon energy range at generation level, usually set from 10 $GeV$ to 2 $TeV$ for the ATLAS studies.

The ATLAS cavern shape is approximated with a box, containing the ATLAS detector with a full description of each subdetector.

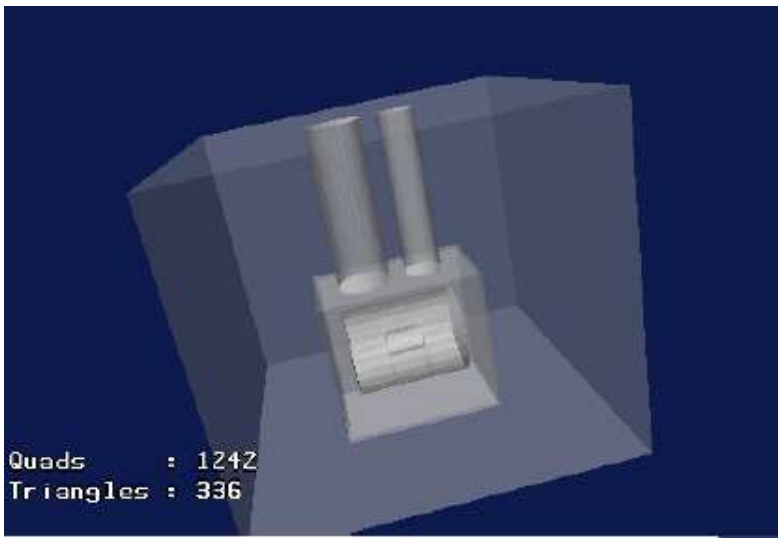


Figure 5.2: View of the ATLAS cavern as described in the simulation.

The rock overburden (for a $\sim 60\ m$ depth) and the main service shafts are simulated as well (see figure 5.2). For the rock a density of 2.33 $g/cm^3$ is considered, while for shafts and cavern walls the concrete density is 2.5 $g/cm^3$. Air is in the shafts and inside the cavern.

In order to reduce the processing time and avoid simulation of cosmics not going to hit any detector, user can require to propagate only muons pointing toward a "fiducial sphere" containing the ATLAS barrel. The sphere radius is set by user.

The cosmic ray simulation uses a large part of the processing time per event to propagate the primary muon through the rock overburden. A great number of secondaries are produced and propagated into the rock. A range cut is defined; the user can set this cut so to avoid the simulation of low energy secondaries that stop in the rock (the default range cut is set to 1 $mm$).

## 5.3 Cosmic muons in the ATLAS cavern

To study the RPC physics with cosmic ray in the ATLAS cavern, a simulation of $3 \cdot 10^5$ cosmic muons has been performed. The muon generation area on surface was limited to a square of $600 \times 600\ m^2$, centred with respect to the ATLAS interaction point, and the muon energy cut at ground was fixed at 1 $GeV$. These geometrical limit and energy cut are sufficient to consider every cosmic muons, that could contribute to the signal in the RPCs and produce triggers (see section 5.5.1 and 5.5.2). A cosmic muon was propagated only if its momentum pointed towards a "fiducial sphere" with a diameter of 17 $m$, containing the ATLAS barrel; it means that the maximum accepted muon inclination was 70 degrees. In figure 5.3 the generation spatial distribution of the simulated cosmic muons (black dots) is shown.

Once generated, the muons were propagated through the rock and the concrete, but only 1.7% muons reached the ATLAS detector and produced at least a signal in the RPCs. The ATLAS magnetic field was set on, so muons were bent in the detector. The muons reaching the RPCs are also shown in figure 5.3 by the green dots: their distribution is characterized by two different concentrations, which correspond to the ATLAS shaft positions (see figure 5.4). The muons generated in correspondence of the shafts do not essentially pass through the rocks, so also muons with a low energy reach the cavern. The shaft positions are summarized in table 5.1.

| ATLAS Shafts | Centre | Diameter |
|---|---|---|
| PX14 | $x = 1.7\ m$<br>$z = 13.5\ m$ | $18\ m$ |
| PX16 | $x = 1.85\ m$<br>$z = -16.7\ m$ | $12.6\ m$ |

Table 5.1: The ATLAS shaft positions.

The momentum distributions for all the simulated cosmic muons (on the left) and for only the ones of them, which reach the RPCs (on the right), are shown in figure 5.5. According to the Bethe-Bloch formula, a muon at the minimum of ionization needs an energy of about 25 $GeV$ to pass through a 60 $m$ thickness of rocks ($2.33\ g/cm^2$). In the momentum spectrum shown on the right side of figure 5.5, the particle with momentum up to $\sim$ 30 $GeV$ are only the cosmic

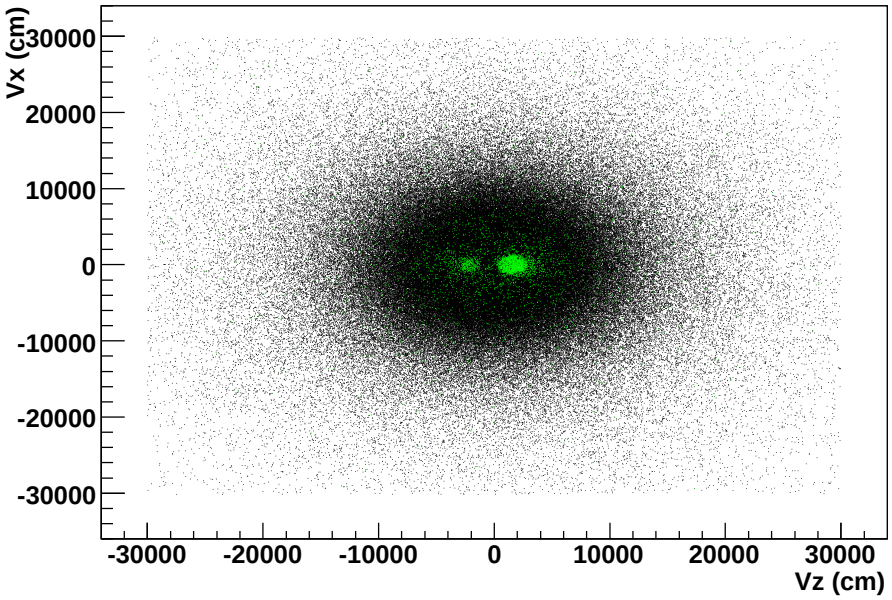


Figure 5.3: The muon generation area: the muons are uniformly generated on the whole $600 \times 600\ m^2$ square, but only if they (black dots) point towards the ATLAS barrel "fiducial sphere" they are propagated. The muons hitting the RPCs (green dots) are 1.7% of the generated sample.

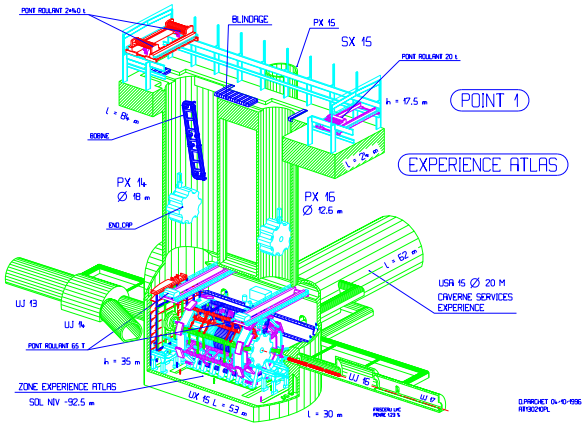


Figure 5.4: The ATLAS cavern: the walls and the shafts are visible.

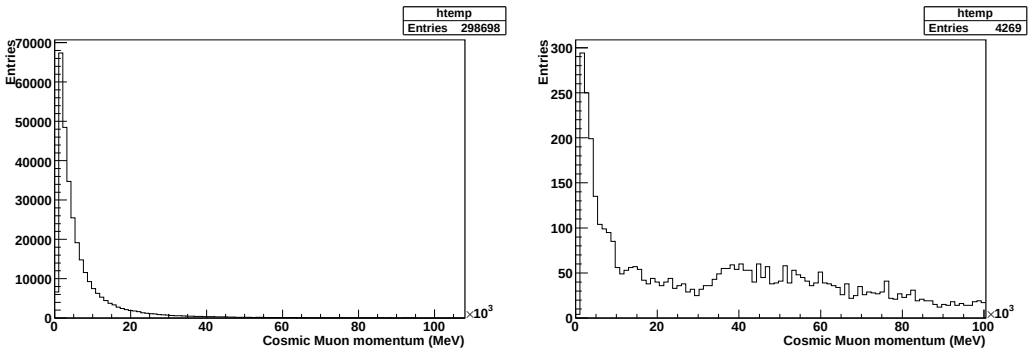


Figure 5.5: The momentum spectrum of the cosmic muons ($\propto E_{\mu}^{-2.7}$) at ground level is on the left. In the momentum distribution on the right side the muons reaching the RPCs are selected: muons with momentum below $\sim$ 30 $GeV$ can reach the cavern only if they pass through the shafts.

muons generated in correspondence of the shafts; the other muons need a larger energy to pass through the rocks and reach the RPCs.

The path, which the muons covered from the ground level to the RPCs, is plotted in figure 5.6 as a function of the muon momentum at generation.

### 5.3.1 Cosmic muon rate in the ATLAS cavern

The cosmic muon rate in the ATLAS cavern can be estimated by the simulation described above, taking into account some criteria:

- Measurements of cosmic rays at sea level [28] estimate a rate $R_{sea} = 130\, Hz/m^2$ for muons crossing an unitary horizontal area (from above), by assuming a minimum muon energy of $E_{min} \sim 225\ MeV$.

- A square area ($A$) is defined at ground level for the cosmic muon generation.

- A muon energy cut ($E_{cut}$) at generation is set to avoid unnecessary processing time, considering that low energy muons are absorbed before to reach the ATLAS detector. Only a fraction of the muon energy spectrum is simulated.

- In order to exclude muons pointing outside of the ATLAS barrel "fiducial sphere", a proper cut in the momentum direction is fixed.

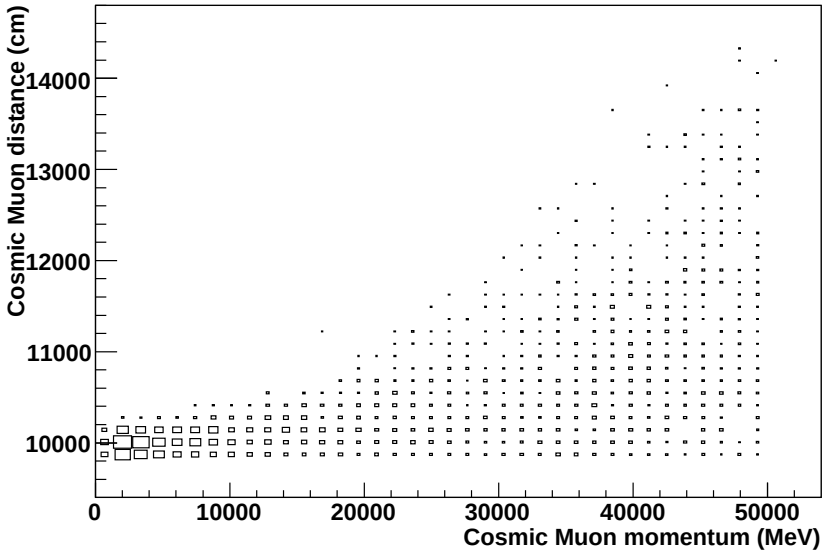


Figure 5.6: Path of muon reaching the RPCs as a function of the momentum at generation. Muons with momentum below $\sim 30\ GeV$ can reach the cavern only if they pass through the shafts ($\sim 90\ m$).

- A large fraction of all the generated and propagated cosmic muons are absorbed by the rocks and only a small percentage of them reaches the ATLAS barrel and produces signal in RPCs.

Therefore the rate can be expressed as follows:

$$R = \left( R_{sea} \cdot A \cdot \frac{\int_{E_{cut}}^{\infty} N(E)dE}{\int_{E_{min}}^{\infty} N(E)dE} \right) \cdot \frac{N_{\mu}^{sim}}{N_{\mu}^{gen}} \cdot \frac{N_{\mu}^{RPC}}{N_{\mu}^{sim}}, \tag{5.1}$$

where $N_{\mu}^{gen}$ is the number of all the generated muons and $N_{\mu}^{sim}$ is the number of the muons pointing toward the barrel "fiducial sphere". Finally $N_{\mu}^{RPC}$ takes into account only the muons reaching the ATLAS cavern and hitting the RPCs.

As presented in the table 5.2, for a simulation with a generation square of $600 \times 600\ m^2$ and a energy cut at ground level of $E_{cut} \geq 1\ GeV$ the cosmic muon rate in the ATLAS cavern is 2.2 *kHz*.

| | | |
|---|---|---|
| Rate at sea level | $R_{sea}$ | $130\ Hz/m^2$ |
| Generation area | $A$ | $600 \times 600\ m^2$ |
| Cut in the energy spectrum | $E_{cut} \geq 1\ GeV$ | 84% |
| Cut in the momentum direction | $N_\mu^{sim}/N_\mu^{gen}$ | $3.3 \cdot 10^{-3}$ |
| Muons reaching the RPCs | $N_\mu^{RPC}/N_\mu^{sim}$ | 1.7% |
| **Rate in the cavern** | **R** | **2178 Hz** |

Table 5.2: Cosmic muon rate in the ATLAS cavern obtained by a simulation generating muons at ground level on a $600 \times 600\ m^2$ area with an energy cut of 1 $GeV$ and defining a "fiducial sphere" containing the ATLAS barrel (diameter of 17 $m$). The $R$ value is calculated with the expression 5.1.

### 5.3.2 Results of the cosmic muon digitization

The distribution of the number of the RPC digits produced by the simulated cosmic sample described above is shown in figure 5.7. A peak at 5 is clearly visible. Five digits occur when a muon hits only one RPC, taking into account that a chamber is constituted by two detector layers (i.e. two gas gaps, as described in chapter 2) and digits are from both $\eta$ and $\varphi$ views, moreover strip clusters are considered by the simulation. Therefore on average a muon crossing an ATLAS RPC chamber produces 5.2 digits.

The digit distribution on the *x-y* plane is shown in figure 5.8 on the left. The ATLAS barrel layout of the RPC three stations in $\varphi$ view is reproduced by the digit positions: all the chambers are hit by the cosmic rays. and in particular the green points, relative to the events with less than 8 digits, are mainly concentrated in the outer stations. Moreover by observing the distribution of the number of digits in function of the $\eta$ stations, shown on the right side of figure 5.8, it has to be noted that muons which produce less than 8 digits mainly hit the outer stations also in the $\eta$ view. The outer stations (in both $\eta$ and $\varphi$ views) are located under the ATLAS shafts, therefore the events with less than 8 digits (just one hit RPC) are due to vertical muons passing through the shafts and reaching the detector in the regions between the barrel and the end-caps ($\eta \sim 1$), where the middle stations (BML/S) are shorter than the outer ones (BOL/S) along the *z* axis (see figure 5.9).

As a conclusion the peak at 5 in the distribution of the number of digits represents muons intersecting only a BOL/S chamber, that extends on a long distance in the *z* axis. Since the pivot planes according to the trigger logic (see chapter 4) are sited on the BML/S stations, these events can not give a trigger and are therefore

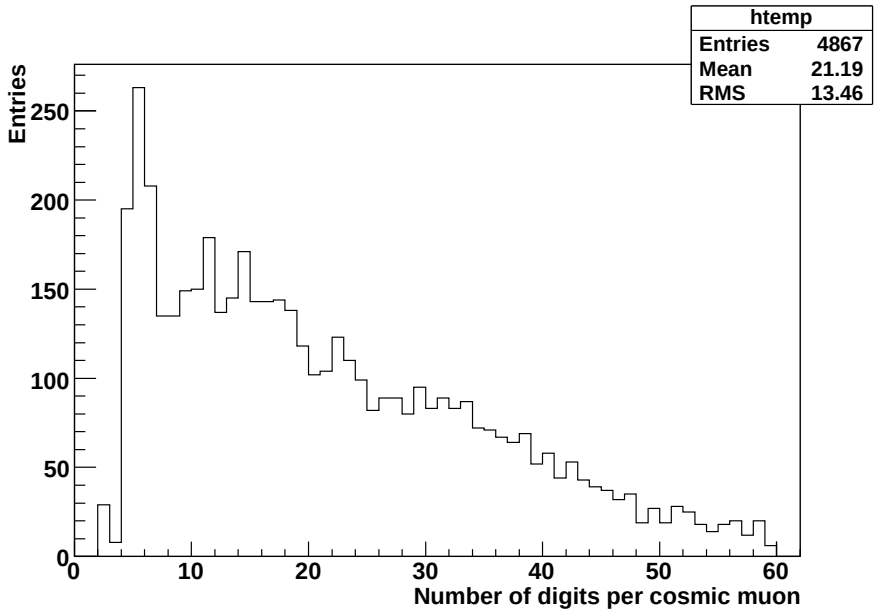


Figure 5.7: Distribution of the number of the RPC digits per cosmic muon. The peak at 5 is due to muons hit only one RPC (consisting of four read-out panels and considering the strip cluster mechanism).

eliminated.

## 5.4 The LVL-1 trigger with cosmic muons

In order to evaluate the LVL-1 muon trigger rate in the barrel for cosmic rays, a simulation of the muon trigger logic has been performed. The sample of $3 \cdot 10^5$ cosmic muons, described in section 5.3, was used as input for the LVL-1 trigger simulation.

The CMs were programmed with the following $p_T$ thresholds:

1. **Fully Open Window**: no coincidence window is fixed by the trigger logic, except the limit imposed by the hardware cabling (corresponding approximately to a $p_T$ threshold of about 3.5 *GeV*). This is the most accepting configuration.

2. **6 GeV**: the lowest ATLAS standard $p_T$ threshold for low-$p_T$ trigger (mainly dedicated to b-physics studies).

3. **10 GeV**: ATLAS standard $p_T$ threshold for low-$p_T$ trigger.

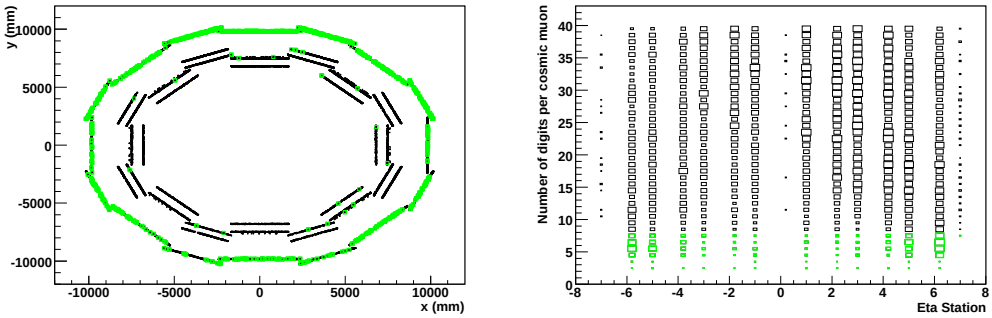


Figure 5.8: The digit distribution on the *x*-*y* plane ($\varphi$ view) is shown on the left, and the distribution of the number of digits as a function of the barrel $\eta$ stations (i.e. along the *z* axis) is shown on the right. The events with less than 8 digits are shown in green: these events are localized in the outer stations both in the $\varphi$ and the $\eta$ (stations -6, -5, 5 and 6) views.

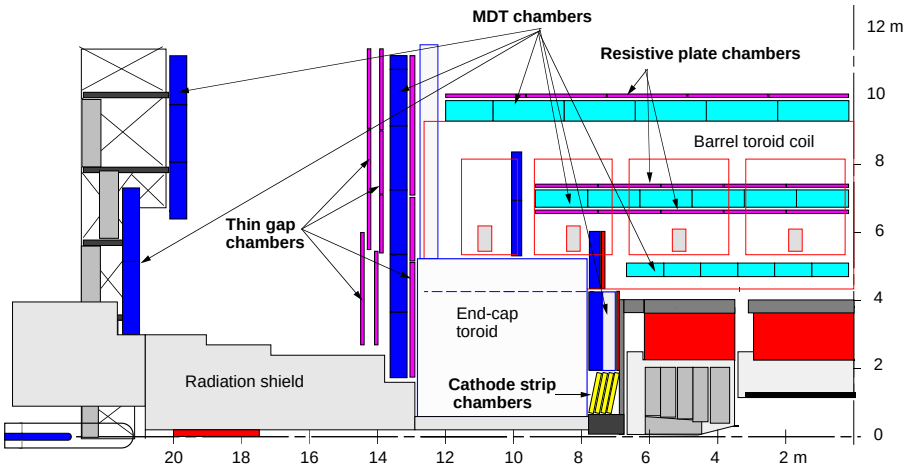


Figure 5.9: ATLAS Muon Spectrometer section (*z*-*y* plane): the middle RPC stations are shorter than the outer ones with respect to the *z* (horizontal) axis. The outer RPC stations are localized under the shafts and are hit by the vertical low energy cosmic muons, which reach the cavern without passing through the rocks.

4. **11 GeV**: this low value for the high-$p_T$ trigger allows to compare the results of this selection with the low-$p_T$ trigger results. In fact since this threshold value is comparable with the third low-$p_T$ threshold, the difference between the two triggers is the effect produced by requiring a further hit in the outer station, according to the high-$p_T$ trigger logic.

5. **20 GeV**: the main ATLAS standard muon $p_T$ threshold, useful for high-$p_T$ muon trigger.

6. **40 GeV**: also an important ATLAS standard muon $p_T$ threshold for high-$p_T$ trigger.

For cosmic muon trigger studies the low-$p_T$ trigger majority asked for $3/4$ spatial coincidences in the two doublets of the RPC middle stations; while the high-$p_T$ CMs were programmed to look for a $1/2$ signal in the outer doublet in coincidence with the low-$p_T$ trigger.

In section 5.3 it is observed that only 1.7% muons of the whole sample reach the ATLAS detector and produce at least a signal in the RPCs, but not all the cosmic muons reaching the RPCs have the characteristics necessary to produce trigger coincidences. Only 28% of the cosmic muons reaching the RPCs are selected by the LVL-1 trigger. And they are 0.5% of the whole sample.

The spatial distribution for muons producing signal in the RPCs and for muons selected by the LVL-1 trigger are compared in figure 5.10. The trigger preferentially selects the muons coming from the bigger ATLAS shaft. For these muons the momentum spectrum at generation level is shown in figure 5.11.

The distribution of the trigger $p_T$ thresholds crossed by the cosmic muons is shown in figure 5.12 and the relative trigger rates are presented in table 5.3. The trigger rate for each threshold was computed by considering a muon cosmic rate in the ATLAS cavern of 2.2 $kHz$ (see table 5.2) and multiplying this value by the fraction of muons crossing that threshold over the total number of the muons passing in the RPCs.

The trigger rates for cosmic muons relative to 6 $GeV$ threshold and 20 $GeV$ threshold are particularly relevant, since these values correspond to the ATLAS standard lower $p_T$ thresholds for low-$p_T$ trigger and high-$p_T$ trigger respectively. They are more than an order of magnitude lower than the muon trigger rates evaluated for the ATLAS experiment, which are $\sim$ 9.3 $kHz$ for the low-$p_T$ trigger (6 $GeV$ at low luminosity $10^{33}\ cm^{-2}s^{-1}$) and $\sim$ 1.4 $kHz$ for the high-$p_T$ trigger (20 $GeV$ at high luminosity $10^{34}\ cm^{-2}s^{-1}$) [26].

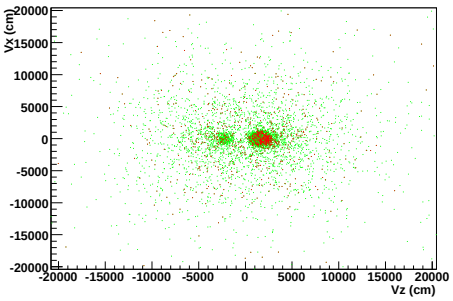


Figure 5.10: Generation spatial distribution: the green dots are the cosmic muons reaching the RPCs and the red dots are the muons selected by LVL-1 trigger only. The trigger preferentially selects the muons coming from the bigger ATLAS shaft (centred at $z = 13.5\ m$).

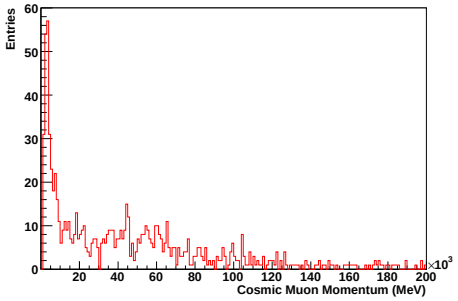


Figure 5.11: Momentum distribution at generation level of the cosmic muons selected by the LVL-1 trigger.

| LVL-1 Trigger | $p_T$ Threshold | Majority Coincidence | Trigger Rate |
|---|---|---|---|
| Low-$p_T$ | Fully Open Window | 3/4 | 607 *Hz* |
| | 6 *GeV* | 3/4 | 214 *Hz* |
| | 10 *GeV* | 3/4 | 141 *Hz* |
| High-$p_T$ | 11 *GeV* | Low-$p_T$ + 1/2 | 30 *Hz* |
| | 20 *GeV* | Low-$p_T$ + 1/2 | 21 *Hz* |
| | 40 *GeV* | Low-$p_T$ + 1/2 | 18 *Hz* |

Table 5.3: LVL-1 trigger rates for cosmic muons in the cavern. The rates estimated for the ATLAS experiment are $\sim$ 9.3 *kHz* for the low-$p_T$ trigger (6 *GeV* at low luminosity $10^{33}\ cm^{-2}s^{-1}$) and $\sim$ 1.4 *kHz* for the high-$p_T$ trigger (20 *GeV* at high luminosity $10^{34}\ cm^{-2}s^{-1}$) [26].

The ATLAS standard $p_T$ threshold trigger rates obtained in this study can be compared with the results produced by a fast Monte Carlo (MC) simulation and reported on the *ATLAS First-Level Trigger Technical Design Report* (LVL-1 TDR) [10]. It has to be considered that different values of the incident cosmic rate at the sea level are used to normalize the cosmic muon trigger rates in the ATLAS cavern. The incident cosmic rate at sea level was estimated 100 $Hz/m^2$, instead

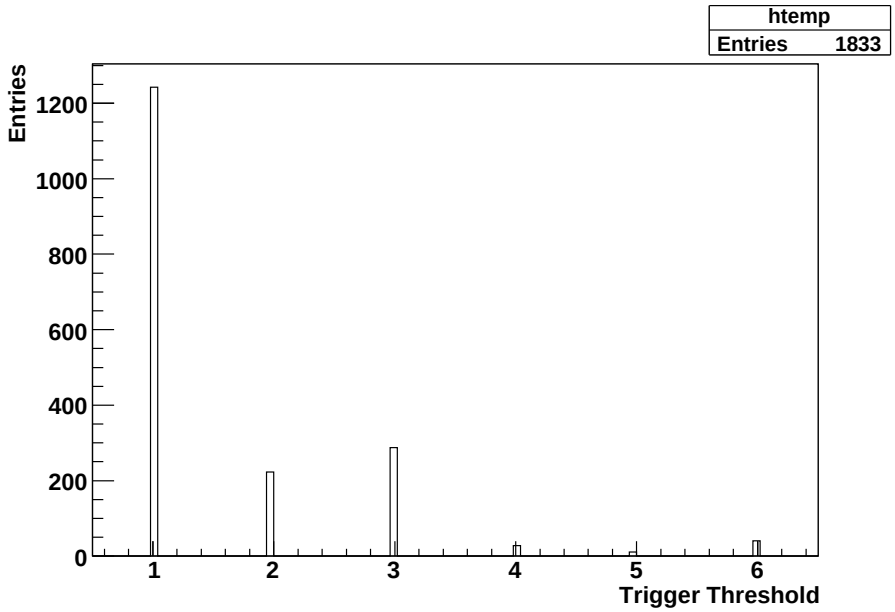


Figure 5.12: Distribution of the crossed $p_T$ thresholds for the cosmic muons. The thresholds from 1 to 3 are "Fully Open Window", 6 *GeV* and 10 *GeV* for the low-$p_T$ trigger; and the others are 11 *GeV*, 20 *GeV* and 40 *GeV* for the high-$p_T$ trigger.

of 130 $Hz/m^2$ as in this simulation; so that the trigger rates presented here have to be scaled by a factor of 0.77. The table 5.4 compares the trigger rates of this study for the ATLAS standard $p_T$ thresholds with the trigger rates reported in the LVL-1 TDR. The values are in good agreement.

| LVL-1 $p_T$ Threshold | New Results | Results in the LVL-1 TDR |
|---|---|---|
| 6 *GeV* | 165 *Hz* | $<$200 *Hz* |
| 20 *GeV* | 16 *Hz* | $<$10 *Hz* |

Table 5.4: The LVL-1 trigger rate results are compared with previous results reported on the *ATLAS First-Level Trigger Technical Design Report* [10]. In order to compare the values, the new cosmic trigger rates are normalized by an incident cosmic rate at the sea level of 100 $Hz/m^2$ (instead of 130 $Hz/m^2$ as in table 5.3).

## 5.5 Trigger study on three ATLAS muon towers

In order to study in detail the trigger performances with cosmic muons, a dedicated simulation considering only three muon towers of the ATLAS Muon Spectrometer has been performed.

The chosen towers are the first three $\eta$ stations of the half barrel at $\eta > 0$ in the barrel muon sector 13, which is sited at $\varphi = 3/2\pi$ (see figure 5.13). These are the first muon towers tested in the cavern with cosmic muons.

A muon tower consists of three RPC stations (see chapter 4), each one composed by eight gas volumes arranged in two layers. Two strip panels read a gas volume out: one in the $\eta$ view and the other in the $\varphi$ view.

According to the LVL-1 trigger segmentation, a muon sector in the barrel is divided in four trigger sectors, two for each half barrel ($\eta < 0$ and $\eta > 0$). As shown in figure 5.13, the trigger sectors assigned to the muon sector 13 at $\eta > 0$ are identified by the number 55 (at $x < 0$) and 56 (at $x > 0$). Each trigger sector is segmented in trigger towers as the muon sectors, so a muon tower is constituted by two trigger towers, one for the trigger sector 55 and the other for the trigger sector 56. The trigger segmentation of a half barrel muon sector is shown in figure 5.14. Two Pad boards, one for low-$p_T$ trigger and one for high-$p_T$ trigger, are mounted on a muon tower for each trigger sector.

Three muon towers and, therefore, six LVL-1 trigger towers (corresponding to six low-$p_T$ trigger Pads and six high-$p_T$ trigger Pads) are considered in this study.

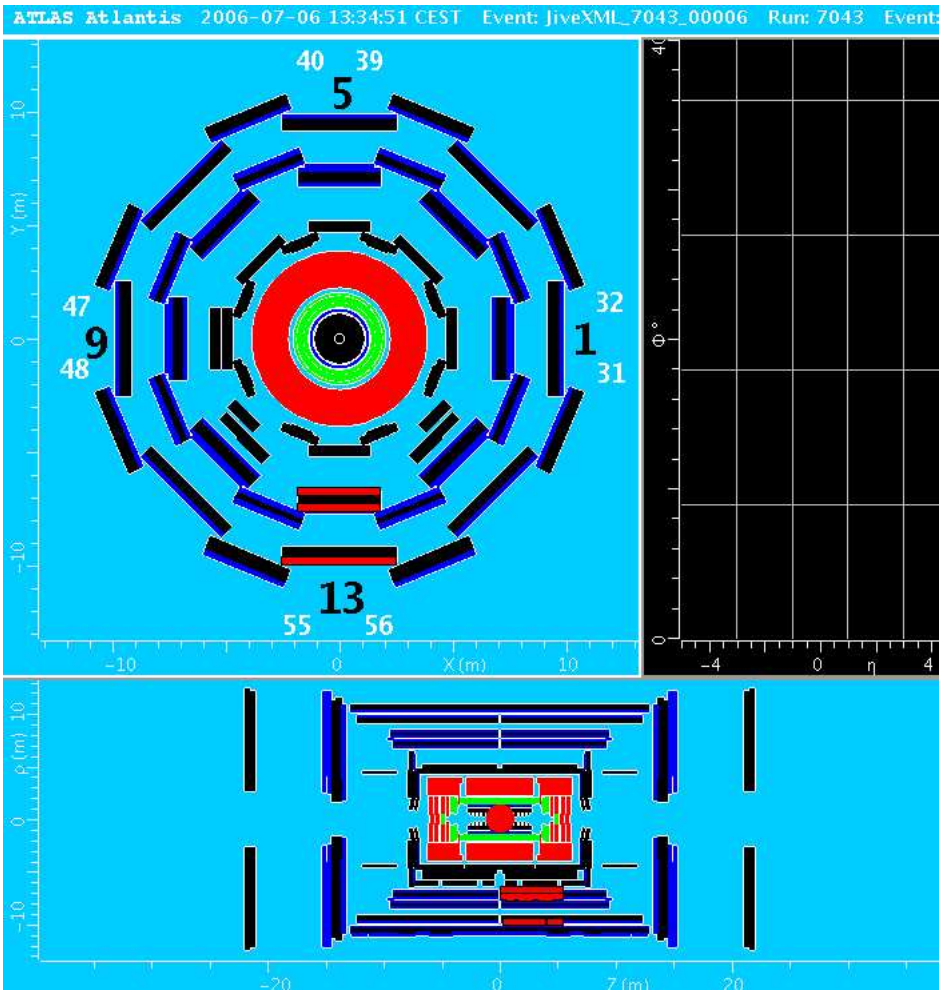


Figure 5.13: Scheme of the ATLAS barrel segmentation. In the $\varphi$ view (up) the Muon Spectrometer is segmented in 16 sectors, each one composed by 4 LVL-1 trigger sectors (2 at $\eta < 0$ and 2 at $\eta > 0$). The black and the white numbers indicate the spectrometer and the trigger sectors at $\eta > 0$ respectively. In the $\eta$ view (down) the barrel is segmented in 12 muon projective towers (or $\eta$ stations), 6 at $\eta < 0$ and 6 at $\eta > 0$. The RPCs of the sector 13 in operation are emphasized in red.

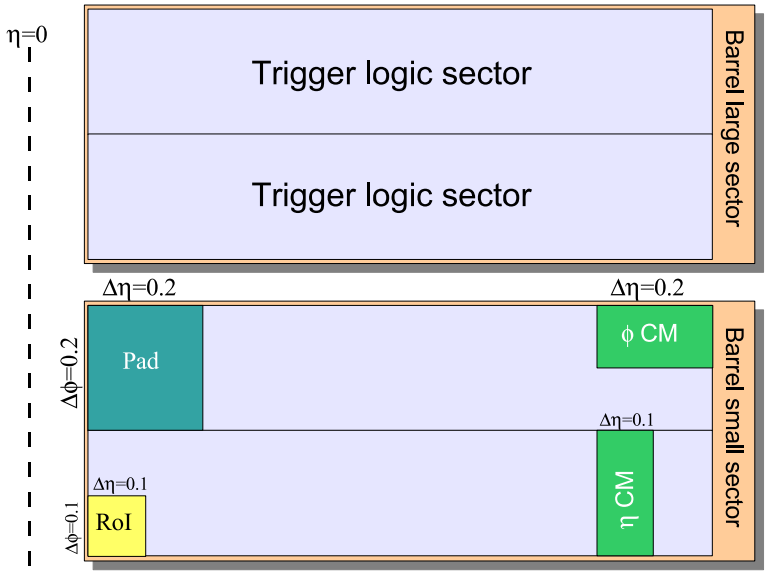


Figure 5.14: Segmentation of the half barrel muon sectors, according to the LVL-1 trigger logic. Approximative dimensions of RoI, Pad and CM are also shown.

A sample of $1.6 \cdot 10^6$ cosmic muons pointing towards the three stations of the muon sector 13[1] has been simulated. The generation area at ground level was a square of $600 \times 600\ m^2$, centered in the $p$-$p$ interaction point, and a $E \geqslant 1\ GeV$ cut at generation was set.

In this simulation the ATLAS magnetic field was set off, in order to compare the simulation results with the data collected during summer 2006, when the magnet was still not operational.

For the LVL-1 trigger simulation, the Coincidence Matrices were programmed with the $p_T$ thresholds and majority coincidences described in section 5.4 (*Fully Open Window*, 6 *GeV*, 10 *GeV* with majority 3/4 for the low-$p_T$ trigger, and 11 *GeV*, 20 *GeV* and 40 *GeV* with majority 1/2 for the high-$p_T$ trigger). It has to be stressed that, since in this simulation the magnetic field was off, the trigger thresholds are not significant for the $p_T$ selection.

The LVL-1 trigger rates in the cavern are calculated for the six trigger towers under study with the expression 5.1, considering in $N_\mu^{RPC}$ only the muons hitting the RPCs of those towers. Then multiplying this value by the fraction of the muons selected by the LVL-1 trigger over the muons hitting the RPCs, the trigger rate is

[1] In order to select only muons pointing towards the studied RPCs, a "fiducial sphere" with a radius of 4.3 $m$ containing the first three $\eta$ stations of sector 13 is defined.

obtained.

The trigger rates estimated for each LVL-1 $p_T$ thresholds are shown in figure 5.15 for the trigger towers of the sector 55 and in figure 5.16 for the trigger towers of the sector 56. The cosmic muon trigger rates for the ATLAS standard

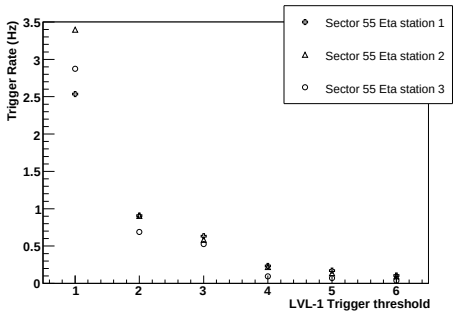


Figure 5.15: LVL-1 trigger rate with cosmic muons for three towers of the trigger sector 55. The trigger rates are plotted as a function of the crossed $p_T$ thresholds (1, 2 and 3 are the low-$p_T$ trigger thresholds and 4, 5 and 6 are the high-$p_T$ trigger thresholds). No magnetic field is in the simulation.

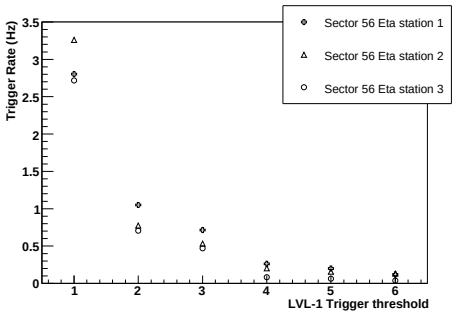


Figure 5.16: LVL-1 muon trigger rate with cosmic muons for three towers of the trigger sector 56. The trigger rates are plotted as a function of the crossed $p_T$ thresholds (1, 2 and 3 are the low-$p_T$ trigger thresholds and 4, 5 and 6 are the high-$p_T$ trigger thresholds). No magnetic field is in the simulation.

$p_T$ threshold are $\sim 1\ Hz$ and $< 0.3\ Hz$ for the low-$p_T$ trigger (threshold 2 corresponding to a $p_T \geq 6\ GeV$ cut) and the high-$p_T$ trigger (threshold 5 corresponding to a $p_T \geq 20\ GeV$ cut) respectively. The rate increases of a factor 3 with respect to the standard low-$p_T$ trigger (threshold 2), if the coincidence window is fully open (threshold 1).

### 5.5.1 Dependence on the generation area

In order to check that all the cosmic muons contributing to the trigger rate are considered in the simulation, the trigger rate dependence on the muon generation square is studied.

The study is limited to the three first $\eta$ stations of the ATLAS sector 13 at $z > 0$. The stations are arranged horizontal, they have been chosen to maximize the cosmic flux on the chamber surface. Moreover the $\eta$ station 3 is sited in the region under the $PX14$ shaft (see figure 5.17), that is the region of minimum

cosmic muon energy loss, as observed in section 5.3. The total trigger rate is calculated by integrating the three stations. Only the rate with the "Fully Open Window" trigger setting is considered for the present study.

The cosmic muon samples were simulated with a muon energy cut at generation fixed at $E_{cut} = 1\ GeV$ and varying the side of the generation square from 100 to 600 $m$. The total trigger rate as a function of the square side is shown in figure 5.18. The rate increases with the square dimension, reaching a plateau value for square side greater than 300 $m$. Therefore a muon generation in a $600 \times 600\ m^2$ area is fully sufficient to include all the cosmic muons contributing to the trigger rate in the ATLAS cavern.

### 5.5.2 Muon energy cut at generation

A muon energy cut is applied to the cosmic muon spectrum in generation. In order to check that the 1 $GeV$ energy cut does not perturb the trigger rate evaluation, a study of the trigger rate dependence on the energy cut is presented.

The study is limited to the three first $\eta$ stations of the ATLAS sector 13 at $z > 0$ and the total trigger rate is calculated by integrating the three stations. The presented results are for the "Fully Open Window" trigger setting, which is the most accepting configuration.

The cosmic muons were simulated with the characteristics described in section 5.5, only the energy cut was modified, ranging from 1 to 10 $GeV$.

In figure 5.19 the trigger rate is shown as a function of the muon energy cut at generation: it is constant up to $E_{cut} \sim 4\ GeV$ and decreases for cut at larger energy value.

In conclusion, the trigger rate can be efficiently estimated, if the muon energy cut at generation is lower than $\sim 4\ GeV$. It has to be stressed that in the present study the ATLAS magnetic field was off; the muon energy cut could be probably increased, if muons are bending by the magnetic field.

### 5.5.3 Simulation results and data

A preliminary commissioning test of the three muon stations of the ATLAS sector 13 described above was carried out in the cavern (summer 2006). The RPCs worked with a high voltage of 9.6 $kV$ and an electronics threshold of 1.0 $V$ (the set-up used in the test is illustrated in section 6.1). The magnetic field was off.

To select events due to cosmic muons, the low-$p_T$ trigger was programmed

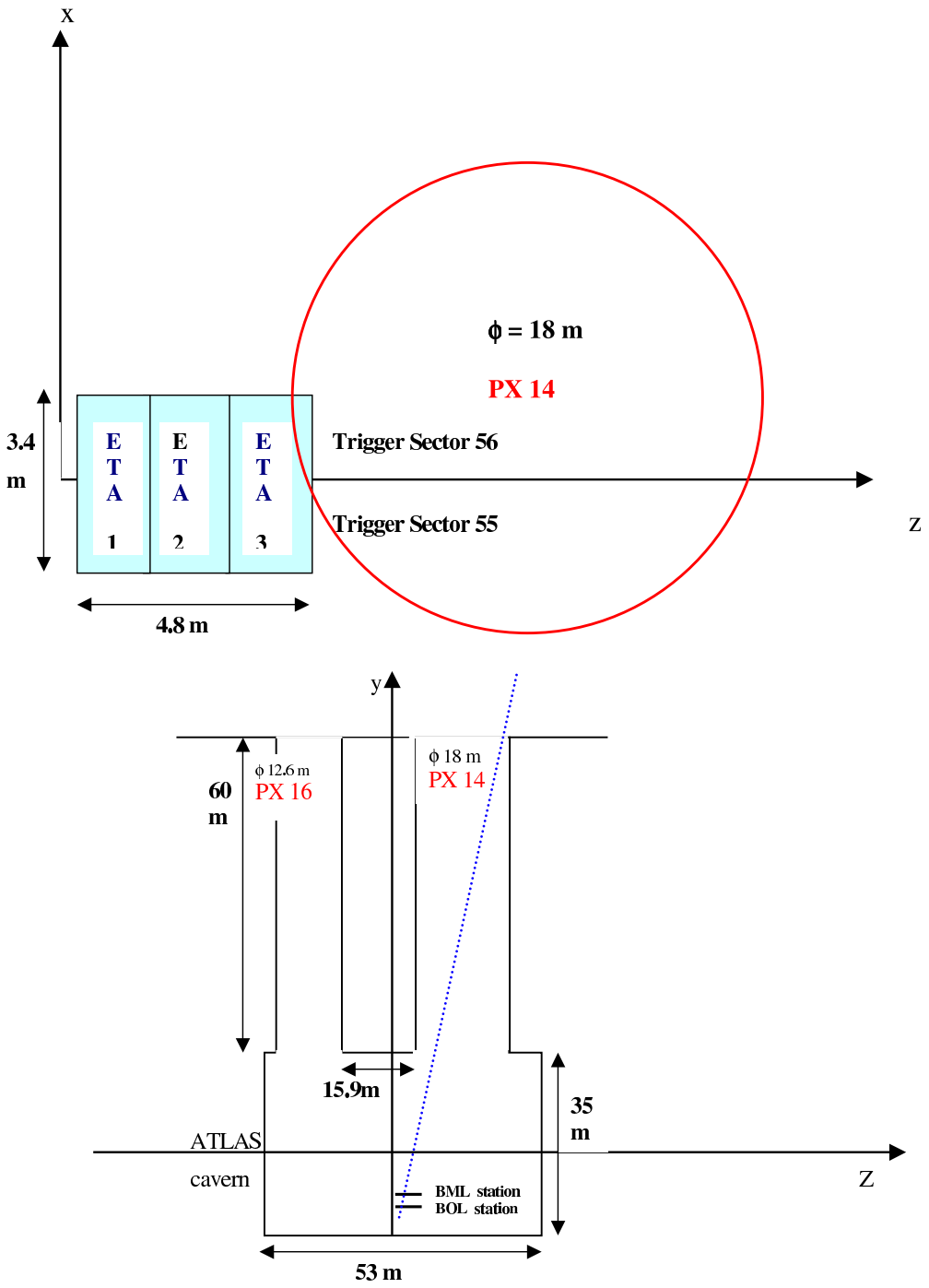


Figure 5.17: Position of the sector 13 muon stations in operation with respect to the shafts.

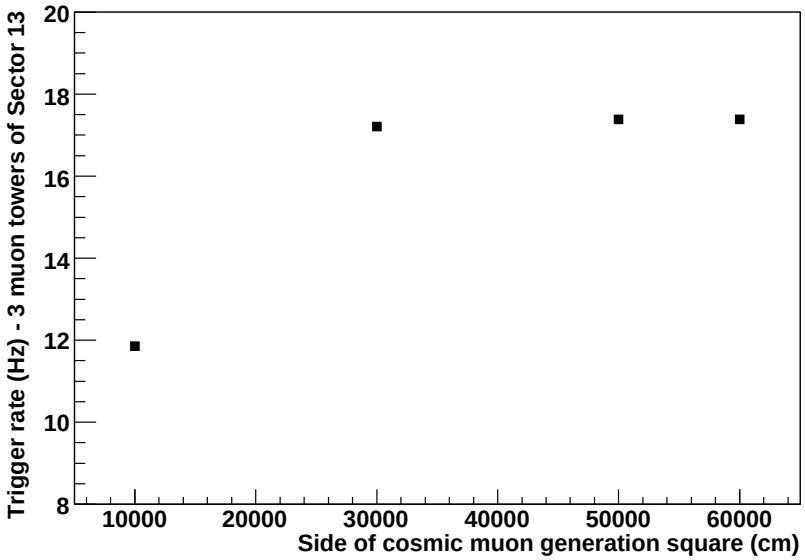


Figure 5.18: Trigger rate dependence on the side of the cosmic muon generation square.

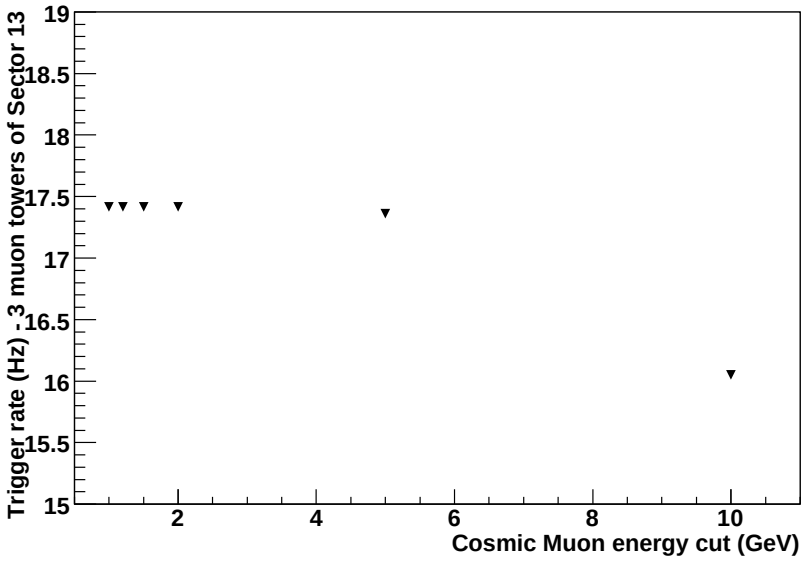


Figure 5.19: Trigger rate dependence on the cosmic muon energy cut at ground level.

to search coincidences within the fully open window between the two low-$p_T$ doublets (RPC 1 and RPC 2) satisfying the two-out-four (2/4) logic and using only the $\varphi$ view. In total, six muon trigger towers, belonging to the trigger sectors 55 and 56, were operative.

The same LVL-1 trigger logic was simulated using as input the cosmic sample described above (generation area of $600 \times 600\ m^2$ and $E_\mu \geq 1\ GeV$ cut at ground level). The trigger rates obtained for this configuration for the three towers of the trigger sectors 55 and 56 are shown in figures 5.20 and 5.21 respectively and are compared with the results presented in section 5.5. Summarizing these plots show

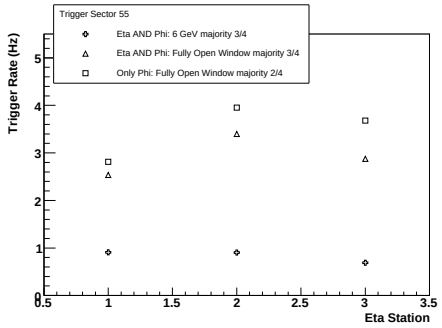


Figure 5.20: LVL-1 muon trigger rates obtained by simulation for three trigger towers of the trigger sector 55: different settings for the LVL-1 trigger logic are shown.

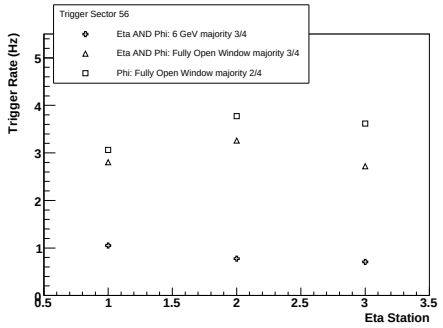


Figure 5.21: LVL-1 muon trigger rates obtained by simulation for three trigger towers of the trigger sector 56: different settings for the LVL-1 trigger logic are shown.

the trigger rates simulated for the following trigger logic settings:

1. low-$p_T$ trigger in the $\eta$ and $\varphi$ views with the ATLAS standard configuration: $p_T$ threshold of 6 $GeV$ (in this simulation the magnetic field was off, therefore the trigger threshold is ineffective for the $p_T$ selection) and 3/4 coincidence majority.

2. low-$p_T$ trigger in the $\eta$ and $\varphi$ views with the fully open coincidence windows and the 3/4 coincidence majority.

3. low-$p_T$ trigger only in the $\varphi$ view with the the fully open coincidence windows and the 2/4 coincidence majority.

In the cases 2 and 3 for both the trigger sectors, the $\eta$ station 2 shows a larger trigger rates with respect to the $\eta$ station 1, since increasing $\eta$ the stations of the

sector 13 are getting closer to the region under the shaft, that is the region of minimum energy loss for almost-vertical cosmic muons.

This effect is less evident in the $\eta$ station 3, since the trigger roads are defined by assuming the muon path to be a straight line with the origin at the interaction point, therefore towers at larger $\eta$ have more inclined roads and the trigger does not select the vertical tracks.

In the ATLAS standard trigger setting (case 1) the trigger rate due to cosmic muons decreases increasing $\eta$, therefore the shaft position does not influence the trigger rates of these muon stations.

Finally, the simulation results for the case 3 can be compared with the data collected at the first commissioning test for the trigger sectors 55 and 56. It has to be taken into account that no detector noise was introduced in the simulation, therefore for the comparison the rate due to fake triggers has to be added to the rates obtained by the simulation.

The fake trigger rate can be estimated, considering the single hit rate measured in a Coincidence Matrix during the cosmic test in the cavern ($R_{lay} \sim 5\ kHz$ was measured in a $\varphi$ CM for a BML layer) and the chosen coincidence time window ($\Delta t_{trigW} = 25\ ns$ a LHC bunch-crossing range). The trigger configuration required a coincidence between a pivot layer and one of the confirm layers belonging to the RoI, therefore to calculate the rate of fake coincidences due to detector noise, the single hit rate of a pivot layer has to be multiplied for the single hit rate of each confirm layer, which is connected to the same CM. In a low-$p_T$ station, the single hit rate ($R_{lay}$) is equivalent both for the pivot and the confirm layers, since the RPC layers have the same dimensions (area $A \sim 170 \times 170\ cm^2$); therefore the fake trigger rate is given by the following expression:

$$R_{ftrig} = 2(R_{lay} \cdot nR_{lay}) \cdot \Delta t_{trigW} \tag{5.2}$$

where $n$ is the number of the confirm layers belonging to the same RoI and the factor 2 is considered because in each muon trigger tower two pivot layers can be fired.

According to the expression 5.2, the rate due to fake triggers is about 2.5 $Hz$ for the $\eta$ stations 1, since there is a only confirm doublet ($n = 2$) in the RoI of these trigger towers. Instead in the $\eta$ stations 2 and 3 the RoIs consist of two confirm doublets: one of its muon station and the other due to the overlap with the previous muon station, according to the LVL-1 trigger logic; therefore in these cases $n$ is equal to 4 in the expression 5.2 and the fake trigger rate is about 5 $Hz$.

Adding the values estimated for the trigger fake rates to the simulated results,

the data collected during the first commissioning test agree with the simulation within a factor 3, as shown in table 5.5.

| Trigger Rates | | | | |
|---|---|---|---|---|
| | Trigger Sector 55 | | Trigger Sector 56 | |
| $\eta$ station | Data | Simulation | Data | Simulation |
| 1 | 8 | 5.3 | 4 | 5.7 |
| 2 | 16 | 9.0 | 9 | 8.8 |
| 3 | 23 | 8.7 | 16 | 8.6 |

Table 5.5: The LVL-1 muon trigger rates for three $\eta$ stations of the barrel sector 13: preliminary data are compared with the simulation results. A fake trigger rate, calculated according to 5.2, of 2.5 *Hz* and 5 *Hz* is added to the simulated trigger rate of the station 1 and of the stations 2 and 3 respectively.

It has to be stressed that this commissioning test was the first debugging of the installed detectors and the related work is still going on. Moreover the simulation concerns the whole ATLAS detector, whereas during the test a significant part of the detector was not yet installed in the cavern (the inserted end-cap structures, the shielding material and part of the calorimeters). The cosmic muon absorption in these structures could contribute to explain the lower rates of the simulated results respect to the experimental data.

## 5.6 Study of different LVL-1 trigger schemes for cosmic muons

The estimated cosmic muon trigger rate of 214 *Hz* for the standard trigger configuration is fine during the ATLAS experiment running, considering that the trigger must select only muons coming from *p*-*p* collisions, but it is low for data acquisition during commissioning phase, when the cosmic rays are used as particle source. A dedicated trigger scheme should be used therefore to allow the selection of tracks with many orientations, so to improve the trigger rate and to ensure the data taking for each subdetectors in each position (inner or outer, vertical or horizontal).

The LVL-1 trigger logic and the cable connections are optimized to select muons coming from the interaction vertex (as for *p*-*p* collisions), that limits the

possibility of varying the trigger scheme: only trigger thresholds and majority are programmable and so modifiable. Therefore a different trigger scheme have to be based only on modification of thresholds set in the Coincidence Matrices.

Possible different trigger schemes, useful for cosmic muon selection, have been analyzed.

**Fully Open Coincidence Window.** This is the most accepting scheme. It consists of considering every coincidence allowed by cable connections within a CM. Only the low-$p_T$ trigger is performed, i. e. the trigger selects the muons providing a $3/4$ coincidence in the two doublets of the RPC middle station. In this case the muon tracks always point toward the interaction point, but the coincidence windows are as large as possible. As shown in table 5.3, in this configuration the LVL-1 trigger rate is expected in the barrel to be 607 *Hz*, which is a factor $\sim 3$ larger than the standard trigger rate.

**Coincidence only in the pivot doublet.** In this configuration only the pivot doublet (station RPC 2) is considered by the trigger. In order to program this configuration, the RPC 1 station has to be masked simulating a coincidence with the confirm doublet ("masking to one" ). Then a $4/4$ coincidence is requested, that corresponds to a less restrictive $2/2$ coincidence in the RPC 2 doublet. In this way a higher inclination is allowed for the muon tracks, depending on the position in the ATLAS detector. and the LVL-1 trigger rate increases to 1107 *Hz*, which is almost double with respect to the previous configuration.

| Trigger Scheme | Majority Coincidence | Trigger Rate |
|---|---|---|
| ATLAS standard $p_T \geqslant 6\ GeV$ | $3/4$ | 214 *Hz* |
| Fully Open Coincidence Window | $3/4$ | 607 *Hz* |
| Only pivot doublet | $2/2$ | 1107 *Hz* |

Table 5.6: Cosmic muon trigger rates expected for different trigger schemes.

In table 5.6 the trigger rate expected with the ATLAS standard threshold is compared with the fully open coincidence windows and requiring the coincidences only in the pivot plane. In conclusion, in the tests with cosmic rays the trigger rates can be improved of a factor 5 with respect to the standard LVL-1 configuration, if the scheme with the coincidences only in the pivot plane is chosen. This configuration allows to selects also the vertical cosmic muons (having

the maximum probability), which do not pass around the interaction point, providing a larger data sample.

### Further trigger configuration for cosmic muons

The trigger configuration with fully open coincidence windows and 2/2 majority coincidence only in the pivot doublet is the trigger scheme with the highest acceptance. It could be used for the Muon Spectrometer commissioning and calibration in the barrel, since it can select muons on all the muon detector chambers. Although in order to trigger muons for inner subdetectors a selection of muons crossing the $p$-$p$ collision region is necessary. A further request, regarding a selection of muon tracks crossing the interaction vertex region, has to be added to the trigger algorithm, using the implemented logic.

As described in chapter 4, the MUCTPI receives the trigger information from all the Sector Logic boards, then elaborates the coincidence results, counting the number of muon candidates for each of the six $p_T$ thresholds, and passes the multiplicity information to the Central Trigger Processor (CTP). It is the CTP, that combines the information from the LVL-1 trigger processors and makes the final LVL-1 acceptance decision. The CTP however receives only the final trigger results and it does not know which trigger tower the selected muons have passed through, so it is not able to perform spatial selection.

A possible trigger configuration has been suggested by the Rome 1 Trigger Group. Since the CTP can only distinguish information regarding the trigger $p_T$ thresholds, it is convenient to diversify the towers symmetrical respect to the interaction point, by programming their Coincidence Matrices with different trigger thresholds. In this way the selection of events with two triggers with different thresholds is equivalent to a spatial selection, because these triggers are produced by two towers symmetrical respect to the interaction point. It is important to note that in this configuration the thresholds only work as tags for the trigger towers and does not perform muon momentum cut. Indeed in each trigger tower the muon selection is obtained by "masking to one" the confirm plane and searching a 2/2 coincidence in the pivot doublet with the fully open coincidence window, so to increase the trigger rate in both the trigger towers.

An example is here provided to help in the understanding the concept described above. In order to select the muons coming from above and crossing the upper half barrel at $z > 0$ and the bottom half barrel at $z < 0$, the CMs in the upper sector at positive $z$ are programmed with a threshold called "1", while the CMs

in the bottom sector at negative $z$ are programmed with a threshold called “2”. Then the CTP menu has to be programmed to select only events with two selected muons, one with the trigger threshold ”1“ and the other with the trigger threshold ”2“. A time coincidence window has to be set, taking into account the muon time of flight passing through the whole ATLAS detector. This condition necessarily implies that a single muon crossed the ATLAS detector, passing through the inner subdetectors.

A trigger rate estimate for this trigger configuration is still to be performed. In fact before computing the trigger simulation with the described scheme, the timing information has to be necessarily included in the detector simulation, so to evaluate the muon time of flight in the detector.

## 5.7 Conclusions

Before starting the ATLAS experiment, a phase of detector commissioning is foreseen to check the correct working and the alignment of each subdetector. The first commissioning test is carried out with cosmic rays triggered by the RPCs and the first experimental results are compared with simulated data. In the simulation program the cosmic muons have been generated at surface level on an area of $600 \times 600\ m^2$ centred respect to the ATLAS detector, with a lower energy cut of $1\ GeV$. It has been shown that these parameters are fully sufficient to include all the cosmic muons, which are triggered in the ATLAS cavern. Muons with energy below $\sim 30\ GeV$ at ground level reach the cavern only if they cross the shafts. The cosmic muon rate simulated in the ATLAS cavern is $2.2\ kHz$.

The trigger rates only due to the cosmic muons for the ATLAS barrel standard LVL-1 trigger logic have been estimated as $214\ Hz$ for the low-$p_T$ trigger with a $p_T$ threshold of $6\ GeV$ and $21\ Hz$ for the high-$p_T$ trigger with a $p_T$ threshold of $20\ GeV$. These values, which are at least an order of magnitude lower than the muon trigger rates due to the $p$-$p$ collisions, are not sufficient to ensure a high acquisition rate during the commissioning phase. As a consequence, different configurations of the LVL-1 trigger have been studied to select also muons not necessarily passing around the interaction point (as the LVL-1 standard configuration for the $p$-$p$ collisions requires).

Two trigger schemes were simulated:

1. the low-$p_T$ trigger was simulated with the fully open coincidence windows (corresponding approximately to a $p_T$ threshold of $3.5\ GeV$); in this way

the trigger rate is increased of a factor $\sim 3$.

2. the low-$p_T$ trigger was studied, requiring trigger coincidences only in the pivot doublets, so to allow the selection of also the vertical cosmic muons (having the maximum probability), which do not pass around the interaction point. This configuration increases the trigger rate of a factor $\sim 5$.

A further simulation considering only six trigger towers of the sector 13 (which were under test) has been performed. The cosmic muon rates found for a single trigger tower of the sector 13 are $\sim 1$ *Hz* and $< 0.3$ *Hz* for the low-$p_T$ trigger with the $p_T$ threshold of 6 *GeV* and for the high-$p_T$ trigger with the $p_T$ threshold of 20 *GeV* respectively. It has to be noted that in this simulation the magnetic field was off (contrary to the previous one), therefore the trigger thresholds are ineffective for the $p_T$ selection. The rate increases of a factor 3 with respect to the standard low-$p_T$ trigger, if the coincidence window is fully open. In this case the stations of the sector 13, which are closer to the region under the shaft, show a larger trigger rate, although this effect becomes less evident for the stations at larger $\eta$, since these towers have more inclined roads and the trigger does not select the vertical tracks from the shaft.

Finally a first commissioning test of three muon towers in the ATLAS cavern made possible a comparison of the simulated results with the data collected in the cavern, although the detector debugging is still going on. The data agree with the simulation within a factor 3. However it has to be stressed that the simulation concerns the whole ATLAS detector, whereas during the test a significant part of the detector was missing in the cavern (the inserted end-cap structures, the shielding material and part of the calorimeters), so the cosmic muon absorption could contribute to explain the lower rates of the simulated results respect to the experimental data.

# Chapter 6

# First studies with cosmic muons in the ATLAS cavern

## 6.1 The first test of a Muon Spectrometer sector in the ATLAS cavern

Since 2004, the ATLAS muon barrel installation has started. The barrel toroid and large part of the muon instrumentation is by now already mounted in the cavern as well as the Inner Detector (except the pixel detector) and the Calorimeters.

A photo of the ATLAS barrel Spectrometer at the end of July 2006 is shown in figure 6.1. The toroid coils are visible, with most of the muon stations inserted between them. The Calorimeter is situated in the centre. Details of the muon stations are shown in figure 6.2. RPCs assembled with the MDT chambers are visible for the outer stations.

In summer 2006 the first test of a Muon Spectrometer sector was carried out. Three muon towers in the ATLAS barrel sector 13 (see figure 6.4) were selected for the test. An event display in figure 6.3 reproduces a cosmic muon crossing the muon stations in operation. The yellow lines are the fired RPC strips.

A muon tower consists of three stations: the Inner, the Middle and the Outer, starting from the interaction point. The muon stations are arranged to form projective towers, pointing to the ATLAS centre. Two kinds of barrel sectors are in the Muon Spectrometer: *Large* sectors and *Small* sectors, according to the muon station dimensions. The muon sector 13 is a Large Sector (also called $\varphi$ station 7). Each muon sector is divided in 4 LVL-1 trigger sector (2 at $\eta < 0$ and 2 at $\eta > 0$), according to the trigger logic. The barrel sector numbering scheme is

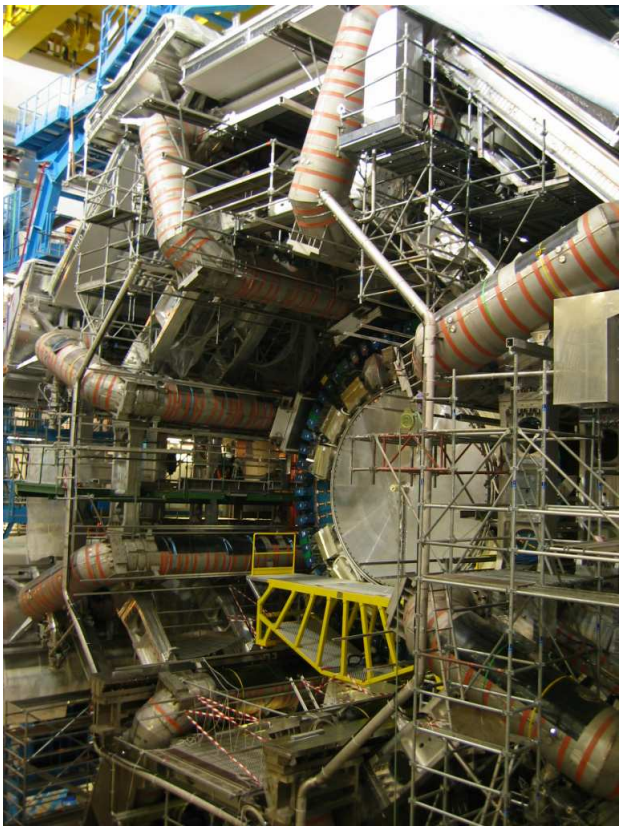

Figure 6.1: Photo of the ATLAS barrel section at the end of July 2006. The magnet toroid coils are visible.

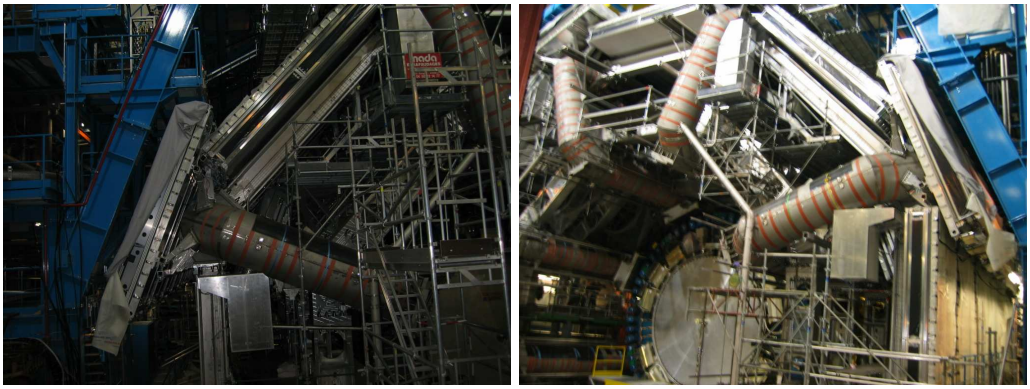

Figure 6.2: Details of the ATLAS barrel. The muon subdetectors are visible: MDTs are assembled with RPCs.

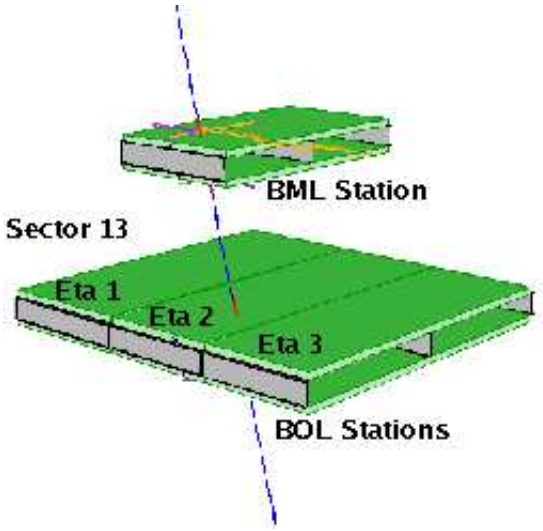


Figure 6.3: Event display for the ATLAS barrel sector 13. A cosmic muon crosses the muon stations. The yellow lines are the fired RPC strips. The upper chamber is a BML station, and the three bottom chambers are the BOL stations (fired RPC strips are not visible, because they are below the MDT chambers).

shown in figure 6.4 (black numbers are for the muon sectors and white numbers for the trigger sectors).

The Barrel Inner Large (BIL) stations are constituted by only the MDT chambers. In the Barrel Middle Large (BML) stations instead the MDT chambers are assembled between two RPCs. Finally in the Barrel Outer Large (BOL) stations the MDTs have the RPCs mounted downstream. The RPC chambers of a muon tower are called "BML Confirm", "BML Pivot" and "BOL Confirm", according to their functions in the trigger logic. An assembled BML station ready for the installation is shown in figure 6.5.

The muon sector 13 towers in operation are at $z > 0$ and they are the first three $\eta$ stations. The first BML station starts at $z = 0.4\ m$, instead of the first BOL station starting at $z = 0.6\ m$, and the third $\eta$ station ends at $z = 5.2\ m$. The $x$ limits are $x = -1.7\ m$ and $x = 1.7\ m$ for the BML stations, and $x = -2.4\ m$ and $x = 2.4\ m$ for the BOL stations. The BML station is centred at $y = -7\ m$ (distance from the interaction point). The BOL station centre is at $y = -9.8\ m$.

Each RPC chamber, as it is shown in figure 6.6, consists of two layers of RPC detectors, distinguished as "Gas Gap 1", the plane at smaller distance from the interaction point, and "Gas Gap 2',' the other one. In sector 13 four gas volumes

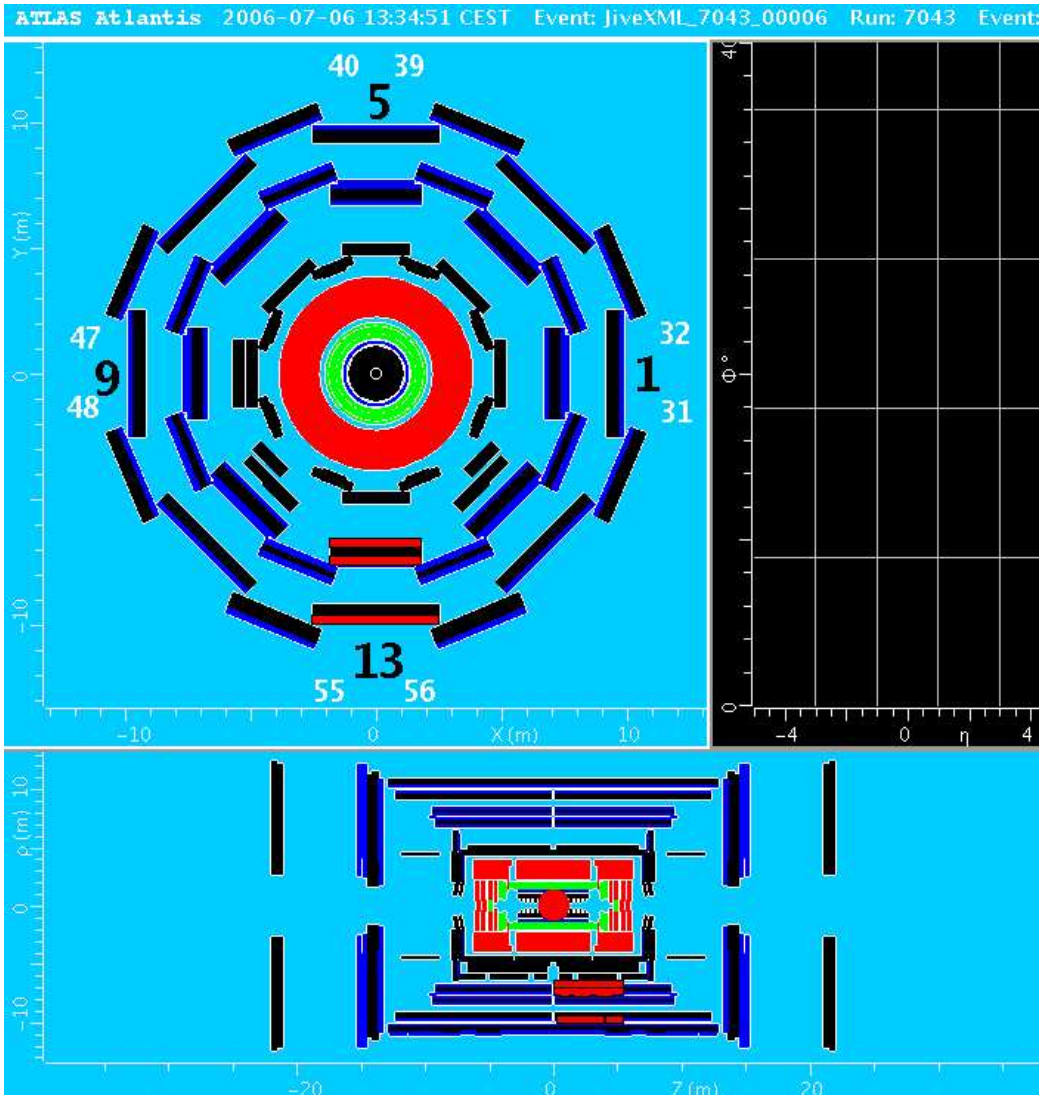


Figure 6.4: Scheme of the ATLAS barrel. In the $\varphi$ view (up) the barrel is segmented in 16 Muon Spectrometer sectors and 64 LVL-1 trigger sectors (32 at $\eta < 0$ and 32 at $\eta > 0$). The black and the white numbers indicate the spectrometer and the trigger sectors at $z > 0$ respectively. In the $\eta$ view (down) the barrel is segmented in 12 muon projective towers (or $\eta$ stations), 6 at $\eta < 0$ and 6 at $\eta > 0$. The RPCs in operation are emphasized in red (muon sector 13: $\eta$ stations 1, 2 and 3 at $\eta > 0$, trigger sectors 55 and 56).

Figure 6.5: Photo of a barrel middle muon station: two RPC are assembled with a MDT, the drift tubes are visible between the RPCs. The boxes mounted on the RPC contain the LVL-1 trigger electronics.

form a RPC layer. The two gas volumes at the same $z$ coordinate are assembled together in the same mechanical structure (see chapter 2), and they form a "Doublet-Z". The two gas volumes at the same $x$ coordinate form a "Doublet-Phi" (see figure 6.6). Five parameters identify a single RPC gas volume in the sector 13: the $\eta$ station number, the name of the RPC chamber ("BML Confirm", "BML Pivot" and "BOL Confirm"), the Doublet-Z (DZ) number, the Doublet-Phi (DPhi) number and the gas gap number.

Each gas volume is read-out by two orthogonal strip panels, one in the $\eta$ view (along $z$) and the other in the $\varphi$ view (along $x$). In the sector 13, the first three BOL stations have $\eta$ panels with 24 strips, as the first $\eta$ BML station. In the second and third BML stations, instead, $\eta$ panels count 32 strips. The $\varphi$ strips are 64 in the BML stations and 80 in the BOL stations.

Five parameters as well identify a RPC strip panel within a muon tower: the name of the RPC chamber (BML Confirm, BML Pivot and BOL Confirm), the Doublet-Z (DZ) number, the Doublet-Phi (DPhi) number, the gas gap number and the view ($\eta$ or $\varphi$). Considering all the possible combination the RPC strip panels are numbered from 0 to 47, starting from the $\eta$ panel of the first gap located in the

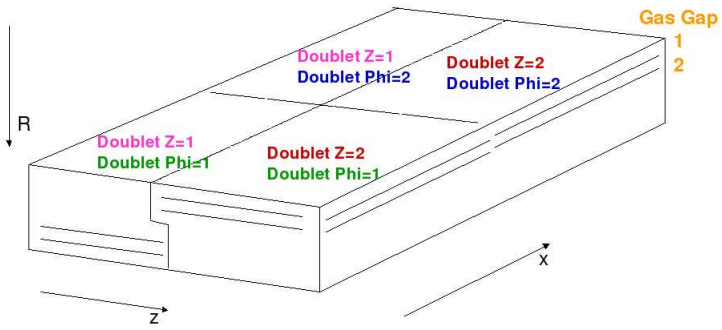


Figure 6.6: Scheme of an ATLAS RPC chamber in sector 13.

Doublet-Z 1 and in the Doublet-Phi 1 of the BML Confirm.

The Muon Spectrometer sector 13 at $\eta > 0$ is divided in two trigger sector: trigger sector 55, that is located at $x < 0$, and trigger sector 56 (see figure 6.4) at $x > 0$. The trigger sectors are also segmented in trigger towers as the muon sectors, so each muon tower is constituted of two trigger towers. As described in chapter 4, in a muon trigger tower a low-$p_T$ trigger Pad and a high-$p_T$ trigger Pad collect the trigger results by eight Coincidence Matrices (CM). Four CMs, two for the $\eta$ view and two for the $\varphi$ view, are mounted on the BML station and they are used for the low-$p_T$ trigger, and four CMs are mounted on the BOL station for the high-$p_T$ trigger. A schematic design of the six operative trigger towers is shown in figure 6.7. The intersection of a $\eta$-CM and a $\varphi$-CM within a Pad gives a RoI (Region Of Interest). On the confirm planes close RoIs are in overlap, in order to select also inclined muon tracks. The overlaps are between RoIs of the same muon tower, but also between the nearby towers. For this purpose some channels from confirm stations are split and read-out in more than one CM.

### 6.1.1 The RPC set-up in the ATLAS cavern

During the cosmic ray test the three muon towers were equipped with temporary gas and power services, because the final ones were not yet available.

The gas system provided the RPCs with the standard mixture ($C_2H_2F_4$:94.7%, $C_4H_{10}$:5%, $SF_6$:0.3%) by means of temporary gas tubes. The gas circuit was open-flow; no close recirculation loop or gas purification were yet in place.

The power system used in the test was an industrially produced standard system (CAEN). Each high voltage (HV) channel supplied 12 gas volumes belonging to the same layer of the three $\eta$ stations, according to the final scheme. Low volt-

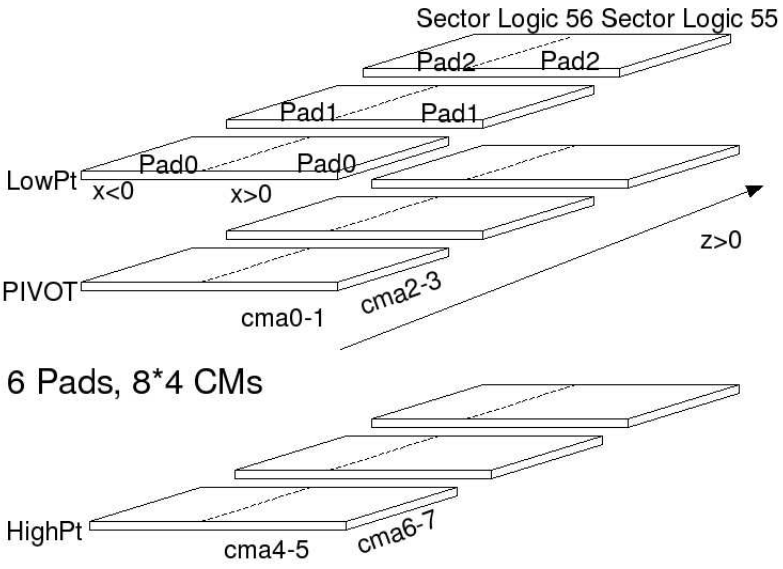


Figure 6.7: Schematic design of the six trigger towers in operation of the muon sector 13.

age (LV) for Font End (FE) boards was supplied separately for each RPC layer.

The DAC modules, which are foreseen in the final system to set the FE electronics threshold (Vth) were not available and standard LV PS were used. The Vth setting on the FE boards was organized on a RPC layer, coupling all $\eta$ read-out panels of the three $\eta$ stations. A similar distribution system was used for the $\varphi$ read-out panels.

A provisional Detector Control System (DCS), using the same CAEN module, was used to control, as in the final system, the following parameters:

- the environment parameters: atmospheric pressure, temperature and relative humidity. No HV correction was applied on the RPC gas volumes for temperature and pressure changes, because to the final DCS configuration was not yet available;

- all the power system parameters, in particular the HV circuit currents for each gas gap;

- the current absorbed by each LV channel;

- the input gas pressure of the RPC gas volume. It was able to switch the HV channel off in case of emergency, to avoid detector damages.

Finally the CAEN module was also used for the power supply of the LVL-1 trigger system, with a channel assigned to each Pad.

### 6.1.2 The data acquisition

In the muon trigger system a $t_0$ time for each 16 channel group can be fixed to set all detector outputs in time, in order to ensure a time coincidence within $\sim 3\ ns$ (which is $1/8$ of the LHC bunch-crossing range).

The trigger system provides muon selection during the ATLAS commissioning phase with cosmic rays in the cavern. During the preliminary studies in summer 2006 the trigger configuration was not yet optimized for cosmic muons. In particular during this test the $\eta$ and $\varphi$ views of the same muon trigger tower had to be still calibrated in time, in order to estimate the different cable delays and to set the correct time alignment between the two views and the three RPC planes. Therefore for large part of the data acquisition, trigger was provided only by the $\varphi$ view with the fully open Coincidence Window configuration (see chapter 5). A time window of 25 $ns$ (larger than the standard one) was set for the coincidence and a majority of $2/4$ in the two middle RPC doublets (one hit per doublet) was requested.

When a coincidence was found by the trigger, data in a time window of 200 $ns$ large (corresponding to 8 LHC bunch-crossing) were acquired, reading all the subdetectors out. The acquisition time window had to be large enough to collect all event hits out of time alignment. No more than one trigger was accepted within 25 $ns$ (the LHC bunch-crossing range).

## 6.2 First results in the ATLAS cavern

In figure 6.8 an event display shows one of the first cosmic muons crossing the muon stations of the sector 13 ($\eta$ view).

Data collected in August 2006 (run 1036) have been analyzed in the ATHENA framework (release 12.2.0) and $22 \cdot 10^3$ events were processed. During the run storage the RPC gas volumes were supplied with 9.6 $kV$ and the $\eta$ and $\varphi$ electronics thresholds on the FE boards were set to 1.0 $V$ for all the chambers.

In figure 6.9 and 6.10 the hit profile in the $\eta$ view and $\varphi$ view respectively are shown for the three operative stations of the sector 13. The PX14 shaft, centred at $x = 1.7\ m$ and $z = 13.5\ m$ and with a diameter of 18 $m$, influences the cosmic flux in the ATLAS cavern, as already seen in the simulation (see section 5.3). In

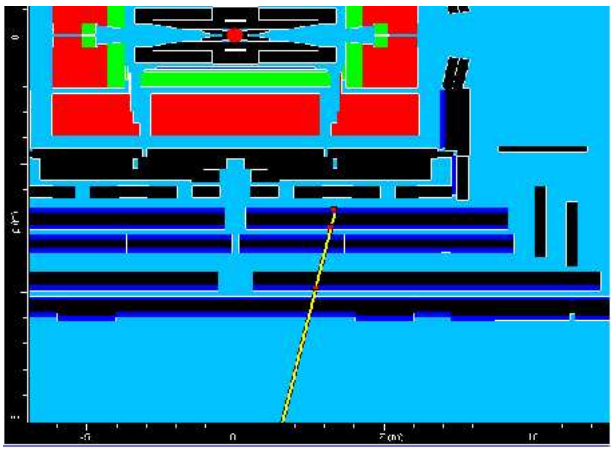

Figure 6.8: A muon track produces hits in the RPC stations ($\eta$ view of the half bottom ATLAS barrel). The blue lines are the RPC stations.

the $\varphi$ view the hit profile is not flat over the chamber, due to the shaft not centred respect to the sector 13 position. The profile in the $\eta$ view (figure 6.9) increases with z, that means station are getting closer to the region under the shaft.

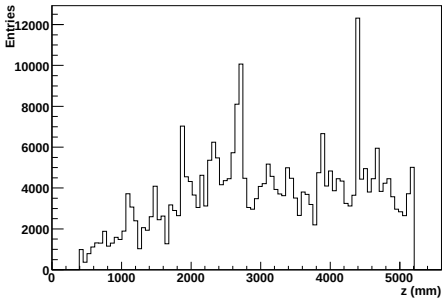


Figure 6.9: $\eta$ RPC hit distribution for the three stations in the sector 13. The cosmic muon flux increases with z, due to the presence of the shaft, as expected by simulation (see section 5.3).

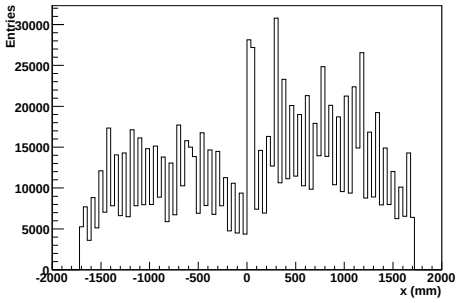


Figure 6.10: $\varphi$ RPC hit distribution. The profile reproduces the shaft position, which is not centered with respect to the sector 13.

The hit profile and the hit time distribution of a gas volume for the $\varphi$ and $\eta$ views are shown respectively in figure 6.11 and 6.12.

The $\varphi$ hit time distribution is almost flat in one single bunch-crossing range (25-50 $ns$), as expected for a pivot station, because it is the detector activating the trigger. For the $\eta$ view the hit time distribution is a little larger and split over two

bunch-crossing ranges (1-25 and 25-50 $ns$), showing that the two views are not perfectly aligned in time.

The hit multiplicity for each single physics hit can exceed 1, because of the after pulses of the Front End electronics (see figure 6.13). In the standard trigger read-out instead, a dead time with a maximum value of 100 $ns$ will be set on each channel (a dead time of 60 $ns$ is already sufficient to avoid hits due to after pulses). In the present data there was no applied dead time.

In figure 6.14 an event with a signal and an after pulse is shown. A signal is induced on the strips 62 and 63 at $t = 53$ $ns$ and a after pulse is visible on both strips after about 20 $ns$. The two hits in each strip can not be produced by two different cosmic muons, considering that with a $\sim 2$ $Hz/m^2$ cosmic rate, estimated by simulation, two events within 20 $ns$ on the same read-out strip have very low probability. To avoid the double counting caused by the after pulse hits the dead time is introduced (off-line) in the analysis by the cluster algorithm.

Moreover in the confirm layers a physics hit is counted more times, if the muon crosses a region where two (or many) CMs overlap. In fact according to the trigger logic, two close RoIs intersect on the confirm layers to allow trigger of inclined muon tracks crossing two trigger towers. The RoI overlap is performed by splitting a RPC strip signal in more than one CM (the splitting is only for signal from strips of the confirm layers; strips of the pivot panels are read out only by the CM, which defines the RoI). At the moment the hit splitting is not removed by the analysis, therefore all the CM read-out data are considered in the hit distributions.

Furthermore due to the CMs not yet aligned in time, a physical hit read out by more than one CM is collected more times and with different time reference. The dead time introduced in the cluster algorithm allows also to reduce the hit multiplicity due to the signal splitting.

### 6.2.1 Cluster algorithm

To study the RPC performances and to check the RPC efficiency, a cluster algorithm has been implemented. The algorithm is based on the following rules:

- For each event a cluster is defined as a group of adjacent strips hit at the same time or within 15 $ns$. This time range is estimated as the maximum time for the signal induction/cross talk.

- Not to count hits due to after pulses, only the first hit of each strip is considered by the cluster algorithm. This choice corresponds to set a maximum

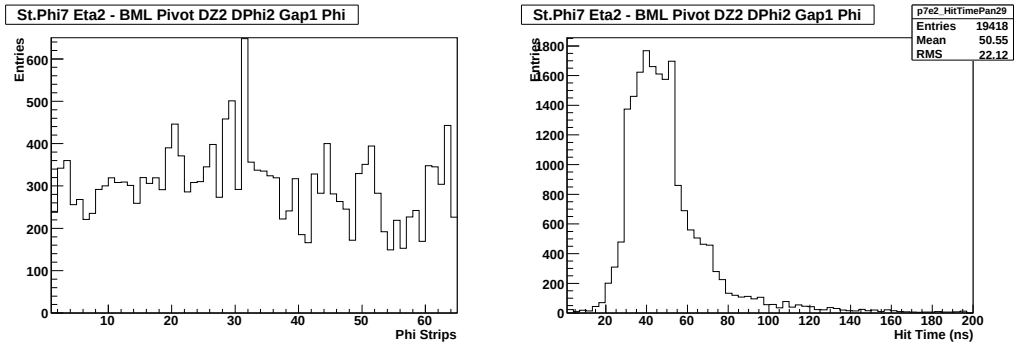


Figure 6.11: Hit strip distribution (on the left) and hit time distribution (on the right) for cosmic muons on a $\varphi$ read-out panel. The hit multiplicity for each single physics hit can exceed 1, because of the after pulses of the FE electronics. The hits are concentrated in a single bunch-crossing range (25-50 $ns$), as expected for a pivot station, which is the detector activating the trigger.

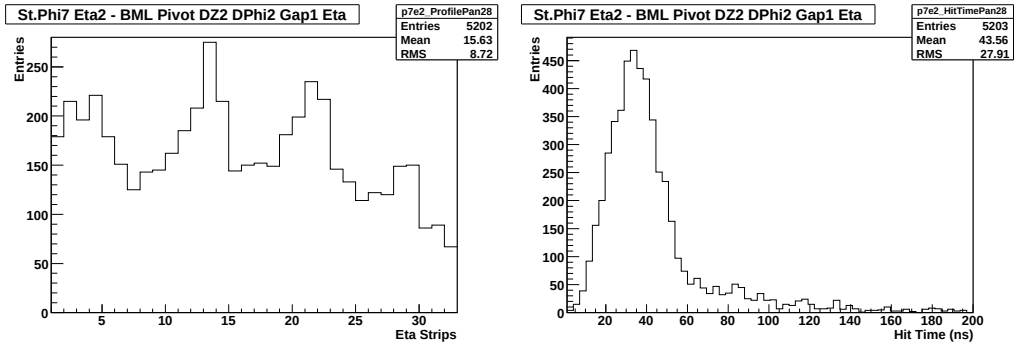


Figure 6.12: Hit strip distribution (on the left) and hit time distribution (on the right) for cosmic muons on a $\eta$ read-out panel. The hit multiplicity for each single physics hit can exceed 1, because of the after pulses of the FE electronics. The times associated to the hits scatter over two bunch-crossing ranges (1-25 and 25-50 $ns$). The comparison with the time distribution which is above shows that the two views are not perfectly aligned in time.

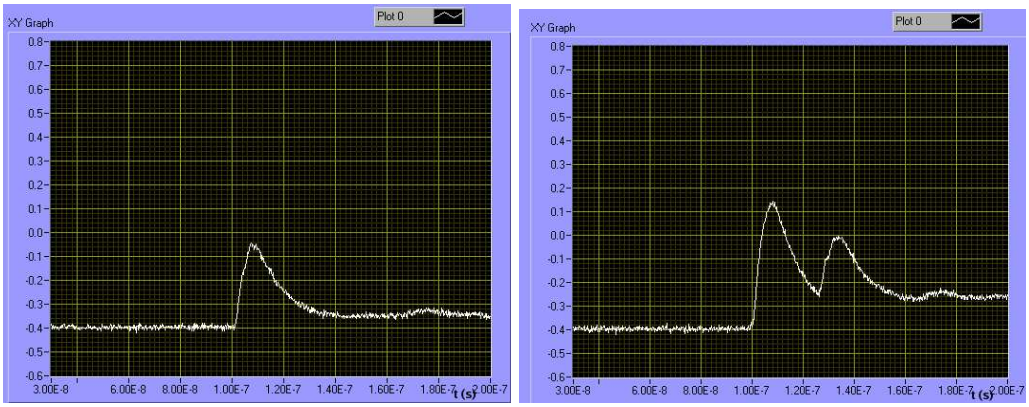


Figure 6.13: A Front End output signal is shown for a RPC working in avalanche mode (on the left). On the right side an after pulse is visible $\sim 20$ *ns* far from the first readout signal (laboratory test result, not correlated with the present test).

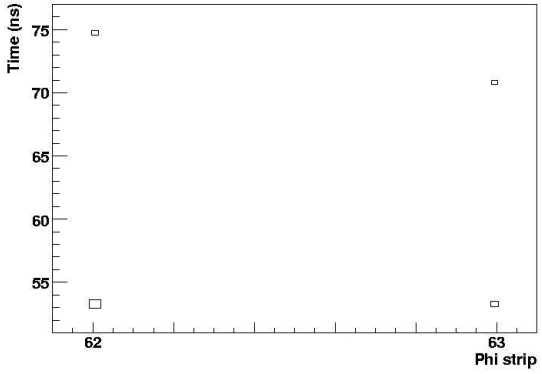


Figure 6.14: A cosmic ray test event. Two synchronous signals are induced on contiguous strips at $t = 53$ *ns*. An after pulse after about 20 *ns* is also observed in both strips, with a time misalignment of 1 time bin (3.125 *ns*). No dead time is set on the read-out channel.

dead time of 200 *ns* (the data acquisition time window) on each strip. Moreover the introduced dead time reduces to 1 the hit multiplicity due to the signal splitting.

- The first hit in time fixes the cluster time.
- The number of the strips forming the cluster defines the cluster size; cluster size is 1, if the signal is induced on one strip only.
- The cluster centre is given by the geometrical centre of all the strips belonging to the same cluster.
- In a read-out panel more than one cluster can occur.

The cluster algorithm is particularly needed for complex events, like the one shown in figure 6.15. An event with many fired strips and many hits in time in the strip is shown. After the cluster algorithm is applied, after pulses and hit duplications due to the overlap regions are removed. The large hit multiplicity is reduced to only eight clusters (red box): one with size 12, one with size 2 and the others with size 1. The time range of the event is now confined in less than $\sim 40$ *ns*.

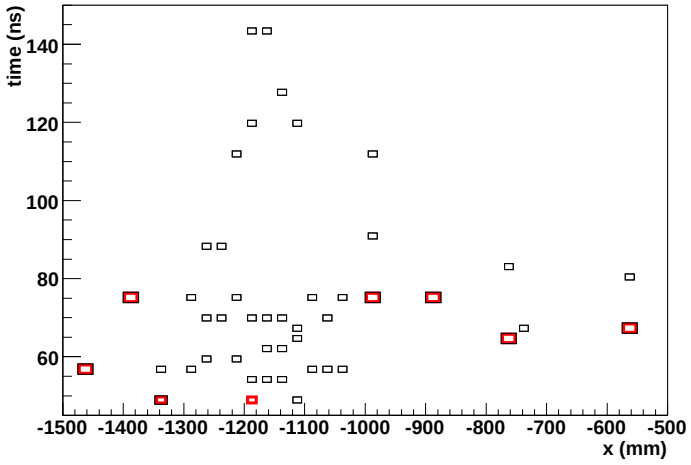


Figure 6.15: A peculiar, complex event with many fired strips and many hits in time in the strips. The large hit multiplicity is reduced by the cluster algorithm to only eight clusters (red box): one with size 12, one with size 2 and the others with size 1. The event is now confined within $\sim 40$ *ns*.

It has to be noted that the event shown in figure 6.15 is a peculiar event with a very large hit multiplicity. For the present data in a strip panel the average number of clusters per event is 1.2.

The average cluster size is strictly dependent on the set RPC working point. At the conditions set for the analyzed run (High Voltage 9.6 $kV$ and electronics threshold 1.0 $V$) the average cluster size is $\sim$ 1.5. The cluster size distributions for a $\eta$ read-out panel (left side) and for a $\varphi$ read-out panel (right side) are shown in figure 6.16.

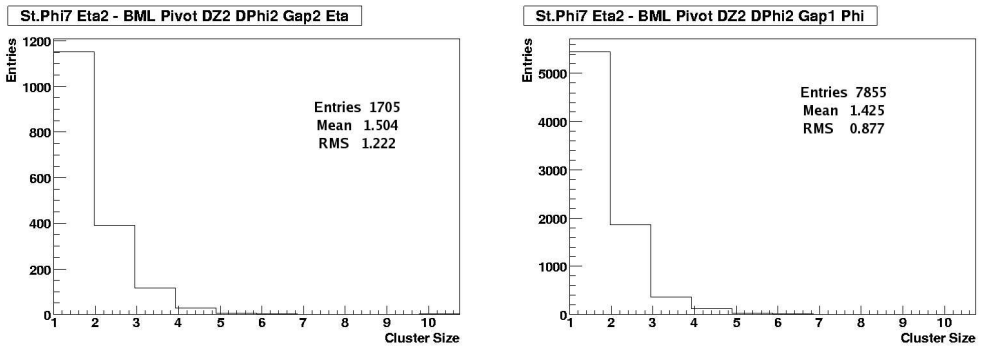


Figure 6.16: Cluster size distribution (working point: $HV$ = 9.6 $kV$ and $Vth$ = 1.0 $V$) for an $\eta$ read-out panel is on the left and for a $\varphi$ read-out panel is on the right.

To evaluate the effect of introducing the cluster algorithm, hit distributions can be compared with cluster distributions. In figure 6.17 the hit time distribution (black line) is compared with the cluster time distribution (red line). The time distributions on the left are for an $\eta$ panel and on the right are for a $\varphi$ panel. The cluster time distribution is peaked at the time value different few $ns$ from the hit time peak. But due to the dead time introduced on the strip, the RMS of the cluster time distribution is smaller of about 7.5 $ns$ with respect to the hit time distribution, in both $\eta$ and $\varphi$ views.

Then the hit distribution (black line) is compared with the cluster distribution (red line) in figure 6.18. The cluster multiplicity is reduced with respect to the hit multiplicity. By using the cluster algorithm, the after pulse contamination in the hit distribution of the pivot layers (which have not overlapped regions) can be calculated comparing the number of hits with the number of clusters, weighted for their average cluster size. The after pulse contamination is about $\sim$ 1.3, hence the real hit multiplicity has to be reduced of about 23%. It has to be noted that

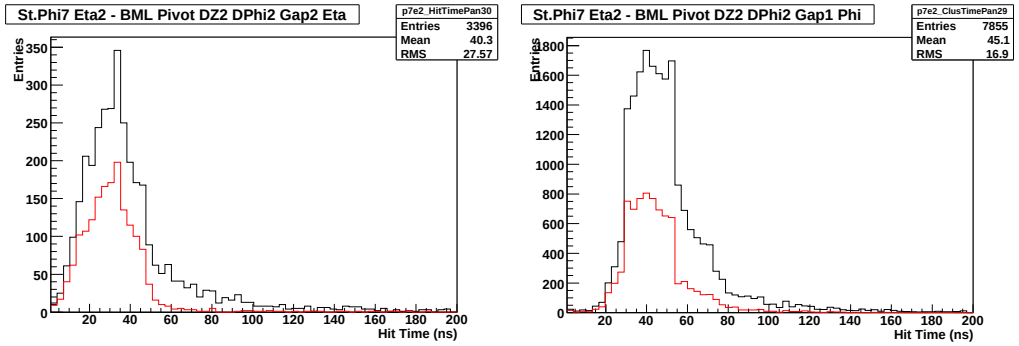


Figure 6.17: Cluster time distribution (red line) is compared with the original hit time distribution (black line). They are peaked at the same time value, but the RMS of the cluster time distribution is smaller of about 7.5 *ns*. An $\eta$ read-out panel is on the left side and a $\varphi$ read-out panel is on the right side.

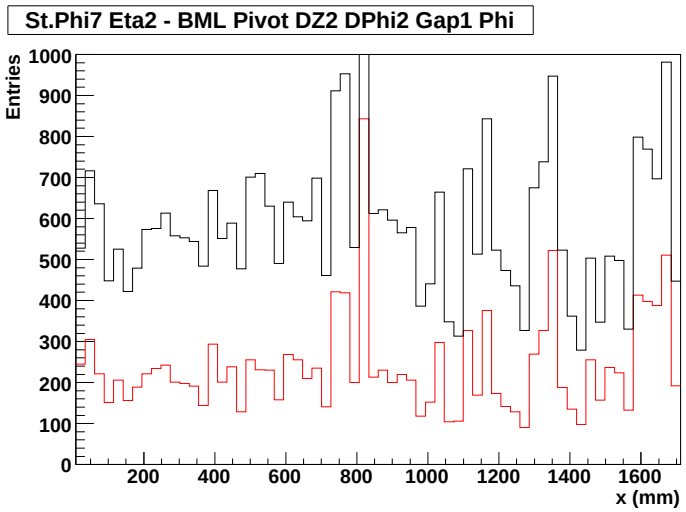


Figure 6.18: Cluster distribution (red line) is compared with the original hit distribution (black line).

these results are preliminary, this is the first data taken in the ATLAS cavern and the detector working point was not optimized.

## 6.3 Efficiency algorithm

The MDT chambers assembled with the RPCs are the subdetectors dedicated to the muon track reconstruction in the $\eta$ (bending) view, as described in chapter 1. An algorithm, developed within the ATHENA framework and called MOORE [34], provides the muon track reconstruction using the MDT data.

During the cosmic test, the MDTs of the three stations in sector 13 were operative (high voltage at 3080 $V$ and electronics threshold at $-40$ $mV$). Therefore in the $\eta$ view, the RPC cluster positions can be compared with the muon tracks, in order to provide a further check in the RPC detection efficiency measurement.

For this purpose a dedicated algorithm, the `RpcPerformanceNtuple`, has been introduced in the ATHENA framework. It acts as follows:

- The track segment reconstructed by two MDT multilayers in each muon station is extrapolated on the RPC gaps. The expected hit $\eta$ strips are computed according to the extrapolation.
- In order to check if the track is consistent with the event trigger, two conditions for each gap under test have to be satisfied:
  1. for the efficiency study of the gas gap 1, a hit in the $\eta$ view is requested in gap 2, and vice versa;
  2. moreover a $\varphi$ hit in the same layer of the $\eta$ hit is requested.
- Since each drift tube of the MDT chamber covers two RPC gas volumes along $x$, MDTs can not distinguish between the two $\eta$ RPC panels of the same unit, identified by Doublet-Phi 1 or 2 in figure 6.6. If one of the two Doublet-Phi verifies the requests described in the previous item, the expected $\eta$ strip is assigned to this doublet; otherwise the event is not considered for the RPC efficiency evaluation.

During the cosmic test RPCs worked as trigger detectors and second coordination providers, as in the standard ATLAS operation. To study the efficiency on the $\eta$ view, only data acquired with RPC trigger given by coincidences of two $\varphi$ BML doublets in each trigger tower were selected. According to the trigger logic, a $\varphi$ hit on one of the two layers within each gap doublet was sufficient for the trigger.

Therefore the set of the algorithm conditions, described above, selects an unbiased sample of events for the detection efficiency measurement. The RPC efficiency estimated in this way is a combination of two contributes: the gas volume efficiency and the $\eta$ FE efficiency.

The profile of the muon MDT segment extrapolation on a RPC panel is shown in figure 6.19.

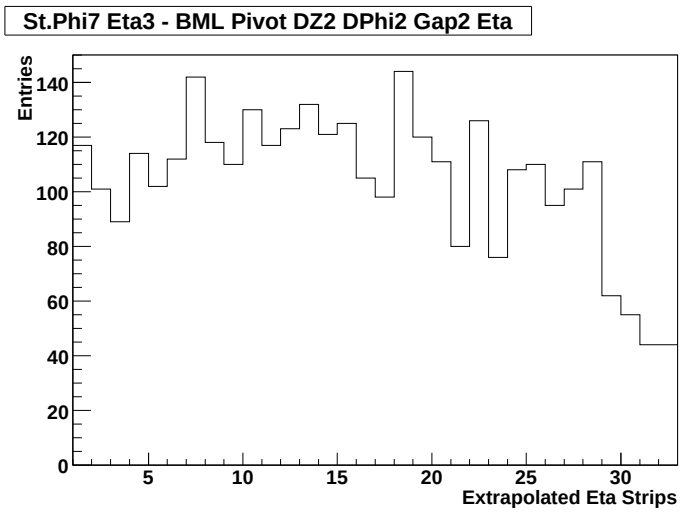


Figure 6.19: MDT track extrapolation profile on a RPC plane.

In figure 6.20 a muon crossing the muon stations of the sector 13 is shown. The RPC cluster centres are shown both in $\eta$ and $\varphi$ view. In the $\eta$ view the points extrapolated on the RPC gas volumes by the MDT reconstructed track are also shown (red triangles). In a large number of the observed events the MDT extrapolation is consistent with the cluster centre.

Moreover the correlation between the RPC cluster centres and the extrapolated hits on a $\eta$ strip panel is shown in figure 6.21. The residual is the difference between the cluster $z$ coordinate and the muon segment extrapolation on the RPC plane. The residual distribution is shown in figure 6.22. An $\eta$ strip is $\sim$ 30 *mm* large.

A strip/panel is considered efficient if there is a cluster having the centre within 60 *mm* from the extrapolated MDT track segment. The halo of 60 *mm* (about the width of two strips) is sufficient to consider for the efficiency all the clusters correlated with the muon tracks as shown in figure 6.23, where the panel efficiency measured for different halo values is plotted.

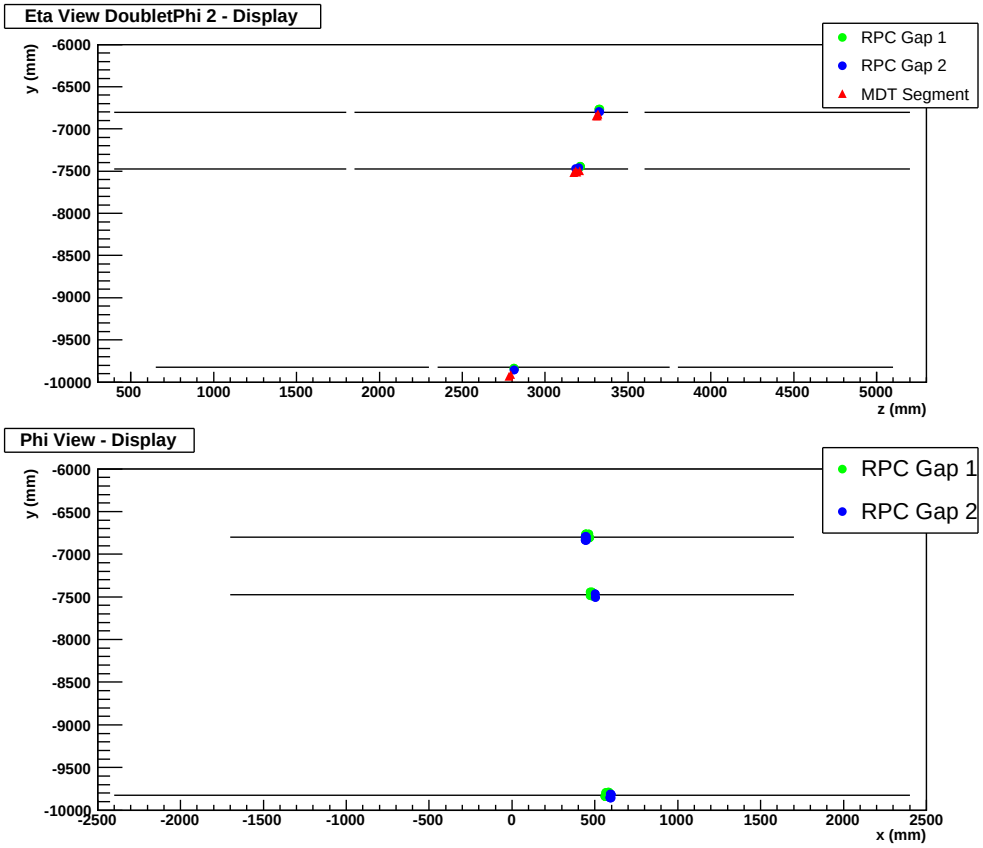


Figure 6.20: Event display. The extrapolation by MDT muon segments are shown together with the RPC fired strips. The track is visible on the three RPC stations both in $\eta$ view (up) and $\varphi$ view (down).

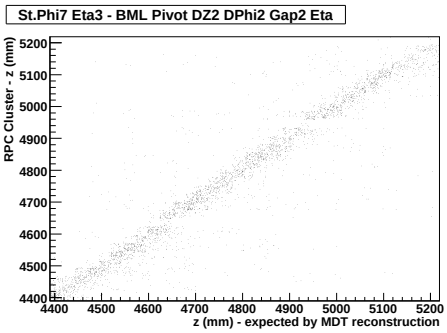


Figure 6.21: Correlation between the RPC cluster centre and the extrapolation of the muon tracks reconstructed by the MDT trackers.

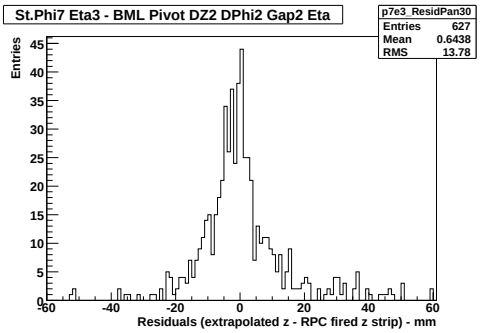


Figure 6.22: Distribution of the distances between the RPC cluster centres and the extrapolated MDT track segments (an $\eta$ strip is $\sim 30\ mm$ large).

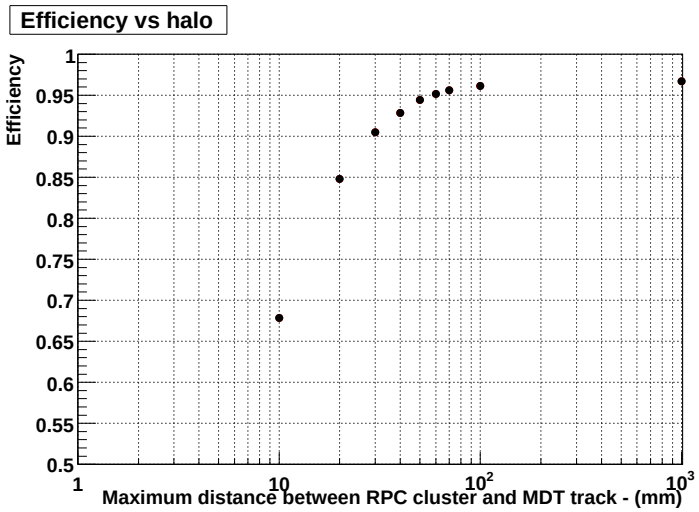


Figure 6.23: Panel efficiency versus halo plot. The halo fixes the limit distance of the cluster centre from the MDT track segment, to define that cluster as efficient. Above $\sim 60$ *mm* the slope can be considered negligible.

The efficiency for each strip of a read-out panel is shown in figure 6.24. The efficiency of the selected read-out panel is $0.952 \pm 0.007$. The error on the efficiency is estimated assuming the Binomial distribution. Therefore if $N$ is the number of events with reconstructed tracks and $n$ is the number of events with efficient clusters, the efficiency is defined as

$$\varepsilon = \frac{n}{N}$$

and the error estimate is given by

$$\delta\varepsilon = \sqrt{\frac{\varepsilon(1-\varepsilon)}{N}},$$

taking into account that $\varepsilon$ and $\delta\varepsilon$ are not correctly evaluated if the number of inefficient events is very small ($\bar{n} = N - n < 3$ is chosen for simplicity), due to the limited statistics of the acquired events. In this case for the inefficient events the Poisson distribution is assumed and a lower limit for the efficiency is fixed, as illustrated in table 6.1.

It has to be stressed that the RPC working point was not optimized. The applied high voltage is 9.6 $kV$, which, taking into account the different normalization due to the environment conditions in the ATLAS cavern, corresponds to an applied high voltage of 9.9 $kV$ at the cosmic test stand in Rome (as described in

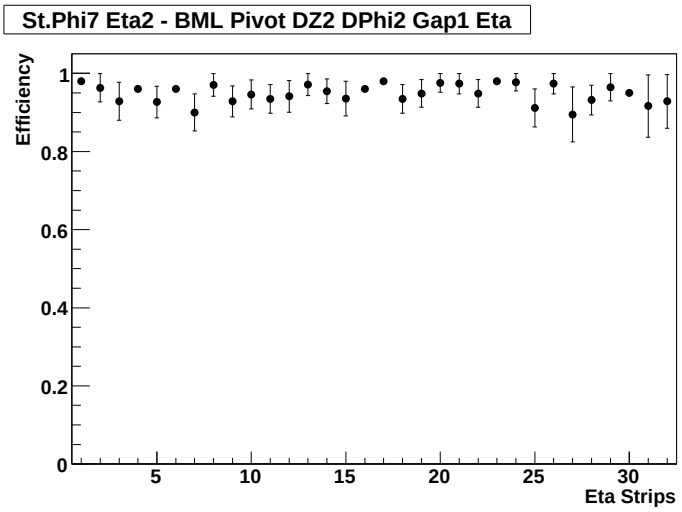


Figure 6.24: RPC strip efficiency. The error bars are calculated assuming that the efficient event distribution follows the Binomial statistics. The points without error bars are relative to the cases with a number of inefficient events $< 3$ and indicate the efficiency lower limit values estimated with the Poisson statistics for a confidence level around 90% and presented in table 6.1. The efficiency of this read-out panel is $0.952 \pm 0.007$.

| $\bar{n}$ | $CL$ | Efficiency |
|---|---|---|
| 0 | 87% | $\geq 98\%$ |
| 1 | 90% | $\geq 96\%$ |
| 2 | 89% | $\geq 95\%$ |

Table 6.1: If the number of inefficient events is $\bar{n} = N - n < 3$, a confidence level ($CL$) is chosen and the mean value ($<\bar{n}>$) producing a Poisson probability of $\bar{n}$ inefficient events equal to $(1 - CL)$ is calculated. Then a lower limit for the efficiency is fixed by $(N - <\bar{n}>)/N$.

chapter 3). With an high voltage of 9.9 $kV$ the RPC is not yet fully efficient (see section 3.1.4).

## 6.4 An ATLAS muon tower

In this section the analysis results for one (the second) $\eta$ muon tower of the sector 13 are summarized. A muon tower consists of three RPC stations and each RPC station has eight $\eta$ and eight $\varphi$ strip panels. The $\eta$ strips are 32 for each BML panel and 24 for the BOL panels; and the $\varphi$ strips are 64 for each BML panel and 80 for the BOL panels. Within a muon tower the RPC strip panels are numbered from 0 to 47, starting from the $\eta$ panel of the first gap located in the Doublet-Z 1 and in the Doublet-Phi 1 of the BML Confirm.

The average number of clusters per event is 1.25 for the $\eta$ strip panels and 1.21 for $\varphi$ strip panels. These results for each panel are presented in figure 6.25. For the $\eta$ view the average number of clusters per event is compared with the same quantity for only the efficient clusters, that have an associated MDT track with the criteria described before. The comparison shows that in this tower the BML stations have more noise than the BOL station (in the $\eta$ view).

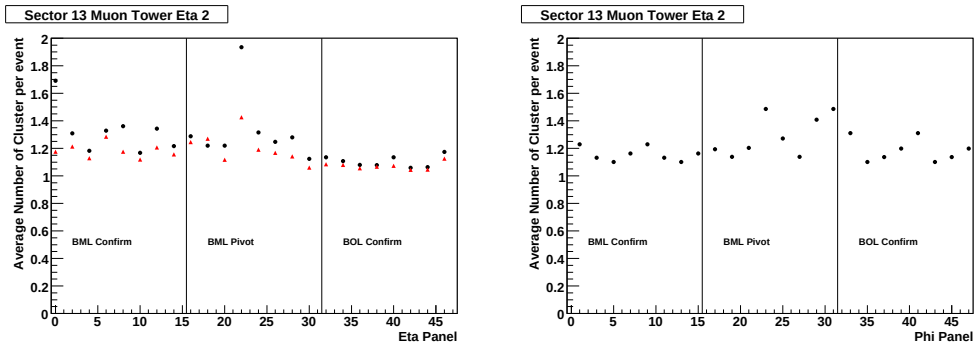


Figure 6.25: Average number of clusters per event for each RPC plane of the second $\eta$ muon tower in the sector 13 for $\eta$ view (left) and $\varphi$ view (right). On the left side both the efficient clusters (red triangles) and all the clusters (black points) are considered. The comparison shows that in this tower the BML stations have more noise than the BOL station (see the layer 22 of the $\eta$ view with $\sim$ 2 clusters per event and only 70% of clusters are efficient). The two BOL $\eta$ planes are already optimized for the detector noise, almost all the clusters are efficient; for the $\varphi$ view some optimization has still to be done.

The average cluster size for each panel is shown in figure 6.26 for $\eta$ view (left) and $\varphi$ view (right). In the $\eta$ view the average size of the efficient clusters is also shown (red triangles). The BML $\eta$ planes show a larger cluster size with respect to the other panels, which have average cluster size of 1.5.

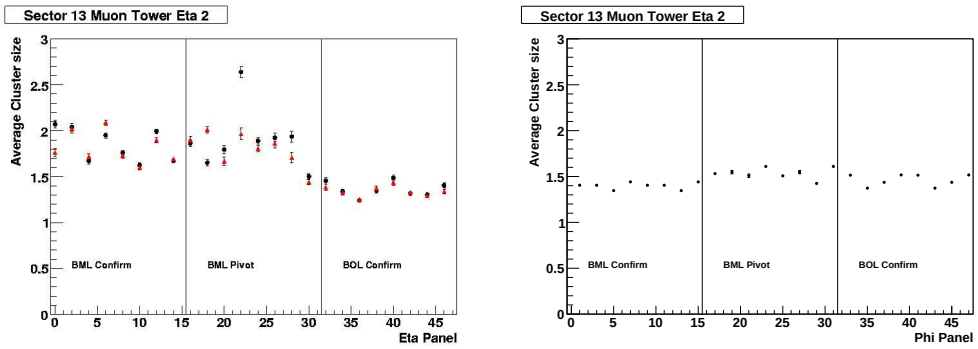


Figure 6.26: Average cluster size for each RPC plane of the second $\eta$ muon tower in the sector 13 for $\eta$ view (left) and $\varphi$ view (right). On the left both only the efficient clusters (red triangles) and all the clusters (black points) are considered.

For each panel the efficiency is shown in figure 6.27. All the panels have efficiency over 85%, with a high voltage applied to the gas volumes of 9.6 $kV$, which corresponds for the ATLAS RPCs to an efficiency value under the plateau value ($\sim$ 98%). The measured panel efficiency is 92.8% on average.

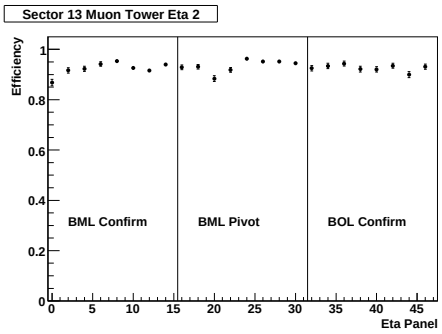


Figure 6.27: $\eta$ strip panel efficiency for the second $\eta$ muon tower in sector 13.

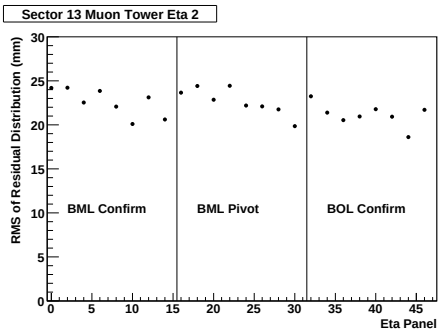


Figure 6.28: Residual RMS of the RPC clusters with respect of the MDT muon tracks for the second $\eta$ muon tower in sector 13. The RMS is 22 $mm$ on average.

In figure 6.28 the RMS of the cluster residual distribution for each $\eta$ panel is shown.

## 6.5 Check of the time alignment

The main goal of the cosmic ray tests in the cavern is the detector calibration. At the moment of the present test, the trigger configuration was not yet optimized for cosmic muons. The muon trigger towers had to be still calibrated, and in particular the two views and the three RPC stations in a muon tower were not aligned in time. A preliminary time alignment was only performed in the $\varphi$ view to ensure a good trigger capability. The Coincidence Matrices (CMs) elaborated the trigger coincidences in both the two views, but only the $\varphi$ view activated the data acquisition.

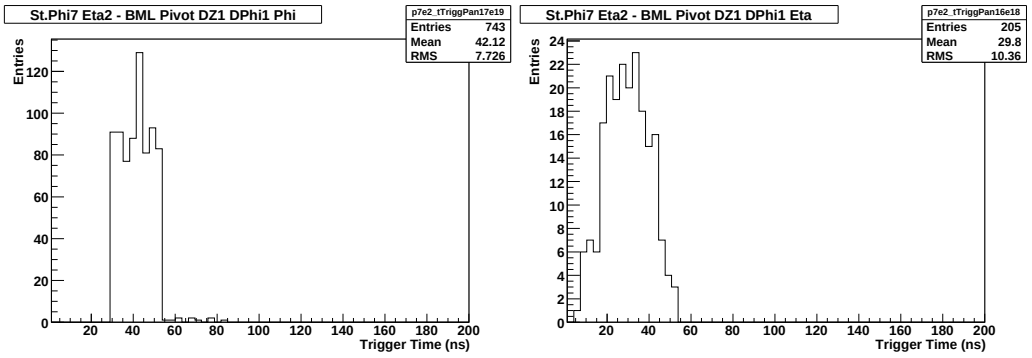


Figure 6.29: Trigger coincidence time distribution of the $\varphi$ view (on the left) and of the $\eta$ view (on the right). The CMs elaborated the trigger coincidences in both the two views, but only the $\varphi$ view activated the data acquisition.

The coincidence time distribution of the pivot layers is shown in figure 6.29 both for $\varphi$ and $\eta$ views. According to the muon trigger system, the pivot layer is the plane fixing the event time with respect to a time window of 25 $ns$ (divided in 8 bins of 3.125 $ns$) provided by a clock emulating the LHC bunch-crossing time range. The $\varphi$ trigger time distribution is almost completely concentrated in the second LHC bunch-crossing time range (between 25 and 50 $ns$), instead of the $\eta$ trigger time distribution, which is larger and split on two time windows.

One of the main consequences of applying the cluster algorithm is that the cluster time distribution has a peak at the same value of the hit time distribution, but the RMS decreases of about 7.5 $ns$ (see section 6.2.1). Therefore, the time

alignment within a muon trigger tower can be evaluated by comparing the average cluster time for each read-out panel. Cluster time distributions for pivot read-out

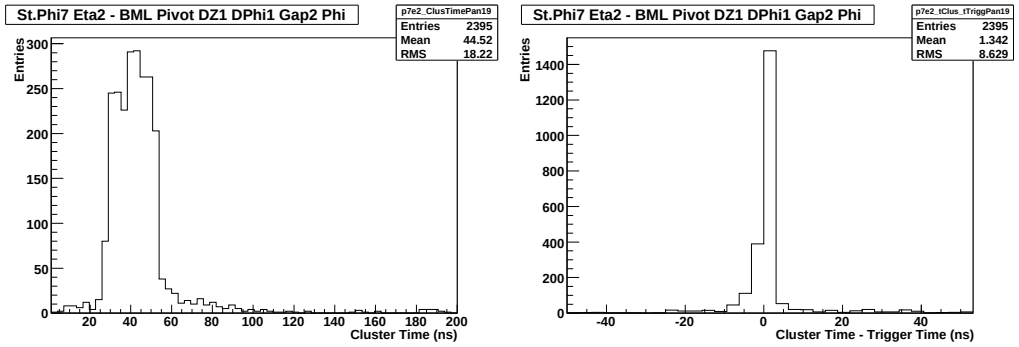


Figure 6.30: Cluster time distribution before (on the left) and after (on the right) subtraction of the trigger time for a $\varphi$ panel.

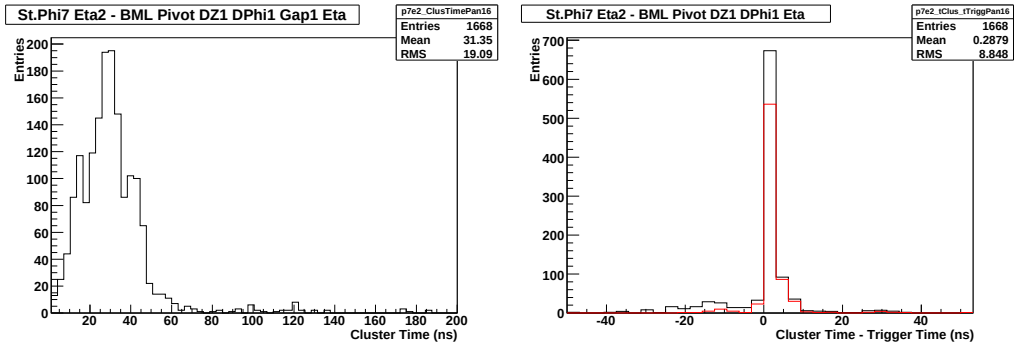


Figure 6.31: Cluster time distribution before (on the left) and after (on the right) subtraction of the trigger time for a $\eta$ panel. The distribution in black refers to all clusters and the one in red to the efficient clusters only. The events out of the sharp peak (on the right) are in large part inefficient.

panels are shown on the left in figures 6.30 and 6.31.

If the trigger time is subtracted from the cluster time event by event (see figures 6.30 and 6.31 on the right), the RMS of the time distribution further considerably decreases, passing from 18 $ns$ for $\varphi$ and 19 $ns$ for $\eta$ to about 9 $ns$. Moreover a further reduction of the RMS is observed for the $\eta$ view for the distribution of the efficient clusters (red line in figure 6.31), which shows substantially lower

tails and a RMS of 5.5 $ns$ (this value has to be compared with the total time jitter given by $\sigma^2_{tot} = \sigma^2_{int} + \sigma^2_{strip}$, where the $\sigma_{int}$ is the intrinsic RPC time resolution of $\sim 1.5\ ns$ and the $\sigma_{strip}$ is the jitter of the time propagation of the signal in the strip, which for a BML $\eta$ strip is about 2.5 $ns$). This is the real cluster time distribution of a strip panel.

Finally the comparison between the red and the black lines in figure 6.31 (right) also shows that the time distribution of the efficient clusters is basically equivalent to the trigger time distribution and the histogram tails are mostly due to inefficient (fake) clusters. The distribution of the efficient clusters only is used to estimate the average cluster time for the $\eta$ view.

In figure 6.32 the average cluster time is shown for the $\varphi$ strip panels of the second $\eta$ tower in trigger sector 56. All the clusters are considered in the time distribution (cluster efficiency can not be estimated with the MDT segments on the $\varphi$ view). The average time is estimated by a Gaussian fit (black triangles). The times are correctly aligned at less than 3 clock time bins (9.375 $ns$).

The average time for each panel obtained by the RPC cluster distribution can be compared with the time estimated by the trigger data. With the trigger data measurements the delay of each RPC station is analyzed by the time distribution of the signals in the CMs on each connector of 16 channels. Therefore for a RPC read-out panel the average cluster time has to be compared with the mean value, obtained by averaging on the time measured in the CMs for each channel group of the strip panel. For channels which are read out by more than one CM (channels belonging to overlapped RoIs), only the time measured by CM mounted on the pivot plane of the same trigger tower is considered.

The comparison in figure 6.32 shows that the values obtained by the cluster time distributions are in agreement with the times measured in the CMs (red stars). On the $\varphi$ view the signals are already been aligned in time, allowing to provide the trigger.

In the $\eta$ view instead, the time alignment has still to be done, both between the RPC stations (BML Confirm, BML Pivot and BOL Confirm) and among the CMs. In figure 6.33 an example of a read-out panel (panel 4 of the $\eta$ station 3) with strips connected to two CMs, which are not aligned in time, is shown. The hit times are plotted as a function of the strip number. The first eight channels (a FE board) are delayed of about 60 $ns$ respect to the others, which instead have similar time distributions. This effect occurs because the channels from 1 to 8 belong to a different RoI respect to the other strips, therefore they are connected to another CM, which has a different time reference.

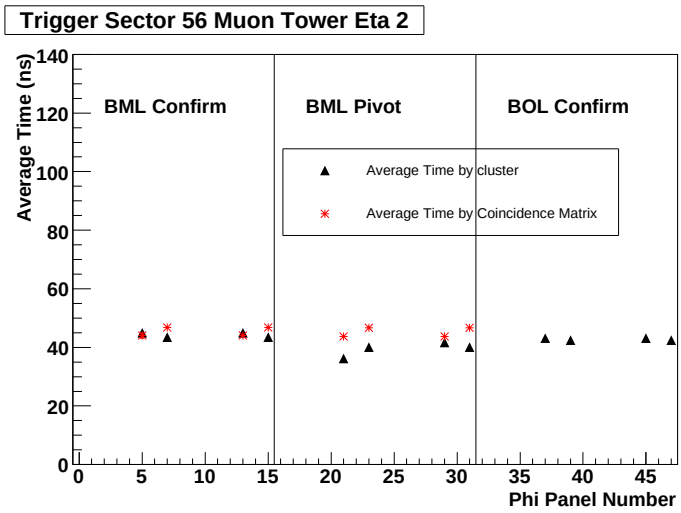


Figure 6.32: Average cluster time for the $\varphi$ strip panels of the second $\eta$ tower in trigger sector 56 (the strip panels are numbered from 0 to 47, starting from the $\eta$ panel of the first gap located in the Doublet-Z 1 and in the Doublet-Phi 1 of the BML Confirm). The average time is estimated by a Gaussian fit (black triangles). The red stars show the average time measured in the Coincidence Matrices (not available for BOLs). The error on the average time is limited by the time resolution (a time bin is 3.125 $ns$ large) and is $3.125/\sqrt{12}$ $ns$ according to the RMS of a uniform distribution.

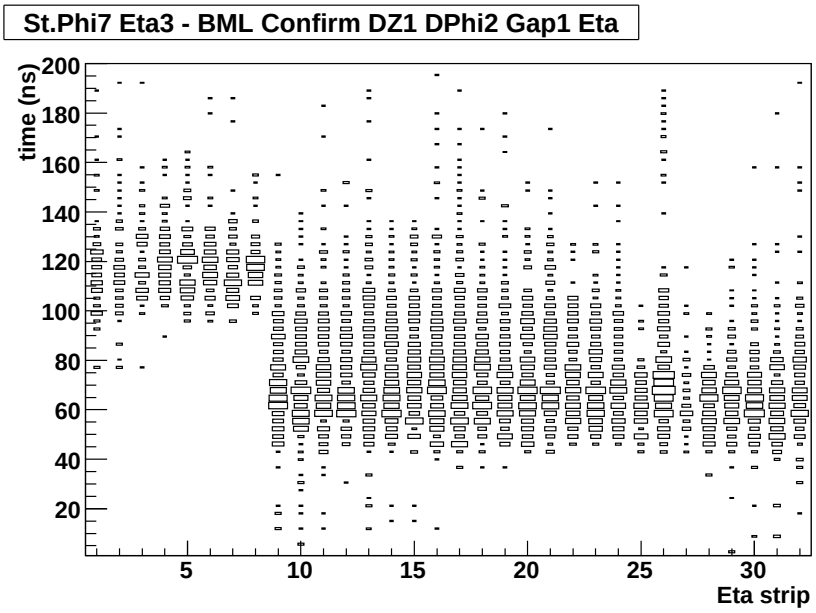


Figure 6.33: Hit time versus the hit strip number for panel 4, $\eta$ station 3. The first eight channels (a FE board) are delayed respect to the others.

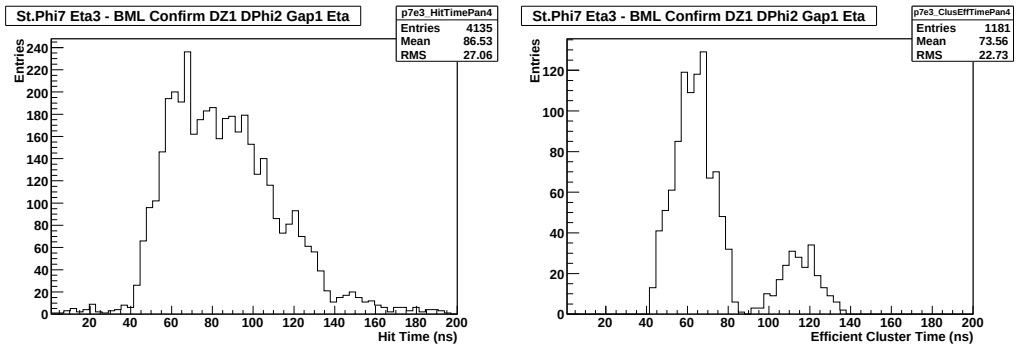


Figure 6.34: Hit time (left) and cluster time (right) distribution for panel 4 $\eta$ station 3. The hit time distribution is the convolution of two contributes, which are visible in the cluster time distribution. The signal of the strips are read-out by two different CMs, which are not aligned in time. A CM with an average time of 115 *ns* is connected with the first eight strips. Another CM read the channels from 9 to 32 and has an average time of 62 *ns*.

The hit time distribution and the cluster time distribution for this panel are shown in figure 6.34. The hit time distribution is the convolution of two different contributes, which are observed in the cluster time distribution. According to the fits shown in figure 6.35, the clusters show a time peak at 62 *ns* for the strips from 9 to 32 and another time peak is at 115 *ns* for the strips from 1 to 8.

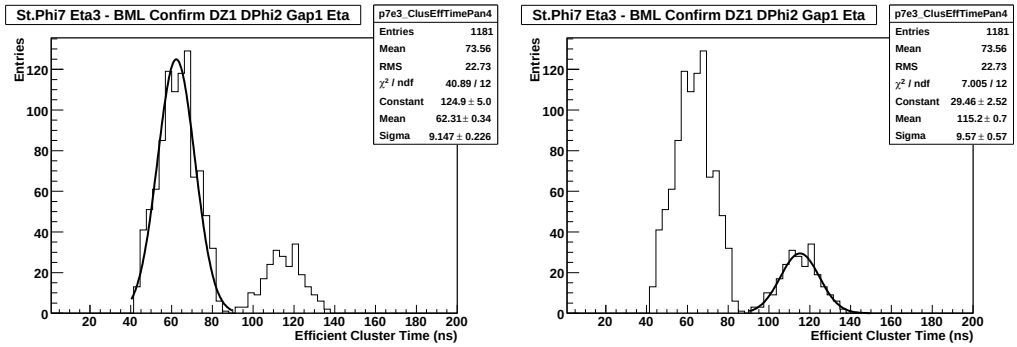


Figure 6.35: Since the strips of the panel 4 $\eta$ station 3 are read-out by two different CMs, which are not aligned in time, two fits are applied to the cluster time distribution in order to estimate the average time for the two contributes separately.

The correction for this time misalignment between two CMs, which read out strips of the same panel, is required by the cluster construction algorithm. Indeed without this correction any cluster, including strip 8 and 9, is split in two different clusters according to the algorithm described in section 6.2.1 (which requires a maximum difference of 15 *ns* among hits of the same cluster). After the scaling of 53 *ns* for the strips 1-8, the hit time distribution for all the strips is shown in figure 6.36.

In summary, until the time alignment will be performed, it is essential to check that the strips of a panel are read-out by the same CM, otherwise the time alignment of the channels has to be verified. If a time misalignment is found, the cluster algorithm is applied at the beginning in order to separate the two different group of hit times and each peak in the distribution is fitted separately to estimate the misalignment. Then the hit times are renormalized so to have a single time reference for all the channels and the algorithm is applied a second time to correctly construct the clusters.

Finally, in figure 6.37 the average time (triangles) for each $\eta$ strip panel of the third $\eta$ tower in trigger sector 56 is shown. The average time is estimated by applying a Gaussian fit to the time distribution, considering only the efficient clusters (so to eliminate the tails of the time distribution, as shown in figure 6.31).

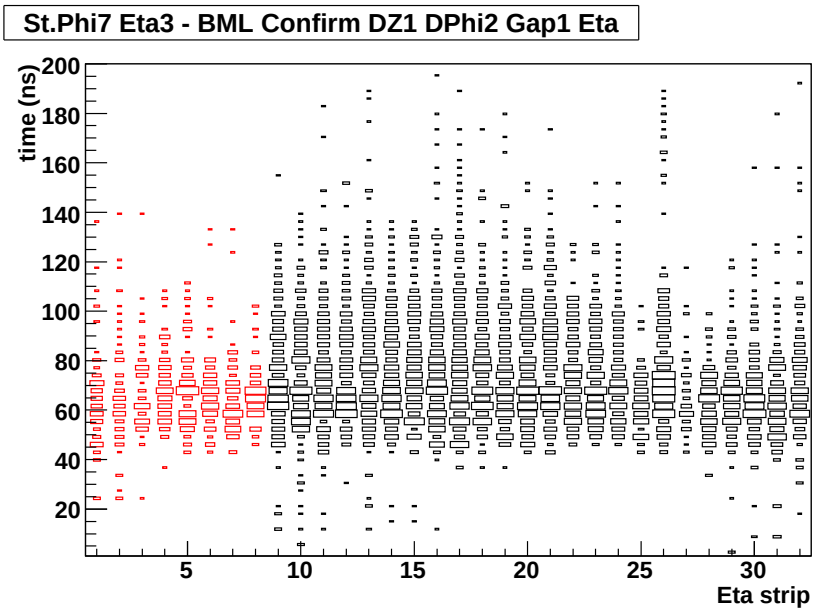


Figure 6.36: Hit time versus the hit strip number for panel 4, $\eta$ station 3. The times measured for the strips 1-8 (red) are subtracted of 53 $ns$, in order to normalize the hit at the reference time of the others channels (see figure 6.33).

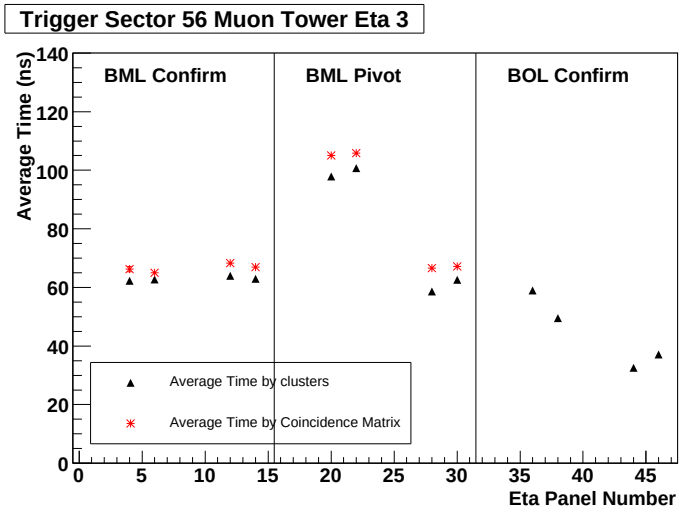


Figure 6.37: Average time of the efficient cluster (triangles) for the $\eta$ strip panels of the third $\eta$ tower in trigger sector 56. The average time measured in the Coincidence Matrix is also shown by the red stars (not available for BOLs). Each couple of points is relative to the $\eta$ panels belonging to the same RPC doublet, which are connected to the same CM with cables of similar length.

The time misalignment of the muon trigger tower is visible: the average times are scattered in a range of about 80 $ns$. For each couple of panels of a RPC doublet (coupled points in figure 6.37) the difference is within 20 $ns$, because they are connected to the same CM with cables of similar length.

The average time measured in the Coincidence Matrix is also shown in figure 6.37 by the red stars. The average cluster time and the CM times are consistent within 3 clock time bins (9.375 $ns$).

## 6.6 Conclusions

In summer 2006 the first test of a Muon Spectrometer sector, already installed in the ATLAS cavern, was carried out. Three complete muon towers in the ATLAS barrel sector 13 were selected for the test. The main goals of the cosmic ray tests in the cavern were the detector calibration, the optimization of the detector working point and the trigger configuration.

To study the RPC performances, a cluster algorithm has been implemented. The average number of clusters per event is 1.2. Due to the after pulses and hit duplications in the overlap trigger regions, the hit time distribution is a few $ns$ delayed with respect to the cluster time distribution, where the spurious signals have been removed. Moreover it shows a relevant tail, which increases the RMS of about 7.5 $ns$ ($\sim$ 30-40%) with respect to the cluster time distribution. At the conditions set for the analyzed run (High Voltage 9.6 $kV$ and electronics threshold 1.0 $V$) the average cluster size is 1.5.

In the $\eta$ view the detection efficiency was evaluated by comparing the RPC cluster positions with the muon tracks provided by the MDT chambers. The estimated RPC efficiency is a combination of two contributions: the gas volume efficiency and the $\eta$ FE efficiency. The strip panel efficiency is 92% on average. The high voltage plateau indicates a working point around $\sim$ 10 $kV$ somewhat higher than the value used during the test (9.6 $kV$).

The time alignment within a muon trigger tower can be evaluated by comparing the average cluster times of all the read-out panels. A preliminary time alignment was only performed in the $\varphi$ view to ensure the trigger. For the $\eta$ tower 2 of the trigger sector 56, for example, the average cluster times in the $\varphi$ view result aligned within 3 clock bins (9.375 $ns$) and are in agreement with the times measured in the CMs.

In the $\eta$ view instead, the time alignment has still to be carried out, both be-

tween the RPC stations (BML Confirm, BML Pivot and BOL Confirm) and among the CMs. The time misalignment between two CMs, which read out strips of the same panel, has to be taken into account during the cluster construction. The hits have to be renormalized to the same time reference in order to define the clusters correctly. A time misalignment up to 80 $ns$ (trigger sector 56, tower 3) was observed in the $\eta$ towers.

# Conclusions

The deep knowledge of the detector and the complete control of its performance are essential for the chambers providing the trigger at the ATLAS experiment. A test-beam of a muon tower of the ATLAS barrel Muon Spectrometer and a quality test for the mass production of the largest barrel (BOL) RPCs allowed to accurately investigate on the performances of the RPCs and are both presented in this thesis.

At the test-beam the trigger chambers were assembled together with the precision chambers, according to an ATLAS muon tower; this allowed to compare the RPC data with the reconstructed muon tracks. In this test the study of the RPC clusters showed that the size of a cluster is not random, but it depends on the position of the muon track with respect to the read-out strip panel. In particular clusters with size 1 are more frequent for tracks crossing the detector near the centre of a strip; whereas clusters with size 2 are mainly due to tracks impacting in the region between two adjacent strips. It was also shown that the average cluster size is sensitive to the RPC working point.

The systematic test of 192 BOL RPCs allowed to characterize the performance of each single RPC unit. These results will be available in a data base for monitoring the unit performance and its evolution during the experiment. Moreover the large amount of collected data provides the necessary statistics to study in detail the detector physics.

At the working point of 10.2 $kV$ (normalized at $T = 293.15\ K$ and $P = 1010\ mbar$) and at the FE electronics threshold of 1.0 $V$, the performance of the BOL units can be described by the following average values: detection efficiency $\sim 97\%$, cluster size 1.4 strips, single counting rate 0.4 $Hz/cm^2$ and gap current 0.8 $\mu A$. These values of counting rate and gap current, being lower than the values measured for the prototypes, show that a better quality level was achieved by the mass production.

In addition a linear correlation between the single counting rate and the gap

current was observed. This observation supports the interpretation that, for a perfectly optimized detector Faraday cage, the noise is mainly due to discharges occurring inside the gas.

Furthermore an accurate dedicated measurement has shown that in the standard operation no cross-talk is observed between the two RPC layers assembled in the same mechanical structure. This test ensures the hermeticity of the Faraday cage, which is a crucial characteristic for the trigger rejection power of the low energy background.

The RPCs will be used to trigger cosmic rays during the detector commissioning tests. For this purpose different trigger logic configurations dedicated to select cosmic muons have been simulated and studied. As described in this thesis, the configuration with the highest trigger rate for the cosmic muon (1.1 $kHz$) is the one requiring a two-out-of-two coincidence of the pivot planes. Moreover the trigger rates with the ATLAS standard logic due to cosmic muons were evaluated to be an order of magnitude lower than the muon trigger rates for the $p$-$p$ collisions, for both the low-$p_T$ and high-$p_T$ triggers.

Furthermore the commissioning test of three muon towers in the ATLAS cavern, reported here, allowed for the first time to validate the trigger simulation. For the comparison a dedicated simulation, accounting for the real trigger used for the three stations under test, has been performed. It should be stressed however that this simulation used the standard ATLAS layout, whereas during the test a significant part of the ATLAS detector was missing, resulting in a different cosmic muon absorption. This may contribute to explain the higher rate measured with respect to the simulation.

The analysis of the RPC data collected at the first commissioning test are also presented. A cluster algorithm has been implemented for the RPC data, although the analysis required a correction via software of the time alignment between the chambers, which had to be still optimized. The average number of clusters per event was 1.2 with a size of 1.5 on average. An independent evaluation of the RPC detection efficiency was performed comparing the cluster centres with the muon tracks reconstructed by the MDT chambers: the average value was found to be 92% at a working point of 9.6 $kV$ (normalized at $T = 293.15\,K$ and $P = 960\,mbar$) and at the FE electronics threshold of 1.0 $V$.

At the end of the work for this thesis, it can be observed that the participation to the RPC tests allowed to acquire a significant experience and an accurate knowledge of the detector and its parameters. Furthermore the study of the trigger logic for the cosmic muon selection allowed to improve the understanding of the

first level trigger. Finally the analysis of the RPC data stimulated the development of a tool which will be useful to debug the detector during the commissioning phase.

# Bibliography


[1] The LHC Study Group: "The Large Hadron Collider - Conceptual Design", CERN/AC/95-05.

[2] Z. Kunszt et al.: “Higgs production at LHC”, Z. Phys C74.

[3] ATLAS Collaboration, “ATLAS Letter of Intent for a General-Purpose pp Experiment at the Large Hadron Collider at CERN ”, CERN/LHCC/92-4.

[4] ATLAS Collaboration, “Technical Proposal for a General Purpose pp Experiment at the Large Hadron Collider at CERN”, CERN/LHCC/94-43.

[5] ATLAS Collaboration: “Detector and Physics Performance Technical Design Report”, CERN/LHCC 99-14/15.

[6] CMS Collaboration: “CMS Technical Proposal”, CERN/LHCC 94-38.

[7] ATLAS Muon Collaboration: “ATLAS Muon Spectrometer Technical Design Report”, CERN/LHCC 97-22.

[8] W. Blum: “High-precision drift tubes”, ATLAS Internal Note MUON-NO-24 (1993).

[9] K. Nagai: “Thin Gap Chambers in ATLAS”, *Nuclear Instruments and Methods in Physiscs Research* NIM A384 (1996) 219.

[10] ATLAS Level-1 Trigger Group: “ATLAS First-Level Trigger Technical Design Report”, CERN/LHCC 97-22 (1998).

[11] M. Abbrescia et al.: *NIM, Nuclear Instruments and Methods in Physiscs Research* NIM A359 (1995).

[12] P. Camarri et al.: *NIM, Nuclear Instruments and Methods in Physiscs Research* NIM A409 (1998).

[13] P. Camarri et al.: “Streamer suppression with $SF_6$ in RPCs operated in avalanche mode”, *Nuclear Instruments and Methods in Physiscs Research* NIM A414 (1998).

[14] R. Cardarelli et al.: “Avalanche and streamer mode operation of resistive plate chambers”, *Nuclear Instruments and Methods in Physics Research* NIM **A382** (1996).

[15] R. Cardarelli, A. Di Ciaccio, R. Santonico: “Performance of a resistive plate chamber operating with pure $CF_3Br$, *Nuclear Instruments and Methods in Physiscs Research* NIM 333 (1993).

[16] M. Abbrescia et al.: “Resistive plate chambers working at high rate”, *Nuclear Instruments and Methods in Physiscs Research* NIM B44 (1995).

[17] C. Bacci et al.: “Test of a resistive plate chamber operating with low gas amplification at high intensity beams”, *Nuclear Instruments and Methods in Physiscs Research* NIM **A352** (1995).

[18] R. Santonico: “RPC: Status and perspectives”, *‘Second International Workshop on The Resistive Plate Chambers in particle physics and astrophysics’ on SCIENTIFICA ACTA Quaderni del dottorato (Università degli studi di Pavia)* (15/06/1993).

[19] R. Santonico: “Topics in resistive plate chambers ”, *‘Third International Workshop on Resistive Plate Chambers and related detectors’ on SCIENTIFICA ACTA Quaderni del dottorato (Università degli studi di Pavia)* vol.IX (15/05/1996).

[20] G. Aielli et al.: "RPC ageing studies"; Proceedings of VCI 2001, *Nuclear Instruments and Methods in Physiscs Research* NIM A478 (2002) 271-276.

[21] G. Aielli: Ph.D. thesis, University of Rome Tor Vergata, February 2001.

[22] The GEANT4 Collaboration: "Geant4 - A Simulation Toolkit", Nuclear Instruments and Methods in Physiscs Research NIM A506 (2003) 250-303

[23] "ATHENA Developer Guide",
http://atlas.web.cern.ch/Atlas/GROUPS/SOFTWARE/OO/architecture/General/
/Documentation/Documentation/DeveloperGuide/AthenaDeveloperGuide.pdf

[24] F. Conventi: "The Simulation of the Level-1 muon trigger at LHC", PhD Thesis.

[25] V. Bocci, E. Petrolo, A. Salamon, R. Vari, S. Veneziano: “The Coincidence Matrix ASIC of the Level-1 Muon Barrel Trigger of the ATLAS Experiment”, *IEEE Transactions on Nuclear Science*, (2003) Issue vol.50, no.4.

[26] A. Aloisio, G. Carlino, F. Conventi, V. Izzo, A. Migliaccio, V. Bocci, A. Di Mattia, L. Luminari, A. Nisati, F. Pastore, E. Petrolo, R. Vari, S. Veneziano, A. Salamon: “The RPC Level-1 Muon Trigger of the ATLAS Experiment at the LHC”, *IEEE Transactions on Nuclear Science*, (2005).

[27] A.Dell’Acqua, A.Rimoldi, V.Vercesi: “Level-1 Muon Trigger Simulation in the Barrel Region”, ATLAS Internal Note ATL-MUON-94-067, ATL-M-PN-67.

[28] D.E. Groom et al.: “Review of Particle Physics”, The European Physical Journal C15 (2000).

[29] Particle Data Group: “Journal of Physics G: Nuclear and Particle Physics” Institute of Physics publishing, volume 33 (July 2006).

[30] R. Bellotti et al., Physical Review **D60**, 052002 (1999).

[31] R. Bellotti et al., Physical Review **D53**, 35 (1996).

[32] M. Boezio et al., Physical Review **D62**, 032007 (2000).

[33] S. Coutu et al., Physical Review **D62**, 032001 (2000).

[34] J.Shank et al.: “Track Reconstruction in the ATLAS Muon Spectrometer with MOORE”, ATLAS Notes ATL-COM-MUON-2003-012, ATL-COM-SOFT-2003-008.

# Acknowledgements

Al termine di questo lavoro di tesi, desidero esprimere la mia sentita gratitudine alle persone che maggiormente hanno contribuito alla mia formazione scientifica e che pazientemente mi hanno incoraggiato e supportato durante questi tre anni.

In primis il professore Rinaldo Santonico e la professoressa Anna Di Ciaccio, che hanno costantemente vigilato e indirizzato il mio lavoro con suggerimenti stimolanti e costruttivi.

Poi la dottoressa Barbara Liberti, che non mi ha mai privato della sua simpatica e preziosa collaborazione, e tutti i colleghi che gentilmente hanno condiviso con me la loro notevole esperienza: in particolare i dottori Roberto Cardarelli, Paolo Camarri, Giulio Aielli, Andrea Salamon, Lucrezia Palummo, Enrico Pastori, Fabrizio Marchese e Fabio Martinelli.

Una profonda riconoscenza mi lega ai tecnici Luigi Di Stante, Emiliano Paoletti e Luigi Pasquali, per la simpatia e per la disponibilità nel condividere le loro competenze.

Desidero inoltre ringraziare il dottor Andrea Di Simone, sempre disponibile a sopperire alle mie carenze nel software, ed i dottori Aleandro Nisati e Francesco Conventi, che gentilmente hanno messo a mia disposizione le loro conoscenze del trigger dell'esperimento ATLAS.

In ultimo desidero esprimere la mia gratitudine ai miei genitori, fiduciosi sostenitori della mia formazione scientifica, ed a mio marito, per la sua pazienza ed il suo amore.